Dynamics of water between graphene and mica

Edwin Dollekamp

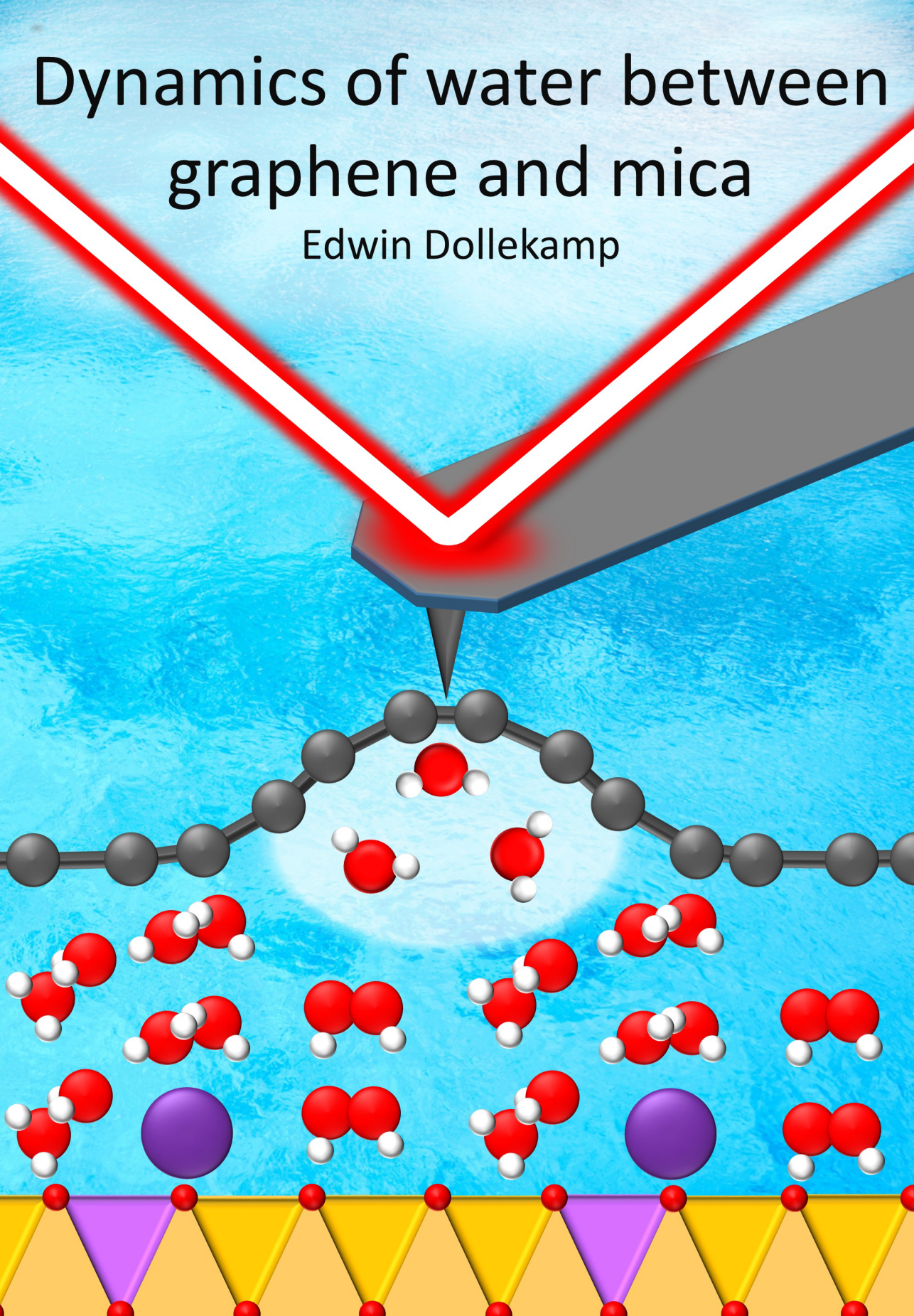

Dynamics of water between graphene and mica

Edwin Dollekamp

Composition of graduation committee:

Chairman and secretary:	Prof. dr. J.L. Herek
Supervisor:	Prof. dr. ir. H.J.W. Zandvliet
Co-supervisor:	Dr. E.S. Kooij
Members:	Prof. dr. ir. R.G.H. Lammertink Prof. dr. J.C.T. Eijkel Prof. dr. T. Banerjee Prof. dr. S. De Gendt Dr. P. Bampoulis

The work described in this thesis was carried out in the Physics of Interfaces and Nanomaterials group, MESA+ Institute for Nanotechnology, University of Twente, the Netherlands.

This work was supported by the Netherlands Center for Multiscale Catalytic Energy Conversion (MCEC), an NWO Gravitation programme funded by the Ministry of Education, Culture and Science of the government of the Netherlands.

Published by Physics of Interfaces and Nanomaterials, University of Twente.
Cover Design: Dynamics of water between graphene and mica. By Edwin Dollekamp.
Printed by: Gildeprint, Enschede, The Netherlands.

ISBN: 978-90-365-4659-1
DOI: 10.3990/1.9789036546591

DYNAMICS OF WATER BETWEEN GRAPHENE AND MICA

DISSERTATION

to obtain
the degree of doctor at the University of Twente,
on the authority of the rector magnificus,
prof. dr. T.T.M. Palstra,
on account of the decision of the Doctorate Board,
to be publicly defended
on Friday the 25th of January 2019 at 16:45 hours

by

Edwin Dollekamp
born on the 14th of September 1989
in Hellendoorn, The Netherlands

This dissertation has been approved by:

Supervisor:
Prof. dr. ir. H.J.W. Zandvliet

Co-supervisor:
Dr. E.S. Kooij

Contents

1

Introduction

1.1 Introduction

The interaction of water with surfaces under ambient conditions is of high relevance for nanofluidics, lubrication, biomass conversion, solar fuels, catalysis and biological systems. For example, in heterogeneous catalysis, the availability of the solid-liquid interface is of utmost importance for efficient electrochemical reactions. (Nano)bubbles at the surface hinder this process and lower the efficiency of the catalytic surface. Probing water films at ambient conditions is challenging due to the dynamic nature of the water molecules. Therefore, most experimental knowledge has been obtained with cryogenic temperature experiments in ultra-high-vacuum (UHV) systems.

The properties of water under confinement are significantly different than bulk water due to strong interactions with the surfaces.[1] A fundamental understanding of the dynamics of confined water is of utmost importance for the fields of electrocatalysis.[2–4] Due to the confined nature, it is hard to microscopically image the dynamics of the water molecules. Therefore, most of our knowledge comes from molecular dynamics (MD) simulations and density functional theory (DFT) calculations. The discovery of the two-dimensional (2D) material graphene, in combination with the development of scanning probe microscopy techniques, made it for the first time possible to study the dynamics of confined water at room temperature. Due to graphene's mechanical flexibility and impermeability, it can be used as an ultra-thin coating to study the dynamics of water molecules. Xu et al.[5] first used the remarkable properties of graphene to study water adlayers on a mica substrate. Since then, graphene covered water layers have been studied on a

variety of substrates, which resulted in a profound increase in fundamental knowledge about the structural and dynamic properties of water. In this thesis, the knowledge of the dynamics of water between graphene and mica is expanded.

In the remainder of this chapter, we introduce the key concepts used in this thesis. First, we elaborate on the 2D material graphene. Next, we present the properties of mica. We continue with discussing the structure of water on mica. Afterward, we describe the influence of a graphene cover on the water molecules. We end with the scope and outline of this thesis.

1.2 Graphene

Graphene is a two-dimensional material consisting of carbon atoms arranged in a honeycomb network, see Figure 1.1(a). The existence of graphene was experimentally demonstrated in 2004 by Geim and Novoselov[6] and was awarded the Nobel Prize in Physics in 2010. Since then, many other two-dimensional materials have been discovered.[7] Graphene is conductive, mechanically flexible,[8] impermeable to gases/small molecules,[9] hydrophobic, and the strongest material known today with a Young's modulus of 1 GPa.[8] Furthermore, the electrons in graphene behave as massless relativistic particles and have a Fermi velocity of 10^6 m/s.[10] Moreover, the electrons and holes in graphene have a mobility of 10^4 $cm^2V^{-1}s^{-1}$ at room temperature.[6] One layer of graphene is 0.335 nm thick[11] and has a transparency of 97,7% in the visible light spectrum.[12] Graphene can be obtained by the mechanical exfoliation of graphite.[6,7] The graphite used in this thesis is highly oriented pyrolytic graphite (HOPG). A photo of a block of HOPG is shown in Figure 1.1(b). The layered structure and some vertical standing HOPG flakes are observed. This exfoliation method is further discussed in the experimental techniques chapter.

1.3 Mica

In this thesis we used the mineral muscovite mica as a substrate. Mica is hydrophilic, insulating and has a structural formula of $KAl_2(Al,Si_3)O_{10}(OH)_2$. A schematic illustration of the molecular structure of mica is given in Figure 1.2(a). The sheets of mica consist of octahedral layers which are sandwiched between tetrahedral layers. The negatively charged mica sheets are weakly

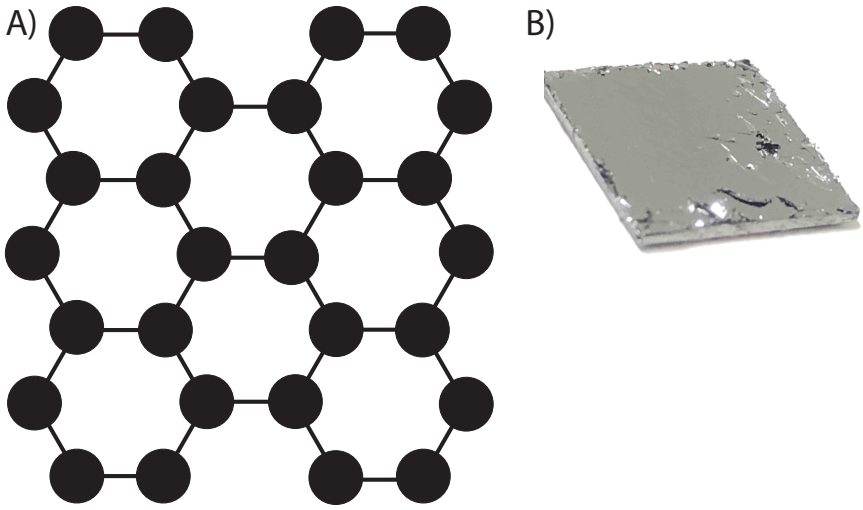

Figure 1.1: (a) The atomic structure of graphene. (b) A photo of a piece of HOPG.

bound together with positive potassium ions. After cleaving, the potassium ions distribute between the two formed surfaces to provide charge neutrality. The potassium ions show a non-uniform distribution by forming islands and rows.[13] A photo of two pieces of mica is shown in Figure 1.2(b). A cleaved mica surface is atomically flat.[14] Due to its flatness, it serves as a perfect substrate to study changes in height, e.g. a different number of water layers on the surface.

1.4 The structure of water on mica

Since mica is hydrophilic, it will attract water molecules from ambient. Hu et al. were the first to experimentally observe water layers on mica at nanometer resolution with scanning polarization force microscopy (SPFM).[15–17] In SPFM, a conductive AFM tip is electrically polarized by applying a voltage. The electric field of the tip induces an electrical polarization of the surface. The electrostatic force between the tip and the sample can be measured and an electronic feedback control can be incorporated to obtain the topography. In this method, the tip is ∼100 Å away from the surface, so capillary iterations do not disturb the water layers. The authors observed

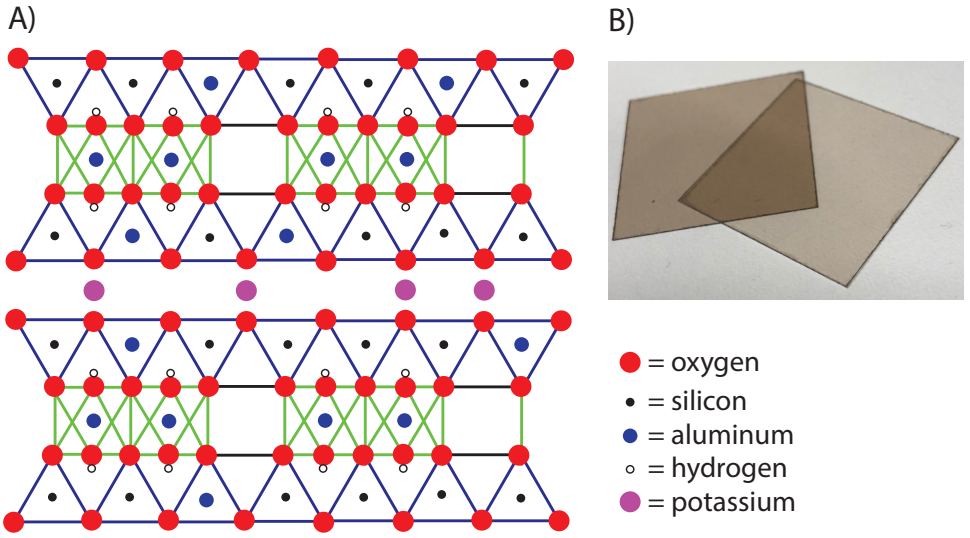

Figure 1.2: (a) The molecular structure of mica. (b) A photo of two pieces of mica.

the growth of small two-dimensional clusters at ∼28 % relative humidity (RH) and full monolayer coverage at ∼40-50% RH.[15,18] The full monolayer ice-like coverage has a smaller dielectric constant as compared to the small two-dimensional clusters.[15,18]

This first water layer on mica under ambient conditions was predicted to be ice-like by density functional theory (DFT) calculations of Odelius et al.[19] In this case, a fully connected hydrogen-bonded network forms on the mica surface with no dangling OH bonds sticking out of the surface. In this configuration, the H atoms of the water point toward the mica, resulting in a net dipole moment. Miranda et al. managed to experimentally verify this ice-like structure for D_2O by sum-frequency-generation (SFG) vibrational spectroscopy and SPFM.[18] They used D_2O instead of H_2O to avoid confusion between the OH stretch modes in the H_2O and the mica. When the humidity was increased, the authors observed a strong signal increase of the 2375 cm^{-1} peak, which corresponds to the ordered tetrahedrally coordinated hydrogen-bonding network. At RH $>$ 97% they observed also a peak at 2740 cm^{-1}, which corresponds to the O-D stretch of non-hydrogen-bonded O-D groups. Therefore, the first water layer on mica is highly ordered, with no free O-H

bonds and the second layer is less ordered (liquid-like) with some free O-H bonds. The multilayers of water on mica at high humidity follow a Stranski-Krastanov growth model.[20] Li et al. calculated with DFT that the second and third water layer still possess perpendicular order.[21] This order is larger in the second layer as compared to the third layer.

1.5 The structure of water between graphene and mica

Xu et al. showed that the water layers on mica can be visualized in AFM by placing graphene on top.[5] Graphene namely prohibits capillary interactions of the AFM tip with the water molecules. Due to graphene's mechanical flexibility, it can perfectly conform to the underlying water molecules. Next to mica, graphene was also used as protective cover to study water layers on HOPG[22] and SiO_2.[23] Li et al.[21] showed with DFT that graphene enhances the stability of the water molecules.

There is still a discussion in literature about how many layers are intercalated between graphene and mica under ambient conditions. In the structural model developed by Bampoulis et al., which we use in this thesis, two water layer are located between graphene and mica under ambient conditions[13,24]. At low relative humidity, some top water layer molecules evaporate out of the slit pore, leaving behind fractal-like depressions.[25] The height of these depressions (0.37 nm[26]) corresponds to the interlayer spacing of hexagonal ice. The remaining water layer is a 2D-ice layer which can be melted to a quasi-liquid phase by applying a high normal force with an AFM tip.[27] This melting can be seen in the AFM topography and friction images. With conductive AFM, also a higher conductivity at the location of the 2D-ice fractals is observed, as compared to the double water layer. This higher conductivity indicates that the water is polarized and dopes the graphene. This doping was also confirmed by scanning tunneling microscopy (STM) experiments, where p-type doping of the graphene was observed.[24] The melted quasi-liquid layer showed no conductivity, indicating that these water molecules are not polarized. With conductive AFM, Bampoulis et al.[13] zoomed-in on the ice-like layer and observed current variations corresponding to individual potassium ions. At the locations of the potassium ions, a low conductance was observed, since the mica+potassium is neutral and only the polarized water molecules contribute to the charge doping. At locations without potassium ions, a

higher conductance was observed since here both the negatively charged mica and polarized water molecules contribute to the charge doping.

In the structural model developed by other groups, one layer is argued to be located between graphene and mica under ambient conditions.[25,28] This layer can partly be removed when the humidity is lowered. At low humidity, they observed with Raman spectroscopy the presence of the D' peak in areas with an evaporated water layer. They attributed this signal to the ionic mica surface in dry conditions.[28]

1.6 Goal of the work / problem statement

The problem statement/research question for this thesis was: what are the dynamic properties of water under confinement? To answer this question we used the well known graphene-mica system. Most of the work on graphene-mica systems involved static measurements. An exemption is the formation of 2D-ice fractals where the intercalated water molecules evaporated out of the slit pore.[25] Experimentally challenging experiments were performed to play with the dynamics of the confined water molecules. For example, we reduced the confined water molecules to hydrogen, charged the graphene and replaced intercalated water molecules with alcohol molecules to see how it affects the mechanical properties of the graphene-mica system. The goal of this thesis work was to get more insight into the dynamics of confined water. A molecular level understanding of the dynamics of two-dimensional confined water has great relevance for understanding water flow in for example nanofluidics.

The problem statement/research question for chapter 4 was: is it possible to reduce confined water between graphene and mica to hydrogen? There needs to be enough charge transport in the confined water film to foster the nucleation and sustain the presence of nanobubbles. The second reason for this nanobubble work is to get a better fundamental understanding of (surface) nanobubbles. The existence of surface nanobubbles is still under discussion in literature.[29] The only method to probe these nanobubbles is by AFM. However, it has been shown that PDMS contamination can easily occur and mistakenly can be interpreted as nanobubbles.[30] Electrochemically induced surface nanobubbles have been studied in literature.[31,32] Observation of nanobubbles between graphene and mica and the absence of surface nanobubbles on top of the graphene may point in the direction that surface

nanobubbles do not exist. This may have a positive impact on the field of electrocatalysis, since it is believed that surface nanobubbles block electrochemical reactions due to the reduced availability of the liquid-solid interface.

The problem statement/research question for this chapter 5 was: what is responsible for the movement of water layers between graphene and mica? During the nucleation of nanobubbles between graphene and mica, we observed the movement of water layers. Also, when a nanobubble disappeared due to dissolution into the bulk water, an extra water layer was observed to be present at the location where the nanobubble used to be. This indicates that the extra water layer has probably an important role in the formation of the nanobubble.

The problem statement/research question for this chapter 6 was: is it possible to change the friction of graphene by replacing intercalated water by alcohol molecules? Altering the friction has been shown to be possible by changing the number of graphene layers,[33] changing the mass of the intercalated molecule[34] or changing the number of intercalated water layers.[35] In our approach, we used the intercalation of alcohol. An advantage is that the alcohol intercalation can be controlled by changing the environment in which the graphene-mica sample is placed.

1.7 Scope and outline

In this thesis, several topics dealing with confined water are studied. In chapter 2 we present the current applications of confined water. The experimental techniques used in this thesis are discussed in chapter 3. In chapter 4, we elaborate on electrochemically induced nanobubbles between graphene and mica. These nanobubbles are formed in the 2D confinement and dissolve slower than their bulk counterparts. We show that these nanobubbles have a pressure in the MPa range and that we can vary the size of the nanobubbles by electrochemical actuation. Applications of these nanobubbles are for example nanoreactors and the study of gas evolution at low overpotential. In chapter 5 we study the influence of charged graphene on the confined water molecules. For this investigation, we used the graphene-mica system again. Here we found a distinct behavior for water at positively and negatively charged graphene. Due to the confined nature and the large surface area of graphene, the orientation of water molecules toward a charged 2D surface is essential for catalytic reactions. Knowledge of confined water at a charged

surface is also crucial for the control over graphene nanobubbles created by water splitting.[36,37] The influence of charge on the graphene is also highly relevant for the graphene transfer process. In this process, charge influences the water and therefore ion intercalation, and thus the effectiveness of the graphene delamination.[38,39] We end the thesis with chapter 6 about the effects of alcohol intercalation on the frictional properties of the graphene. We found that the frictional properties significantly changed at the location of intercalated alcohol molecules. This finding could open up applications for next-generation nano-lubricants and nano-devices. We end the thesis with general conclusions and an outlook.

Bibliography

[1] Granick, S. Motions and Relaxations of Confined Liquids. *Science* **1991**, *253*, 1374–1379.

[2] Fu, Q.; Bao, X. Surface Chemistry and Catalysis Confined under Two-Dimensional Materials. *Chem. Soc. Rev.* **2017**, *46*, 1842–1874.

[3] Deng, D.; Novoselov, K. S.; Fu, Q.; Zheng, N.; Tian, Z.; Bao, X. Catalysis with Two-Dimensional Materials and their Heterostructures. *Nat. Nanotechnol.* **2016**, *11*, 218.

[4] Li, H.; Xiao, J.; Fu, Q.; Bao, X. Confined Catalysis under Two-Dimensional Materials. *Proc. Natl. Acad. Sci. U. S. A.* **2017**, *114*, 5930–5934.

[5] Xu, K.; Cao, P.; Heath, J. R. Graphene Visualizes the First Water Adlayers on Mica at Ambient Conditions. *Science* **2010**, *329*, 1188–1191.

[6] Novoselov, K. S.; Geim, A. K.; Morozov, S. V.; Jiang, D.; Zhang, Y.; Dubonos, S. V.; Grigorieva, I. V.; Firsov, A. A. Electric Field in Atomically Thin Carbon Films. *Science* **2004**, *306*, 666–669.

[7] Novoselov, K. S.; Jiang, D.; Schedin, F.; Booth, T. J.; Khotkevich, V. V.; Morozov, S. V.; Geim, A. K. Two-Dimensional Atomic Crystals. *Proc. Natl. Acad. Sci.* **2005**, *102*, 10451–10453.

[8] Lee, C.; Wei, X.; Kysar, J. W.; Hone, J. Measurement of the Elastic Properties and Intrinsic Strength of Monolayer Graphene. *Science* **2008**, *321*, 385–388.

[9] Bunch, J. S.; Verbridge, S. S.; Alden, J. S.; Van Der Zande, A. M.; Parpia, J. M.; Craighead, H. G.; McEuen, P. L. Impermeable Atomic Membranes from Graphene Sheets. *Nano Lett.* **2008**, *8*, 2458–2462.

[10] Novoselov, K. S.; Geim, A. K.; Morozov, S. V.; Jiang, D.; Katsnelson, M. I.; Grigorieva, I. V.; Dubonos, S. V.; Firsov, A. A. Two-Dimensional Gas of Massless Dirac Fermions in Graphene. *Nature* **2005**, *438*, 197–200.

[11] Al-Jishi, R.; Dresselhaus, G. Lattice-Dynamical Model for Graphite. *Phys. Rev. B* **1982**, *26*, 4514–4522.

[12] Nair, R. R.; Blake, P.; Grigorenko, A. N.; Novoselov, K. S.; Booth, T. J.; Stauber, T.; Peres, N. M. R.; Geim, A. K. Fine Structure Constant Defines Visual Transparency of Graphene. *Science* **2008**, *320*, 1308–1308.

[13] Bampoulis, P.; Sotthewes, K.; Siekman, M. H.; Zandvliet, H. J. W.; Poelsema, B. Graphene Visualizes the Ion Distribution on Air-Cleaved Mica. *Sci. Rep.* **2017**, *7*, 43451.

[14] Lui, C. H.; Liu, L.; Mak, K. F.; Flynn, G. W.; Heinz, T. F. Ultraflat Graphene. *Nature* **2009**, *462*, 339–341.

[15] Hu, J.; Xiao, X. D.; Ogletree, D. F.; Salmeron, M. Imaging the Condensation and Evaporation of Molecularly Thin Films of Water with Nanometer Resolution. *Science* **1995**, *268*, 267.

[16] Hu, J.; Ogletree, D. F.; Salmeron, M. The Structure of Molecularly Thin Films of Water on Mica in Humid Environments. *Surf. Sci.* **1995**, *344*, 221–236.

[17] Hu, J.; Xiao, X.; Salmeron, M. Scanning Polarization Force Microscopy: A Technique for Imaging Liquids and Weakly Adsorbed Layers. *Appl. Phys. Lett.* **1995**, *67*, 476–478.

[18] Miranda, P. B.; Xu, L.; Shen, Y. R.; Salmeron, M. Icelike Water Monolayer Adsorbed on Mica at Room Temperature. *Phys. Rev. Lett.* **1998**, *81*, 5876.

[19] Odelius, M.; Bernasconi, M.; Parrinello, M. Two Dimensional Ice Adsorbed on Mica Surface. *Phys. Rev. Lett.* **1997**, *78*, 2855.

[20] Song, J.; Li, Q.; Wang, X.; Li, J.; Zhang, S.; Kjems, J.; Besenbacher, F.; Dong, M. Evidence of Stranski-Krastanov Growth at the Initial Stage of Atmospheric Water Condensation. *Nat. Com.* **2013**, *5*, 4837.

[21] Li, H.; Zeng, X. C. Two Dimensional Epitaxial Water Adlayer on Mica with Graphene Coating: An Ab Initio Molecular Dynamics Study. *J. Chem. Theory Comput.* **2012**, *8*, 3034–3043.

[22] Cao, P.; Xu, K.; Varghese, J. O.; Heath, J. R. The Microscopic Structure of Adsorbed Water on Hydrophobic Surfaces Under Ambient Conditions. *Nano Lett.* **2011**, *11*, 5581–5586.

[23] Lee, M. J.; Choi, J. S.; Kim, J. S.; Byun, I. S.; Lee, D. H.; Ryu, S.; Lee, C.; Park, B. H. Characteristics and Effects of Diffused Water Between Graphene and a SiO_2 Substrate. *Nano Res.* **2012**, *5*, 710–717.

[24] Bampoulis, P.; Siekman, M. H.; Kooij, E. S.; Lohse, D.; Zandvliet, H. J. W.; Poelsema, B. Latent Heat Induced Rotation Limited Aggregation in 2D Ice Nanocrystals. *J. Chem. Phys.* **2015**, *143*, 034702.

[25] Severin, N.; Lange, P.; Sokolov, I. M.; Rabe, J. P. Reversible Dewetting of a Molecularly Thin Fluid Water Film in a Soft Graphene-Mica Slit Pore. *Nano Lett.* **2012**, *12*, 774–779.

[26] Fletcher, N. H. The Chemical Physics of Ice. *The Chemical Physics of Ice, by NH Fletcher, Cambridge, UK: Cambridge University Press* **2009**,

[27] Sotthewes, K.; Bampoulis, P.; Zandvliet, H. J. W.; Lohse, D.; Poelsema, B. Pressure-Induced Melting of Confined Ice. *ACS Nano* **2017**, *11*, 12723–12731.

[28] Lin, H.; Schilo, A.; Kamoka, A. R.; Severin, N.; Sokolov, I. M.; Rabe, J. P. Insight into the Wetting of a Graphene-Mica Slit Pore with a Monolayer of Water. *Phys. Rev. B* **2017**, *95*, 195414.

[29] Berkelaar, R. Nanobubble-Like Objects at Solid-Liquid Interfaces. Ph.D. thesis, University of Twente, 2014.

[30] Berkelaar, R. P.; Dietrich, E.; Kip, G. A. M.; Kooij, E. S.; Zandvliet, H. J. W.; Lohse, D. Exposing Nanobubble-Like Objects to a Degassed Environment. *Soft Matter* **2014**, *10*, 4947–4955.

[31] Zhang, L.; Zhang, Y.; Zhang, X.; Li, Z.; Shen, G.; Ye, M.; Fan, C.; Fang, H.; Hu, J. Electrochemically Controlled Formation and Growth of Hydrogen Nanobubbles. *Langmuir* **2006**, *22*, 8109–8113.

[32] Yang, S.; Tsai, P.; Kooij, E. S.; Prosperetti, A.; Zandvliet, H. J. W.; Lohse, D. Electrolytically Generated Nanobubbles on Highly Orientated Pyrolytic Graphite Surfaces. *Langmuir* **2009**, *25*, 1466–1474.

[33] Lee, C.; Li, Q.; Kalb, W.; Liu, X.-Z.; Berger, H.; Carpick, R. W.; Hone, J. Frictional Characteristics of Atomically Thin Sheets. *Science* **2010**, *328*, 76–80.

[34] Lee, H.; Ko, J.-H.; Song, H. C.; Salmeron, M.; Kim, Y.-H.; Park, J. Y. Isotope- and Thickness-Dependent Friction of Water Layers Intercalated Between Graphene and Mica. *Tribol. Lett.* **2018**, *66*, 36.

[35] Lee, H.; Ko, J.-H.; Choi, J. S.; Hwang, J. H.; Kim, Y.-H.; Salmeron, M.; Park, J. Y. Enhancement of Friction by Water Intercalated between Graphene and Mica. *J. Phys. Chem. Lett.* **2017**, *8*, 3482–3487.

[36] Dollekamp, E.; Bampoulis, P.; Poelsema, B.; Zandvliet, H. J. W.; Kooij, E. S. Electrochemically Induced Nanobubbles between Graphene and Mica. *Langmuir* **2016**, *32*, 6582–6590.

[37] An, H.; Tan, B. H.; Moo, J. G. S.; Liu, S.; Pumera, M.; Ohl, C.-D. Graphene Nanobubbles Produced by Water Splitting. *Nano Lett.* **2017**, *17*, 2833–2838.

[38] Verguts, K.; Schouteden, K.; Wu, C.-H.; Peters, L.; Vrancken, N.; Wu, X.; Li, Z.; Erkens, M.; Porret, C.; Huyghebaert, C.; Van Haesendonck, C.; De Gendt, S.; Brems, S. Controlling Water Intercalation Is Key to a Direct Graphene Transfer. *ACS Appl. Mater. Interfaces* **2017**, *9*, 37484–37492.

[39] Verguts, K.; Coroa, J.; Huyghebaert, C.; De Gendt, S.; Brems, S. Graphene Delamination using 'Electrochemical Methods': An Ion Intercalation Effect. *Nanoscale* **2018**, *10*, 5515–5521.

2

Applications of confined water

In this chapter, we discuss the applications of water confined between 2D materials. We start with the promising applications of desalination and blue energy. We follow with describing graphene nanobubbles, we continue with explaining how graphene liquid cells work, followed by the introduction of capacitive sensing. After this, we touch on the transfer of graphene facilitated by water intercalation. We conclude this section with a description of the liquid phase exfoliation method.

2.1 Desalination

Perhaps one of the most promising applications of confined water is desalination. Desalination is the process of sieving ions using membranes. This can for example be useful for converting salt sea water into drinkable water. 2D materials are a promising class of membrane materials for desalination. Nanoporous graphene can for example be used for water desalination.[1–5] The same holds for a multi-layered stack of graphene-oxide.[6–9] Abraham et al. were able to control the interlayer spacing in graphene-oxide, thereby tuning the ion sieving.[10] In this context, the diffusion dynamics of water through these membranes define the membrane functionality. For a more comprehensive and detailed review on this topic we refer to the work of Werber et al.[11]

2.2 Blue energy

Another very important application is blue energy. Blue energy is referred to the process of harvesting energy from a salinity gradient, e.g., between sea water and river water. There are two main processes to extract energy from the salinity gradient: pressure retarded osmosis (PRO) and reverse electrodialysis (RED). In PRO, separation of fresh and salt water with a membrane results in an osmotic flow which is used to move a turbine. In RED, anions and cations are separated under a concentration gradient by flowing ions along alternating anion-selective and cation-selective membranes, resulting in a net electric transport. Current harvesting techniques have a low energy efficiency, mainly due to inefficient membranes. 2D materials are a promising class of membrane materials[12] and the structure and dynamics of water confined in these 2D membranes define its efficiency. The molecular thickness of 2D materials like graphene can significantly increase the ion-concentration gradient, resulting in a large power density.[13] Energy conversion densities three orders of magnitude higher than conventional methods have been obtained.[14] Porous graphene was used to establish cation selectivity, resulting in a potential application for Blue Energy[15]. For further information on this topic we refer the reader to the work of Siria et al.[13]

2.3 Graphene nanobubbles

There are a variety of methods to create small encapsulated gas volumes covered by graphene, the so-called graphene nanobubbles. Lim et al.[16] entrapped water molecules between graphene and diamond. Their graphene-diamond sample was heated to ∼1275 K for 45 min., which is the reconstruction temperature of diamond. The graphene then covalently binds to the diamond, resulting in entrapment of the water molecules. The graphene-water-diamond system is called a hydrothermal anvil cell. Graphene nanobubbles with a density of $\sim 8 \times 10^{10}$ cm^{-2} appeared. In situ Fourier-transform infrared spectroscopy (FTIR) was used to confirm the presence of water in these nanobubbles. The water between the graphene and the diamond was found to be in a supercritical state. This supercritical water is very corrosive and etches the diamond surface, resulting in square-shaped voids. The graphene nanobubble has been transformed into a hydrothermal reactor. The pressure inside these graphene nanobubbles was estimated to be ∼1 GPa. In a

follow-up study, Lim et al.[17] used the graphene-diamond anvil cell to establish high-pressure chemical reactions. With infrared (IR) spectroscopy they observed the polymerization of buckministerfullerene (C_{60}) in the graphene nanobubbles. This confirmed the high pressure in the nanobubbles since this reaction is only possible under high pressure and at high temperatures.

Kayal et al.[18] did molecular dynamics simulations on the confined water system described by Lim et al.[16] They found similar vibrational spectral features and high water relaxation times in nanobubbles with a high water density. On the contrary, low water relaxation times were found in low water density nanobubbles.

In the method described by Dollekamp et al.,[19] confined water was used to create hydrogen nanobubbles between graphene and mica. They reduced confined water between graphene and mica to hydrogen gas, which resulted in the nucleation of nanobubbles. The authors achieved this reduction of water by placing the sample in an electrochemical cell and applying a voltage to the graphene. The nanobubbles had a typical radius of a few hundred nanometers and a height of a few tens of nanometers. This resulted in pressures in the order of a few MPa inside the bubbles. The nanobubbles grew over time until a dynamic equilibrium was established between hydrogen formation in the nanobubble and hydrogen dissolution into the confined water film. Eventually, the growth of these nanobubbles led to the delamination of graphene. The nanobubbles preferred to nucleate at the locations of bottom (B-type) step edges and defects. At these locations, more water is available to promote ion transport.

A similar method was used by An et al.[20] They reduced water between layers of highly oriented pyrolytic graphite (HOPG). In their work 10 mM Na_2CO_3 and NaCl were used as the electrolyte. The pressures they obtained were in the range of 20-50 MPa. Gravimetric hydrogen storage capacity calculations also showed that these graphene nanobubbles have the potential to be used for hydrogen storage. A hydrogen capacity of $\sim$21 wt % was estimated for monolayer graphene nanobubbles.

2.4 Graphene liquid cells

In order to study the growth dynamics of bubbles in water at the nanoscale without perturbing the bubble-water interface, for instance by an AFM tip, encapsulation with graphene is essential. This was demonstrated by Shin et

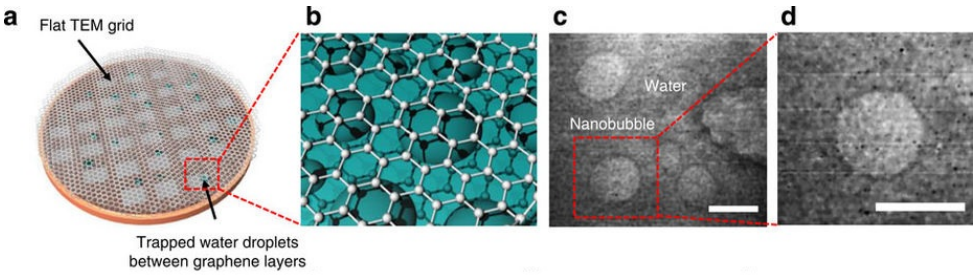

Figure 2.1: (a-b) Schematic illustration of the graphene liquid cell. (c-d) In-situ UHV-TEM images of the confined nanobubbles between graphene. Scale bars, 10 nm. Reprinted with permission from ref.[21] Copyright 2015 Nature Publishing Group.

al.[21] They studied in-situ nanobubbles in water encapsulated between two graphene layers with UHV TEM. A schematic illustration of the graphene liquid cell is given in Figure 2.1(a-b) and UHV-TEM images of the nanobubbles are shown in Figure 2.1(c-d). The graphene encapsulation prevents the gas dissolution into the UHV-TEM chamber since graphene is impermeable to gases. A critical radius of 6.3 $\pm$ 0.8 nm was found for the nanobubbles. Nanobubbles below this size dissolved into the confined water within a minute. Nanobubbles above this size remained stable for $\sim$10 minutes. Two distinct growth mechanisms were observed: Ostwald ripening and coalescence. During the Ostwald ripening, the smaller nanobubbles shrink, while the larger grow even more. During the coalescence, an ultrathin water membrane appears between two nanobubbles, which results in unhydrated gas transport. In a follow-up study, Park et al.[22] studied this merging process in detail. They discovered that the radius-dependent Laplace pressure and distance-dependent gas density were important factors in determining the merging of nanobubbles. These graphene liquid cells have already been applied, for example, to visualize platinum nanocrystal growth at unprecedented resolution.[23] Furthermore, graphene liquid cells can also be used to study nanocrystal-DNA nanoconjugates, which opens the door toward the study of biological samples.[24]

2.5 Capacitive sensing

Olson et al.[25] used a metal-oxide-graphene variable-capacitor (varactor) structure consisting of graphene on HfO_2 to probe water intercalation. When the humidity was increased, water intercalated between the graphene and HfO_2, which resulted in a difference in capacitance. This process was found to be reversible on a short time scale. At high humidity, an n-type doping shift of the Dirac cone in the capacitance-voltage curve was observed, which indicated water intercalation. The authors further confirmed the water intercalation by using pulsed force mode AFM. They observed an increased separation between graphene and HfO_2. Additional DFT and MD simulations[25] validated their experimental observations. The sensitivity of varactors to water intercalation could potentially lead to graphene-based sensors.

2.6 Transferring graphene by water intercalation

Water plays an important role in the transfer process of graphene from a growth substrate to a target substrate. In this section, we elaborate on how confined water is used in different transfer methods. For a more comprehensive review on this topic, we refer to the recently published work of Seah et al.[26]

Schneider et al.[27] developed a method to transfer mechanically exfoliated graphene on SiO_2 by water intercalation, the so-called wedging transfer technique. In their method, they brought a hydrophobic polymer layer on top of the graphene and then immersed the system in water. After the polymer with the graphene detached from the SiO_2 due to water intercalation, it was positioned on the target substrate. When the polymer is dissolved, the graphene remains on top of the target substrate. A similar method was developed for MoS_2, where water intercalation between MoS_2 and a sapphire substrate resulted in the detachment of a polystyrene coated MoS_2 layer.[28]

The bubbling transfer method is another technique to transfer graphene.[29] In this method, electrochemical means are used to detach graphene from a substrate. First, a substrate with CVD graphene is coated with polymethyl methacrylate (PMMA). The use of PMMA prevents the graphene from rolling or tearing during the delamination process. Thereafter, the sample is immersed in water. The water intercalates between graphene and the substrate. When a negative potential is applied to the substrate, the

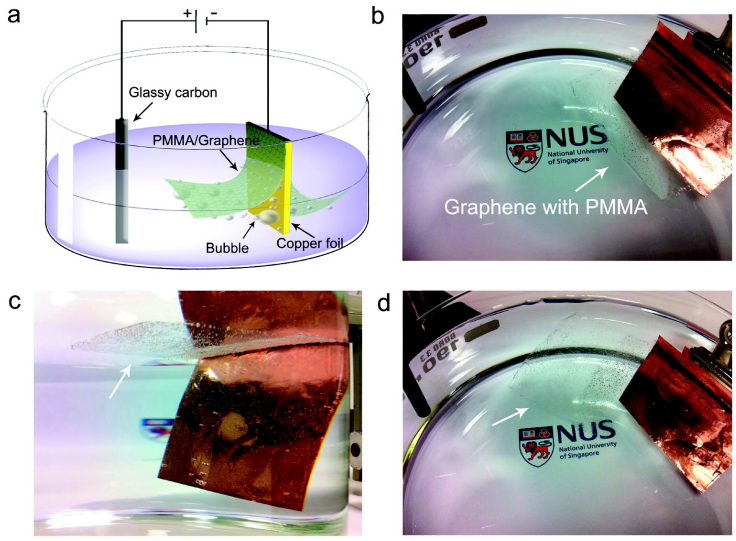

Figure 2.2: (a) Schematic illustration of the electrochemical cell used for the electrochemical exfoliation. (b-d) Consecutive optical images of the graphene/PMMA being delaminated from the copper foil. The PMMA covered graphene eventually fully delaminates from the copper foil. Reprinted with permission from ref.[29] Copyright 2011 American Chemical Society.

confined water is reduced to hydrogen gas. This results in the nucleation of (nano)bubbles with a high internal pressure. These high-pressure bubbles cause the graphene to delaminate from the substrate. This method does not damage the graphene and is relatively easy to implement. Wang et al.[29] demonstrated the use of this bubbling transfer method on CVD graphene grown on a copper foil. Figure 2.2(a) shows a schematic illustration of their setup. The copper foil is used as the negative cathode. Figures 2.2(b-d) show the graphene delamination over time. Figure 2.2(d) shows the successful detachment of the graphene/PMMA. The graphene/PMMA floats in the $K_2S_2O_8$ (0.05 mM) electrolyte. This method makes the Cu etching step abundant and creates high-quality graphene films. Also, the copper catalyst can be reused and the process can be scaled to an industrial level.

Gao et al.[30] used a similar approach to detach CVD graphene from a platinum foil. Compared to copper, the advantage of platinum is its almost unlimited lifetime. Copper is namely etched away for about 40 nm per cycle,[29]

making it a less sustainable material for graphene transfer. Using platinum as the substrate, the quality of the delaminated graphene is almost identical to the original CVD graphene on platinum. Their experiment was performed in a NaOH solution. The authors noticed that when using graphene as an anode, the graphene oxidizes. The bubbling transfer method has also been demonstrated for graphene/Ru[31] and h-BN/Pt[32,33] samples.

Gupta et al.[34] developed a method for exfoliating CVD graphene from copper and platinum substrates by only using hot deionized water, the so-called soak-and-peel delamination method. In their method, hot (90 °C) deionized water penetrates into the hydrophobic graphene-hydrophilic Cu/Pt interface and induces separation. This method gives high-quality graphene with reduced doping compared to transferred graphene using an etchant or electrolyte.

Verguts et al.[35] showed that water intercalation is critical to a direct graphene transfer. The authors found that graphene delamination with the bubbling transfer method was only successful when the sample was exposed to water priorly. Graphene delamination of samples unexposed to water, directly after CVD growth, were unsuccessful and resulted in heavy damage to the graphene. With scanning tunneling microscopy, they showed that water layers intercalate between CVD graphene and $Al_2O_3(0001)$/Pt(111) when the system is exposed to water. An STM image of these water layers between CVD graphene and $Al_2O_3(0001)$/Pt(111 is shown in Figure 2.3. Before this STM image was taken, the sample was immersed in 50 °C water for 16 h. The water layers form a meandering pattern. With SEM and Raman spectroscopy the authors additionally confirmed that water intercalates between the graphene and $Al_2O_3(0001)$/Pt(111).

Dollekamp et al.[36] investigated the dynamics of confined water between charged graphene and mica. They found that a negatively charged graphene surface promotes water intercalation. On the contrary, a positively charged graphene surface resulted in water being expelled from of the graphene-mica slit pore. They attributed this effect to the preferential orientations of the water molecules due to the confinement.

In their most recent work, Verguts et al.[37] looked at the ion intercalation between graphene and platinum. They found that the ion intercalation and not the bubble formation is the driving force for graphene delamination. Graphene delamination was tested in different electrolytes. Ions which resulted in successful delamination at the cathode where: Na^+, K^+, TMA^+, and

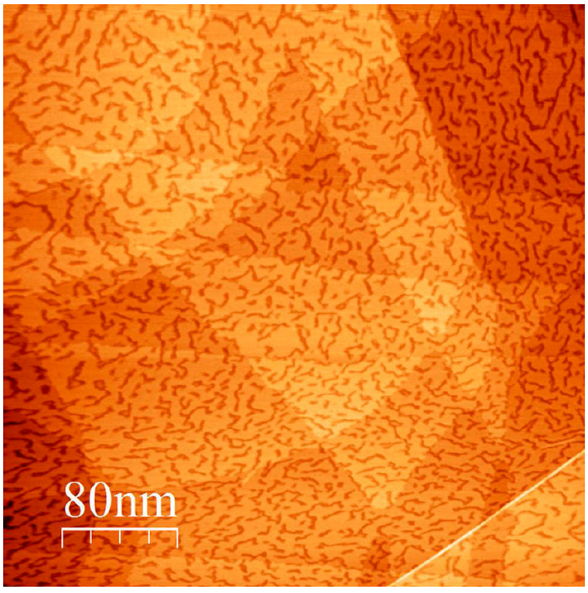

Figure 2.3: STM image under ambient conditions of graphene on $Al_2O_3(0001)/Pt(111)$. Meandering water layers are visible. The bias voltage is 105 mV and the current is 0.2 nA.[35] Copyright 2017 American Chemical Society.

TEA^+. In contrast, unsuccessful delamination at the cathode was observed with H^+, $NH_4{}^+$, and Ce^{4+} ions. The result can be explained by the difference in the electroreductive activity of the ions. The ions that delaminate the graphene have a more negative E^0 (standard reduction potential versus the standard hydrogen electrode) value compared to the E^0 value of water. Therefore, the ions can intercalate between the platinum and graphene, resulting in delamination of the graphene. The ions that not delaminate the graphene directly reduce to gases when coming in contact with the cathode. Ions with successful delamination at the anode where: $NO_3{}^-$, $SO_4{}^{2-}$, Cl^-, and $SO_3{}^{2-}$. Unsuccessful delamination at the anode was observed with OH^- ions. Again, the electroreductive activity of the ions is responsible for the difference in successful delamination. When the counter electrode was removed, and thus no current flows, the same successful delamination was achieved. In the situation without the counter electrode, even $NH_4{}^+$ causes delamination of the graphene since it cannot reduce to $NH_3(g)$ anymore. The authors also noticed that delamination takes up to three orders of magnitude longer at positively charged electrodes, compared to negatively charged electrodes. This may be explained by water expelled out of the confined space between graphene and the positively charged platinum, similar to the observations made by Dollekamp et al.[36] for water confined between mica and positively charged graphene.

2.7 Liquid phase exfoliation

There are several techniques to exfoliate graphene in the liquid phase.[38] Graphene can be exfoliated by oxidizing it with oxidizing chemicals to graphene-oxide, the so-called chemical exfoliation.[39] Its hydrophilicity allows water to intercalate between the graphene-oxide layers. Ultrasonication is then applied to agitate the layers. Afterward, the graphene-oxide layers are reduced back to graphene. Besides water, also ions can intercalate between 2D materials.[40,41] The intercalation increases the spacing between the layers and thus lowers the interlayer attraction. Ultrasonication or thermal shock[42] can then be used to agitate the layers. This process is schematically depicted in Figure 2.4(a). Ions could be exchanged in, e.g., clays, layered double hydroxides, and metal oxides.[43] These materials have counter-ions in between the layers to establish charge neutrality. The ions can then be exchanged for larger ions. This increases the interlayer spacing which is needed to agi-

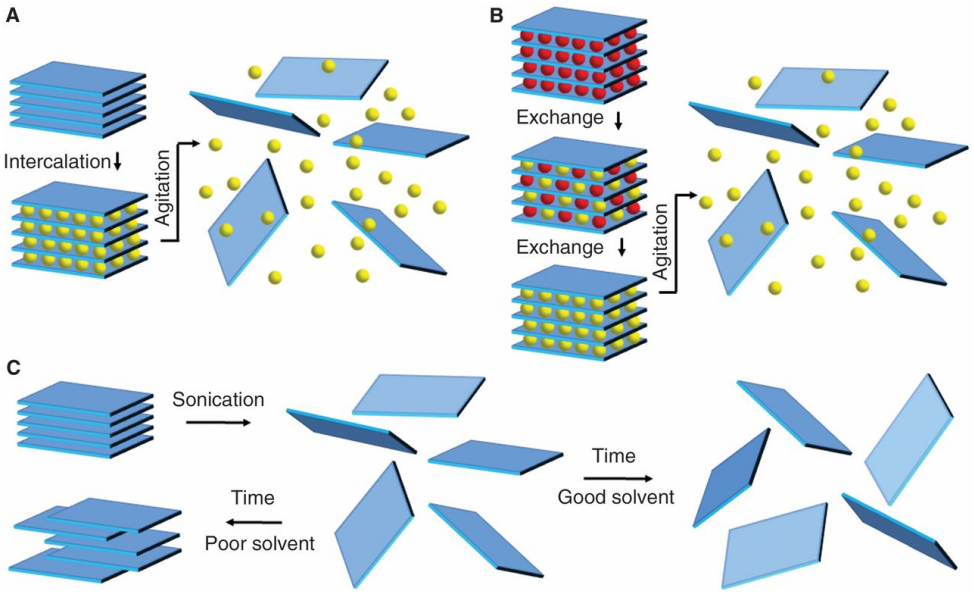

Figure 2.4: Different liquid exfoliation methods. (a) Ion intercalation. (b) Ion exchange. (c) Sonication-assisted exfoliation. Reprinted with permission from ref.[38] Copyright 2013 American Association for the Advancement of Science.

tate the layers with, e.g., ultrasonication or shear mixing. This process is schematically represented in Figure 2.4(b).

Hernandez et al.[44] managed to exfoliate graphene from powdered graphite by means of liquid phase exfoliation. This method is also sometimes called sonication assisted exfoliation. The authors of reference[44] used solvents (e.g. N-methylpyrrolidone) with a similar surface energy as graphene, leading to solvent intercalation between the layers in graphite. This intercalation results in an increased interlayer distance and lowering of the crystal cohesion. With ultrasonication, cavitation bubbles arise which agitate the layers. By choosing the right solvent, the layers are prevented from reaggregation. A monolayer yield of $\sim$1 wt% was achieved. This process is schematically depicted in Figure 2.4(c). The method has also been demonstrated to be successful for h-BN, TMD's and TMO's.[45]

Su et al.[46] used electrochemistry to exfoliate graphene from graphite. They immersed a graphite electrode in sulfuric acid and then applied a potential to

the electrode. This resulted in the intercalation of SO_4^{2-} ions in the graphite. Their obtained graphene sheets have a lateral size of 30 μm and exhibit a modest conductivity with a mobility of 17 $cm^2/V{\cdot}s$.

The influence of chemical, sonication assisted and electrochemical exfoliation on the remaining graphite was studied by Xia et al.[47] They used AFM, Raman and X-ray diffraction to study the exfoliated graphene and remaining graphite. Sonication assisted exfoliation resulted in the best quality flakes and minimal damage to only the top layers of the remaining graphite. Since this method only exfoliates the top graphene layers, this exfoliation method is rather slow. Chemical and electrochemical assisted exfoliation are faster exfoliation methods and act in depth in the graphite. However, these methods resulted in more defects to the graphene.

Bibliography

[1] Surwade, S. P.; Smirnov, S. N.; Vlassiouk, I. V.; Unocic, R. R.; Veith, G. M.; Dai, S.; Mahurin, S. M. Water Desalination using Nanoporous Single-Layer Graphene. *Nat. Nanotechnol.* **2015**, *10*, 459–464.

[2] Cohen-Tanugi, D.; Grossman, J. C. Water Desalination across Nanoporous Graphene. *Nano Lett.* **2012**, *12*, 3602–3608.

[3] O'Hern, S. C.; Boutilier, M. S. H.; Idrobo, J.-C.; Song, Y.; Kong, J.; Laoui, T.; Atieh, M.; Karnik, R. Selective Ionic Transport through Tunable Subnanometer Pores in Single-Layer Graphene Membranes. *Nano Lett.* **2014**, *14*, 1234–1241.

[4] O'Hern, S. C.; Jang, D.; Bose, S.; Idrobo, J.-C.; Song, Y.; Laoui, T.; Kong, J.; Karnik, R. Nanofiltration Across Defect-Sealed Nanoporous Monolayer Graphene. *Nano Lett.* **2015**, *15*, 3254–3260.

[5] O'Hern, S. C.; Stewart, C. A.; Boutilier, M. S. H.; Idrobo, J.-C.; Bhaviripudi, S.; Das, S. K.; Kong, J.; Laoui, T.; Atieh, M.; Karnik, R. Selective Molecular Transport through Intrinsic Defects in a Single Layer of CVD Graphene. *ACS Nano* **2012**, *6*, 10130–10138.

[6] Joshi, R. K.; Carbone, P.; Wang, F.-C.; Kravets, V. G.; Su, Y.; Grigorieva, I. V.; Wu, H. A.; Geim, A. K.; Nair, R. R. Precise and Ultrafast

Molecular Sieving Through Graphene Oxide Membranes. *Science* **2014**, *343*, 752–754.

[7] Nair, R. R.; Wu, H. A.; Jayaram, P. N.; Grigorieva, I. V.; Geim, A. K. Unimpeded Permeation of Water Through Helium-Leak–Tight Graphene-Based Membranes. *Science* **2012**, *335*, 442–444.

[8] Mi, B. Graphene Oxide Membranes for Ionic and Molecular Sieving. *Science* **2014**, *343*, 740–742.

[9] Liu, H.; Wang, H.; Zhang, X. Facile Fabrication of Freestanding Ultrathin Reduced Graphene Oxide Membranes for Water Purification. *Adv. Mater.* **2014**, *27*, 249–254.

[10] others„ et al. Tunable Sieving of Ions Using Graphene Oxide Membranes. *Nat. Nanotechnol.* **2017**, *12*, 546.

[11] Werber, J. R.; Osuji, C. O.; Elimelech, M. Materials for Next-Generation Desalination and Water Purification Membranes. *Nat. Rev. Mat.* **2016**, *1*, 16018.

[12] Feng, J.; Graf, M.; Liu, K.; Ovchinnikov, D.; Dumcenco, D.; Heiranian, M.; Nandigana, V.; Aluru, N. R.; Kis, A.; Radenovic, A. Single-Layer MoS_2 Nanopores as Nanopower Generators. *Nature* **2016**, *536*, 197.

[13] Siria, A.; Bocquet, M.-L.; Bocquet, L. New Avenues for the Large-Scale Harvesting of Blue Energy. *Nat. Rev. Chem.* **2017**, *1*, 0091.

[14] Siria, A.; Poncharal, P.; Biance, A.-L.; Fulcrand, R.; Blase, X.; Purcell, S. T.; Bocquet, L. Giant Osmotic Energy Conversion Measured in a Single Transmembrane Boron Nitride Nanotube. *Nature* **2013**, *494*, 455.

[15] Walker, M. I.; Ubych, K.; Saraswat, V.; Chalklen, E. A.; Braeuninger-Weimer, P.; Caneva, S.; Weatherup, R. S.; Hofmann, S.; Keyser, U. F. Extrinsic Cation Selectivity of 2D Membranes. *ACS Nano* **2017**, *11*, 1340–1346.

[16] Lim, C. H. Y. X.; Sorkin, A.; Bao, Q.; Li, A.; Zhang, K.; Nesladek, M.; Loh, K. P. A Hydrothermal Anvil Made of Graphene Nanobubbles on Diamond. *Nat. Commun.* **2013**, *4*, 1556.

[17] Lim, C. H. Y. X.; Nesladek, M.; Loh, K. P. Observing High-Pressure Chemistry in Graphene Bubbles. *Angew. Chem., Int. Ed.* **2014**, *53*, 215–219.

[18] Kayal, A.; Chandra, A. Infrared Spectral and Dynamical Properties of Water Confined in Nanobubbles at Hybrid Interfaces of Diamond and Graphene: A Molecular Dynamics Study. *J. Phys. Chem. C* **2017**, *121*, 23455–23462.

[19] Dollekamp, E.; Bampoulis, P.; Poelsema, B.; Zandvliet, H. J. W.; Kooij, E. S. Electrochemically Induced Nanobubbles between Graphene and Mica. *Langmuir* **2016**, *32*, 6582–6590.

[20] An, H.; Tan, B. H.; Moo, J. G. S.; Liu, S.; Pumera, M.; Ohl, C.-D. Graphene Nanobubbles Produced by Water Splitting. *Nano Lett.* **2017**, *17*, 2833–2838.

[21] Shin, D.; Park, J. B.; Kim, Y.-J.; Kim, S. J.; Kang, J. H.; Lee, B.; Cho, S.-P.; Hong, B. H.; Novoselov, K. S. Growth Dynamics and Gas Transport Mechanism of Nanobubbles in Graphene Liquid Cells. *Nat. Commun.* **2015**, *6*, 6068.

[22] Park, J. B.; Shin, D.; Kang, S.; Cho, S.-P.; Hong, B. H. Distortion in Two-Dimensional Shapes of Merging Nanobubbles: Evidence for Anisotropic Gas Flow Mechanism. *Langmuir* **2016**, *32*, 11303–11308.

[23] Yuk, J. M.; Park, J.; Ercius, P.; Kim, K.; Hellebusch, D. J.; Crommie, M. F.; Lee, J. Y.; Zettl, A.; Alivisatos, A. P. High-Resolution EM of Colloidal Nanocrystal Growth Using Graphene Liquid Cells. *Science* **2012**, *336*, 61–64.

[24] Chen, Q.; Smith, J. M.; Park, J.; Kim, K.; Ho, D.; Rasool, H. I.; Zettl, A.; Alivisatos, A. P. 3D Motion of DNA-Au Nanoconjugates in Graphene Liquid Cell Electron Microscopy. *Nano Lett.* **2013**, *13*, 4556–4561.

[25] Olson, E. J.; Ma, R.; Sun, T.; Ebrish, M. A.; Haratipour, N.; Min, K.; Aluru, N. R.; Koester, S. J. Capacitive Sensing of Intercalated H_2O Molecules Using Graphene. *ACS Appl. Mater. Interfaces* **2015**, *7*, 25804–25812.

[26] Seah, C.-M.; Vigolo, B.; Chai, S.-P.; Mohamed, A. R. Transfer of Wafer-Scale Graphene onto Arbitrary Substrates: Steps Towards the Reuse and Recycling of the Catalyst. *2D Mater.* **2018**, *5*, 042001.

[27] Schneider, G. F.; Calado, V. E.; Zandbergen, H.; Vandersypen, L. M. K.; Dekker, C. Wedging Transfer of Nanostructures. *Nano Lett.* **2010**, *10*, 1912–1916.

[28] Gurarslan, A.; Yu, Y.; Su, L.; Yu, Y.; Suarez, F.; Yao, S.; Zhu, Y.; Ozturk, M.; Zhang, Y.; Cao, L. Surface-Energy-Assisted Perfect Transfer of Centimeter-Scale Monolayer and Few-Layer MoS_2 Films onto Arbitrary Substrates. *ACS Nano* **2014**, *8*, 11522–11528.

[29] Wang, Y.; Zheng, Y.; Xu, X.; Dubuisson, E.; Bao, Q.; Lu, J.; Loh, K. P. Electrochemical Delamination of CVD-Grown Graphene Film: Toward the Recyclable Use of Copper Catalyst. *ACS Nano* **2011**, *5*, 9927–9933.

[30] Gao, L.; Ren, W.; Xu, H.; Jin, L.; Wang, Z.; Ma, T.; Ma, L.-P.; Zhang, Z.; Fu, Q.; Peng, L.-M. Repeated Growth and Bubbling Transfer of Graphene with Millimetre-size Single-crystal Grains Using Platinum. *Nat. Commun.* **2012**, *3*, 699.

[31] Koren, E.; Sutter, E.; Bliznakov, S.; Ivars-Barcelo, F.; Sutter, P. Isolation of High Quality Graphene from Ru by Solution Phase Intercalation. *Appl. Phys. Lett.* **2013**, *103*, 121602.

[32] Kim, G.; Jang, A.-R.; Jeong, H. Y.; Lee, Z.; Kang, D. J.; Shin, H. S. Growth of High-Crystalline, Single-Layer Hexagonal Boron Nitride on Recyclable Platinum Foil. *Nano Lett.* **2013**, *13*, 1834–1839.

[33] Gao, Y.; Ren, W.; Ma, T.; Liu, Z.; Zhang, Y.; Liu, W.-B.; Ma, L.-P.; Ma, X.; Cheng, H.-M. Repeated and Controlled Growth of Monolayer, Bilayer and Few-Layer Hexagonal Boron Nitride on Pt Foils. *ACS Nano* **2013**, *7*, 5199–5206.

[34] Gupta, P.; Dongare, P. D.; Grover, S.; Dubey, S.; Mamgain, H.; Bhattacharya, A.; Deshmukh, M. M. A Facile Process for Soak-and-Peel Delamination of CVD Graphene from Substrates Using Water. *Sci. Rep.* **2014**, *4*, 3882.

[35] Verguts, K.; Schouteden, K.; Wu, C.-H.; Peters, L.; Vrancken, N.; Wu, X.; Li, Z.; Erkens, M.; Porret, C.; Huyghebaert, C.; Van Haesendonck, C.; De Gendt, S.; Brems, S. Controlling Water Intercalation Is Key to a Direct Graphene Transfer. *ACS Appl. Mater. Interfaces* **2017**, *9*, 37484–37492.

[36] Dollekamp, E.; Bampoulis, P.; Faasen, D. P.; Zandvliet, H. J. W.; Kooij, E. S. Charge Induced Dynamics of Water in a Graphene-Mica Slit Pore. *Langmuir* **2017**, *33*, 11977–11985.

[37] Verguts, K.; Coroa, J.; Huyghebaert, C.; De Gendt, S.; Brems, S. Graphene Delamination Using 'Electrochemical Methods': An Ion Intercalation Effect. *Nanoscale* **2018**, *10*, 5515–5521.

[38] Nicolosi, V.; Chhowalla, M.; Kanatzidis, M. G.; Strano, M. S.; Coleman, J. N. Liquid Exfoliation of Layered Materials. *Science* **2013**, *340*, 1226419.

[39] Dreyer, D. R.; Park, S.; Bielawski, C. W.; Ruoff, R. S. The Chemistry of Graphene Oxide. *Chem. Soc. Rev.* **2010**, *39*, 228–240.

[40] Shih, C.-J.; Vijayaraghavan, A.; Krishnan, R.; Sharma, R.; Han, J.-H.; Ham, M.-H.; Jin, Z.; Lin, S.; Paulus, G. L.; Reuel, N. F.; Hua Wang, Q.; Blankschtein, D.; Strano, M. S. Bi-and Trilayer Graphene Solutions. *Nat. Nanotechnol.* **2011**, *6*, 439.

[41] Eda, G.; Yamaguchi, H.; Voiry, D.; Fujita, T.; Chen, M.; Chhowalla, M. Photoluminescence from Chemically Exfoliated MoS_2. *Nano Lett.* **2011**, *11*, 5111–5116.

[42] Nikitin, Y. A.; Pyatkovskii, M. L. Formation and Properties of Materials Based on Thermally Expanded Graphite. *Powder Metall. Metal. C+* **1997**, *36*, 41–45.

[43] Ma, R.; Sasaki, T. Nanosheets of Oxides and Hydroxides: Ultimate 2D Charge Bearing Functional Crystallites. *Adv. Mater.* **2010**, *22*, 5082–5104.

[44] Hernandez, Y. et al. High-yield Production of Graphene by Liquid-Phase Exfoliation of Graphite. *Nat. Nanotechnol.* **2008**, *3*, 563–568.

[45] Coleman, J. N. et al. Two-Dimensional Nanosheets Produced by Liquid Exfoliation of Layered Materials. *Science* **2011**, *331*, 568–571.

[46] Su, C.-Y.; Lu, A.-Y.; Xu, Y.; Chen, F.-R.; Khlobystov, A. N.; Li, L.-J. High-Quality Thin Graphene Films from Fast Electrochemical Exfoliation. *ACS Nano* **2011**, *5*, 2332–2339.

[47] Xia, Z. Y.; Pezzini, S.; Treossi, E.; Giambastiani, G.; Corticelli, F.; Morandi, V.; Zanelli, A.; Bellani, V.; Palermo, V. The Exfoliation of Graphene in Liquids by Electrochemical, Chemical, and Sonication Assisted Techniques: A Nanoscale Study. *Adv. Funct. Mater.* **2013**, *23*, 4684–4693.

3

Experimental techniques

3.1 Atomic force microscopy

Atomic force microscopy (AFM) was invented by Binnig et al. in 1986.[1] It is a scanning probe technique in which nanometer resolution can be obtained, beyond the optical diffraction limit of light. In AFM, a sharp tip, which is located at the end of a flexible cantilever, scans the surface. The cantilever is positioned at the end of an AFM chip. An optical image of a typical AFM chip, cantilever and tip can be seen in Figure 3.1(a),(b) and (c), respectively. The interaction of the tip with the surface results in a deflection of the cantilever. The most common method to read out the cantilever deflection is by shining a laser at the backside of the cantilever, near the tip, and to detect the reflection with a photodiode detector.[2] This method is schematically depicted in Figure 3.1(d). A piezoelectric element is used to move the tip in the x,y,z-direction. The z-position is controlled with an active feedback loop, such that the vertical deflection on the photodiode detector remains constant. A significant advantage of AFM over scanning tunneling microscopy (STM) is that AFM can also be used to study insulating surfaces. Furthermore, scans can be performed in ambient as well in liquid environments.

All measurements in this thesis are performed with an Agilent 5100 AFM, see Figure 3.1(e). The heart of the Agilent 5100 AFM is the AFM scanner. It consists of a piezoelectric element on which the AFM chip can be mounted with a retainer spring. Inside the AFM scanner, also the laser and photodiode detector are located. The sample stage is located below the AFM scanner, on which the sample can be mounted. This sample stage can also be moved in the x,y,z-direction. The sample is mounted with double sided tape to

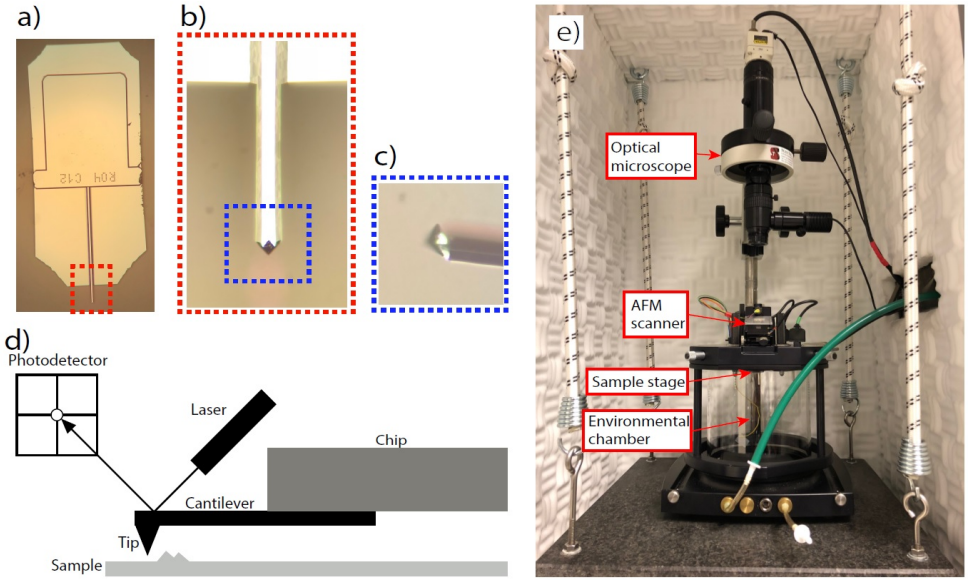

Figure 3.1: (a) A 5x zoom image of an SSS-FMR AFM probe. The width of the chip is 1.6 mm. (b) A 50x zoom image of an SSS-FMR AFM cantilever. The width, length and thickness of the cantilever are 30 μm, 225 μm and 3 μm, respectively. (c) A 50x zoom image of a diagonal view of a SSS-FMR AFM tip. The height of the tip is 15 μm. (d) A schematic illustration of an AFM. (e) Photo of an Agilent 5100 AFM.

the sample stage, so it is well attached. A not properly attached sample namely results in unstable AFM scans. The sample stage is positioned in an environmental chamber, in which the environment can be changed to for example a nitrogen or alcohol environment. At the top of the AFM, an optical microscope is positioned. This microscope is used to find the exact location of graphene flakes on the sample.

The AFM can be operated in different modes. The modes used in this thesis are contact and tapping mode, which will be addressed in the next subsections.

3.1.1 Contact mode

In contact mode, the AFM tip is in contact with the surface. When the tip approaches the surface, the tip will eventually snap into contact. During scanning, when an elevated region is scanned, the vertical deflection of the cantilever, and therefore the vertical deflection voltage of the photodiode detector, will increase due to normal forces acting on the tip. With a feedback loop, the vertical deflection voltage can be kept constant by adjusting the z-piezo of the scanner. The change in z-position of the z-piezo then reflects the topographic information of the sample. A disadvantage of contact mode is the risk of damage by the sharp AFM tip, especially when high normal forces are applied. Besides the vertical deflection, also the lateral deflection can be obtained in contact mode. We will elaborate on the lateral deflection in the next subsection.

3.1.2 Lateral force microscopy

In lateral force microscopy (LFM), lateral forces acting on the tip are measured. The lateral force results in lateral bending (twisting) of the cantilever. This lateral bending is detected by the a change of the horizontal deflection voltage at the photodiode detector. A change in lateral deflection can indicate a change in friction or height, see Figure 3.2(a). In this figure, the blue surface indicates a material with a higher friction. To discriminate between the friction and the height, the lateral trace and retrace scan, the so-called friction loop, should be analyzed. Figure 3.2(b) and (c) show the lateral deflection voltage trace and retrace, respectively. At the location with a higher friction, the trace and retrace scan have an opposite sign. At the location with a height difference, the trace and retrace scan have the same sign. Therefore, subtraction of the trace and retrace scan cancels out the height signal. The remaining signal should be divided by two to obtain the friction signal. The conversion of the friction signal voltage to the friction force is not straightforward and is discussed in the next subsection.

3.1.3 Lateral force calibration

The friction force F_L can be determined by using the improved wedge calibration method of Varenberg et al.[3] This method is based on the wedge calibration method of Ogletree et al.[4] In this method, the half-width of the

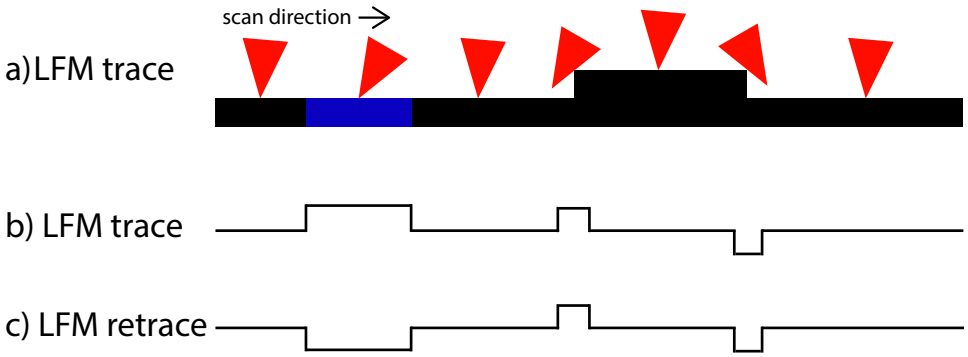

Figure 3.2: (a) Schematic illustration of a LFM experiment. The blue surface indicates a different material with a higher friction. (b) Lateral trace line profile. (c) Lateral retrace line profile.

experimentally observed friction loop W_{exp} is converted to the friction force with a lateral calibration constant α, see equation (3.1):

$$F_L = \alpha W_{exp} \tag{3.1}$$

This method is a direct calibration method, which means that no knowledge of the lateral spring constant k_L is required.

Lateral calibration constant

The lateral calibration constant α can be obtained by determining several frictional characteristics of a calibration sample. We used a TGF11 silicon calibration grating (MikroMasch), which has trapezoidal steps under an angle θ of 54.74°. The following frictional characteristics of the calibration sample have been determined:

- W_{slope}, the half-width of the friction loop on the sloped surface
- W_{flat}, the half-width of the friction loop on the flat surface
- Δ, the friction loop offset of the sloped surface compared to the flat surface
- F_N, the normal force

- F_A, the adhesion force

From these parameters the friction coefficient of the sloped surface μ can be determined using equation (3.2):

$$\sin\theta(F_N\cos\theta + F_A)\mu^2 - \frac{\Delta}{W_{slope}}(F_N + F_A\cos\theta)\mu + F_N\sin\theta\cos\theta = 0 \quad (3.2)$$

This second order polynomial equation can be solved with e.g. Matlab and has two solutions. The real solution must be smaller than $1/\tan(\theta)$. If both values of μ satisfy this condition, both solutions have to be inserted in equation (3.3) to obtain α:

$$\alpha = \frac{1}{W_{slope}}\frac{\mu(F_N + F_A\cos\theta)}{(\cos^2\theta - \mu^2\sin^2\theta)} \quad (3.3)$$

When two values for α are obtained, these values have to be inserted in equation (3.4):

$$\mu_{flat} = \frac{\alpha W_{flat}}{F_N + F_A}, \quad (3.4)$$

where μ_{flat} is the friction coefficient of the flat surface. The α value which results in the smallest difference between μ_{flat} and μ should be taken as the lateral calibration constant.

Normal force

The normal force F_N to the sample during the measurement is determined from equation (3.5):

$$F_N = k_N S_N U_N, \quad (3.5)$$

where k_N is the normal spring constant of the cantilever, S_N is the normal deflection sensitivity and U_N is the vertical deflection voltage. k_N is given by the manufacturer of the AFM tip, S_N is obtained by taking the inverse slope of the force-distance curve in the contact regime and U_N is the voltage difference between the contact setpoint and the scanning setpoint.

Adhesion force

The adhesion force F_A of the cantilever to the sample during the calibration is determined from equation (3.6):

$$F_A = k_N S_N U_A, \tag{3.6}$$

where U_A is the voltage difference between the contact setpoint and the voltage point when the cantilever jumps out of contact.

3.1.4 Tapping mode

In tapping mode the tip oscillates, slightly tapping the surface. The advantage of tapping mode over contact mode is that the forces on the surface are lower. Therefore, damage of the surface is less likely. Furthermore, soft features like nanodroplets can now be scanned since the tip hardly deforms the surface. The cantilever is often brought acoustically into oscillation, via a piezo element inside the AFM scanner. In our measurements, we modulate the amplitude of the tip oscillation.[5] Out of contact, the tip oscillates at its resonance frequency and with its free amplitude. The drive frequency is set at or near the resonance frequency. When approaching, the resonance frequency shifts to lower frequencies in the attractive van der Waals regime, and to higher frequencies in the repulsive van der Waals regime. When the tip approaches the surface, also the amplitude of the tip lowers, due to tip-sample interactions. The tip approach stops when the setpoint amplitude is reached. The setpoint amplitude is often set at 90% of the free amplitude. With a feedback loop, the setpoint amplitude can be maintained by adjusting the z-piezo of the scanner. The change in z-position of the z-piezo then reflects the topographic information of the sample. Besides the amplitude, also the phase of the cantilever oscillation can be obtained in tapping mode. A change in phase correlates to a different energy dissipation of the tip, and indicates a change in the elastic properties of the surface. Therefore, phase imaging can be used to differentiate materials on a sample.

3.2 Sample preparation and characterization

We used the mechanical exfoliation method to obtain graphene flakes.[6–8] A piece of highly orientated pyrolytic graphite (grade ZYB, MikroMasch)

was cleaved using Scotch Tape. The remaining vertical standing flakes were removed from the HOPG with a clean tweezer without the use of Scotch Tape, the so-called tape free method.[9] The flakes were positioned and gently pressed on a muscovite mica substrate (SPI, V1). On one part was not pressed on, so that the flakes could be picked up again and removed. Some layers of graphene remained attached to the mica substrate. The layers of graphene were first studied with an optical microscope (Leica DM2500 MH). Figure 3.3(a) shows a 50x magnified optical reflection microscopy image of a graphene on mica substrate. In this setup, both objective and CCD camera (PCO Pixelfly) are positioned above the sample.[10] Monolayer graphene is 97.7% transparent,[11] so a small contrast can be observed at these locations. The darker parts represent a low number of graphene layers. Areas of few layer graphene are always located at the edges of a bigger flake. To enhance contrast, the sample can be flipped, as can be seen in Figure 3.3(b). The contrast is enhanced because the reflected light from the mica-graphene and graphene-air interface destructively interfere with each other. The dot in the red square area is due to a particle on the lens of the microscope objective.

After areas of few layer graphene are located, the sample is placed in the AFM. Figure 3.3 shows an AFM topography scan of the red dotted square area in Figure 3.3(b). The few-layer graphene area is detected in this AFM image. The sample only has an area with bilayer graphene (BLG) and no single layer graphene. However, the optical and AFM images clearly show the method that we used. A larger HOPG flake is manually positioned on the sample with tweezers to establish an electrical contact. Therfore, the flake has to be visible with the bare eye. Moreover, the flake has to be large enough to place the large HOPG flake on the flake of interest by hand movement. Note that the HOPG flake in Figure 3.3(a) is too small to connect to a larger HOPG flake.

Detecting a monolayer of graphene is not straightforward.[12] Graphene has a thickness of 0.335 nm.[13] In contact and tapping mode, when the height of graphene is measured, the AFM tip has a different interaction with graphene and the mica surface. This can result in inaccurate height measurements. The best method is to compare graphene with its folded counterpart. The folds can be present after exfoliation or created by scanning in contact mode and applying a significant normal force to an edge of a graphene layer. The step height of the folded to unfolded region then correspond to the thickness of the graphene.

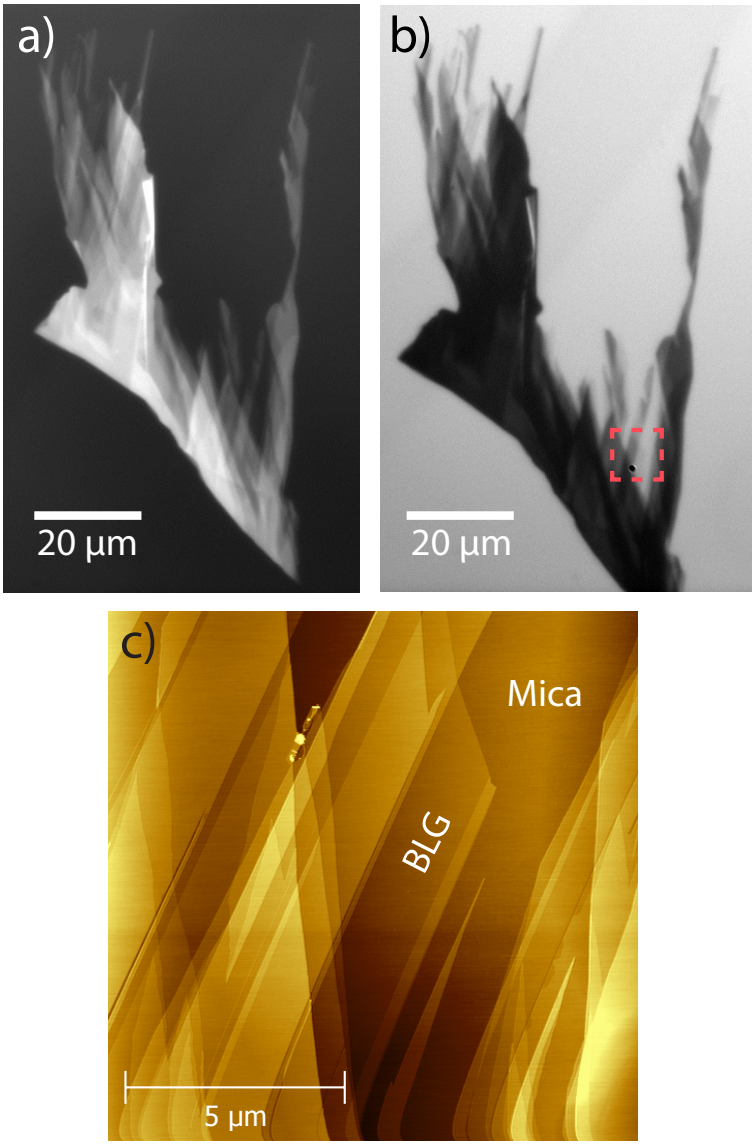

Figure 3.3: (a) Optical microscopy image of a graphene on mica sample. (b) Optical microscopy image of a flipped graphene on mica sample. (c) AFM topography image of the dotted area in (b). A few layer graphene area can be detected.

All our work presented in the thesis is reproducible. We reproduced our results at least once for every type of measurement.

Bibliography

[1] Binnig, G.; Quate, C. F.; Gerber, C. Atomic Force Microscope. *Phys. Rev. Lett.* **1986**, *56*, 930.

[2] Meyer, G.; Amer, N. M. Novel Optical Approach to Atomic Force Microscopy. *Appl. Phys. Lett.* **1988**, *53*, 1045–1047.

[3] Varenberg, M.; Etsion, I.; Halperin, G. An Improved Wedge Calibration Method for Lateral Force in Atomic Force Microscopy. *Rev. Sci. Instrum.* **2003**, *74*, 3362–3367.

[4] Ogletree, D. F.; Carpick, R. W.; Salmeron, M. Calibration of Frictional Forces in Atomic Force Microscopy. *Rev. Sci. Instrum.* **1996**, *67*, 3298–3306.

[5] Martin, Y.; Williams, C. C.; Wickramasinghe, H. K. Atomic Force Microscope-Force Mapping and Profiling on a Sub 100-Å Scale. *J. Appl. Phys.* **1987**, *61*, 4723–4729.

[6] Novoselov, K. S.; Geim, A. K.; Morozov, S. V.; Jiang, D.; Zhang, Y.; Dubonos, S. V.; Grigorieva, I. V.; Firsov, A. A. Electric Field in Atomically Thin Carbon Films. *Science* **2004**, *306*, 666–669.

[7] Novoselov, K. S.; Jiang, D.; Schedin, F.; Booth, T. J.; Khotkevich, V. V.; Morozov, S. V.; Geim, A. K. Two-Dimensional Atomic Crystals. *Proc. Natl. Acad. Sci.* **2005**, *102*, 10451–10453.

[8] Severin, N.; Lange, P.; Sokolov, I. M.; Rabe, J. P. Reversible Dewetting of a Molecularly Thin Fluid Water Film in a Soft Graphene-Mica Slit Pore. *Nano Lett.* **2012**, *12*, 774–779.

[9] Rezania, B.; Dorn, M.; Severin, N.; Rabe, J. Influence of Graphene Exfoliation on the Properties of Water-Containing Adlayers Visualized by Graphenes and Scanning Force Microscopy. *J. Colloid Interface Sci.* **2013**, *407*, 500–504.

[10] Dorn, M.; Lange, P.; Chekushin, A.; Severin, N.; Rabe, J. P. High Contrast Optical Detection of Single Graphenes on Optically Transparent Substrates. *J. Appl. Phys.* **2010**, *108*, 106101.

[11] Nair, R. R.; Blake, P.; Grigorenko, A. N.; Novoselov, K. S.; Booth, T. J.; Stauber, T.; Peres, N. M. R.; Geim, A. K. Fine Structure Constant Defines Visual Transparency of Graphene. *Science* **2008**, *320*, 1308–1308.

[12] Nemes-Incze, P.; Osváth, Z.; Kamarás, K.; Biró, L. P. Anomalies in Thickness Measurements of Graphene and Few Layer Graphite Crystals by Tapping Mode Atomic Force Microscopy. *Carbon* **2008**, *46*, 1435–1442.

[13] Al-Jishi, R.; Dresselhaus, G. Lattice-Dynamical Model for Graphite. *Phys. Rev. B* **1982**, *26*, 4514–4522.

4

Electrochemically induced nanobubbles between graphene and mica

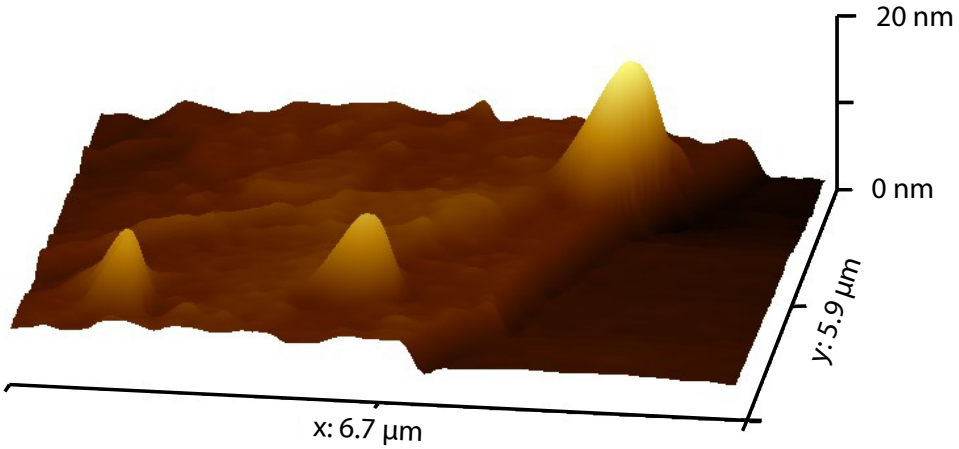

We present a new method to create *dynamic* nanobubbles. The nanobubbles are created between graphene and mica by reducing intercalated water to hydrogen. The nanobubbles have a typical radius of several hundred nanometers, a height of a few tens of nm and an internal pressure in the range of 0.5-8 MPa. Our approach paves the way to the realization of nanobubbles of which both size and internal pressure are tunable.

4.1 Introduction

Over the last decade, graphene has attracted much scientific attention.[1] Graphene is a two-dimensional (2D) material that consists of sp^2 hybridized carbon atoms arranged in a honeycomb network. It is the strongest known material and its charge carriers show an extremely high mobility.[2,3] Other important properties are its flexibility and its impermeability to gases.[2,4] These two properties have been exploited by several researchers to produce small, *static* high-pressure cavities, referred to as nanobubbles.[5–9] Nanobubbles that vary in size have already been established by applying an electric field and by light illumination.[10,11] Also small graphene sealed nano cavities have been used as pressure sensors.[12] We have developed a method in which the size of the nanobubble can be varied electrochemically.

In our method, we make use of a graphene-mica interface immersed in water, which results in the diffusion of water between the two materials.[13–17] The thickness of the graphene membrane, referred to as a graphene blanket, varied from a single layer up to a few layers. Mica is also atomically flat and — in contrast to graphene — is hydrophilic and electrically insulating.[18] Since the sample is immersed in water, electrolysis can be performed by directly applying a potential to the graphene blanket. Applying a reducing potential results in the reduction of the intercalated water to hydrogen gas:

$$2H_2O(l) + 2e^- \rightleftharpoons H_2(g) + 2OH^-(aq), \tag{4.1}$$

which eventually leads to the formation of hydrogen nanobubbles. The advantage of our method is that we work in an aqueous environment. Therefore, if needed, chemicals can be inserted into the nanobubbles. One method is to trap the chemicals during the deposition of the graphene on the mica surface. Another method to do this, is by adding the chemicals to the electrolyte. These chemicals will dissolve in the water and can diffuse between graphene and mica, if their size is not much larger than a nanometer. The chemicals will then enter the nanobubbles and react under the high pressure. The method of forming gas under a graphene blanket can also be used to study the evolution of gas from other working electrode materials and in other electrolytes at low overpotentials.

By optical microscopy and atomic force microscopy (AFM), we report compelling evidence that the nanobubbles are formed by electrolysis. Further, our results provide a strong indication that the nanobubbles grow under the

graphene blanket rather than on top. We also provide convincing evidence that the nanobubbles nucleate between graphene and mica rather than between the graphene layers. Also, we show that the pressure inside the nanobubbles is in the MPa range. Next, we show the level of control we have over the nanobubbles through applying electrochemistry. We end by studying the growth and dissolution time of the nanobubbles.

4.2 Experimental section

Samples were prepared using the mechanical exfoliation method.[13,19,20] A clean ∼2x2 cm^2 mica surface (muscovite mica; highest quality) was prepared by freshly cleaving a thick piece of mica. After this step, a freshly cleaved flake of highly oriented pyrolytic graphite (HOPG; grade ZYA, MikroMasch) was deposited on top of the mica under ambient conditions. This was achieved by gently pressing the flake at the mica surface, taking care that no scratches were formed. Next, the HOPG flake was removed from the surface of the mica, resulting in some residual layers of graphene remaining attached to the surface. This procedure was performed without use of adhesive tape, since such tapes can lead to contamination.[21] Suitable graphene flakes and the number of graphene layers were identified using optical reflection microscopy.[22,23] To establish an electrical connection from the graphene sample out of the electrochemical cell, a large HOPG flake was deposited on top of the graphene flake. This was done at the location of a thick-layered graphene area which was not otherwise of interest during the experiment. The top contacts were always tested for conductivity and showed a resistance of a few Ohms. How this large HOPG flake is connected to outside the electrochemical cell will be discussed in the next paragraph.

Figure 4.1 shows a photo of the electrochemical cell. On top of an AFM sample plate, a small white Teflon plate was placed to provide optical contrast. The sample was placed on top of the white Teflon plate. A rubber O-ring was pressed tightly onto the sample by placing an anodized aluminum liquid cell plate on top of it. This liquid cell plate was pressed tightly to the O-ring by two spring-loaded pins in combination with two cell clamps. In this arrangement, no movement of the sample due to electrostatic interactions was possible. The sample is placed in such a way that the large HOPG flake passed under the O-ring. A small tinned copper wire makes electrical contact with the HOPG flake outside the liquid cell and completes the elec-

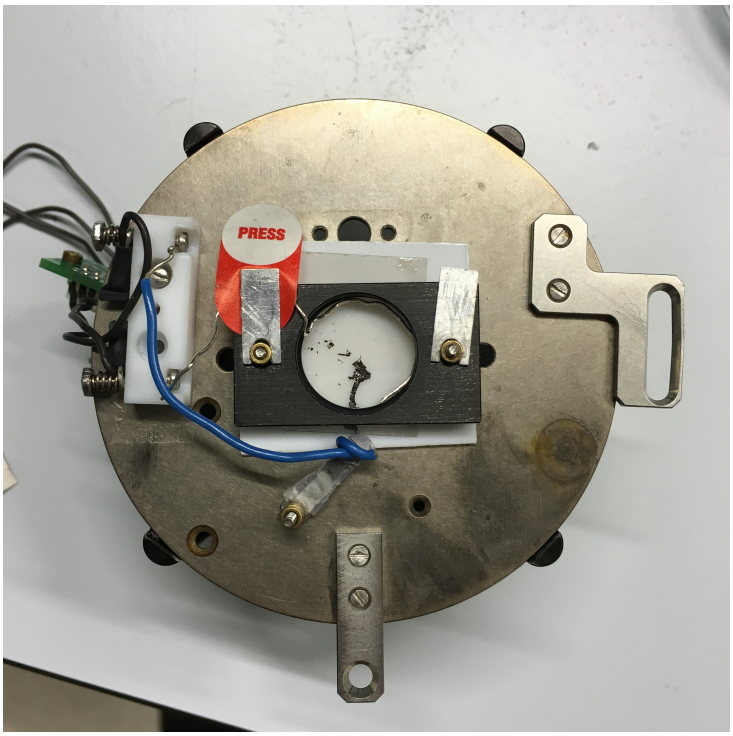

Figure 4.1: Photo of the electrochemical cell.

trical connection. The tinned copper wire was not in contact with the water. A platinum wire was inserted into the cell, which acted as a counter electrode. As the electrolyte, ∼0.7 mL purified water (Milli-Q, 18.2 MΩ·cm) was used. The water was inserted into the cell by use of a BD Discardit™ II 2 mL syringe, without a disposable needle to avoid PDMS contamination.[24] The items in contact with the water were: the sample, the rubber O-ring, the anodized aluminum liquid cell plate, the platinum wire and the AFM nose cone and the optical microscope objective.

Working in a clean manner is essential since contamination has a detrimental effect on our results. Before each measurement, the O-ring, liquid cell plate and platinum wire were cleaned. First, the items were sonicated in a 2-propanol bath (EMSURE, analytical quality) for about 10 minutes and afterwards rinsed with Milli-Q water and then blow dried with nitrogen gas.

After this cleaning step, the items were sonicated in an ethanol bath (EMSURE, analytical quality) for about 10 minutes and rinsed again thoroughly with Milli-Q water and then blow dried with nitrogen gas. The cleaning procedure was finalized by rinsing the top of the AFM nose cone with Milli-Q water and then blow dried with nitrogen gas, since this part is in contact with the electrolyte during scanning.

The precise configuration of the electrochemical cell varied between the experiments. For the measurement with the optical microscope in which we applied a voltage sweep to the sample, an electrochemical cell with a three-electrode configuration was used. In this case, a saturated calomel electrode (SCE; REF421, Radiometer Analytical) was used as the reference electrode. The three-electrode configuration was used to make a quantitative statement of the exact voltage at which the nanobubbles nucleated. For the optical microscopy experiment in which we studied the growth or dissolution dynamics and for the AFM experiments, a smaller and more convenient AFM electrochemical cell was used in a two-electrode configuration. Here the counter electrode also served as the reference electrode. This is a more controlled configuration and we can directly compare both optical and AFM experiments. In this electrochemical cell, there was no space for a large reference electrode.

Control over the electrochemical cell was achieved by using a potentiostat (Princeton Applied Research, model 273A). During the measurements in the AFM, the potentiostat was operated in the constant current mode (chronopotentiometry), in which a constant current was applied to the working electrode; graphene in our case. This mode was used since the current, which correlates to the amount of evolved hydrogen gas, could easily be substantially increased to higher values. We started with applying a current of -1 nA. Afterwards, we applied -10 nA, -100 nA, -1 μA, -10 μA and so on, until we observed the nucleation of nanobubbles. This gradual increase was needed to see the onset of the nucleation of nanobubbles. Early delamination of the graphene at a too high current (significant gas evolution rate) must be prevented since delamination hinders the nucleation of new nanobubbles in this area. During the optical microscopy experiment where we wanted to find the exact onset of the nucleation of nanobubbles, we used the voltage sweep mode to scan along a continuous range of voltages. During the optical microscopy experiment to study the growth and dissolution dynamics of the nanobubbles, the potentiostat was operated in constant current and in the

constant voltage mode (chronoamperometry). We started off by substantially increasing the current, as stated above. When we saw the nucleation of nanobubbles we increased the gas evolution more slowly. We established this by switching to constant voltage mode where we increased the voltage by steps of 0.25 V, starting from the voltage which corresponded to the current when the nanobubbles nucleated.

A small current and potential range was used during the experiments. Only small negative currents and voltages were applied to create nanobubbles in the two-electrode configuration: typically currents between -100 nA and -10 μA with matching voltages of -0.88 V and -3.19 V, respectively. When we applied higher negative currents, large hydrogen bubbles nucleated on top of the graphene blanket. Those large bubbles that grew on top hindered the opportunity to monitor the growth of nanobubbles underneath the graphene by using AFM. During the application of positive voltages to the sample, for example a voltage of 2.75 V (current was 7.5 μA), we saw with optical microscopy that besides the formation of oxygen nanobubbles, the graphene also started to oxidize. This oxidation has been studied by Matsumoto et al. and we refer to their article for more information.[25] Due to this oxidation and the limited additional information we would obtain, we decided not to study oxygen nanobubbles with AFM at lower positive potentials.

The optical experiments were carried out using a Leica DM2500 MH optical microscope in combination with a Leica HCX APO L 40x/0.80 W U-V-I objective and an EO-1312C Edmund Optics or PCO PixelFly CCD camera. This optical microscope was operated in the reflective light mode, where the microscope objective and the light source are both positioned above the sample. The AFM measurements were performed using an Agilent 5100 AFM, using intermittent contact in the constant amplitude mode. The following two AFM tips were used: (i) a NANOSENSORS™ SSS-FMR-10 (with a nominal spring-constant of 2.8 N/m and a resonance frequency of 75 kHz); and (ii) a MikroMasch HQ:NSC36/AL BS C (with a nominal spring-constant of 0.6 N/m and a resonance frequency of 65 kHz).

4.3 Results and discussion

A schematic illustration of the sample under ambient conditions is shown in Figure 4.2(a). For clarity, the AFM sample plate, the white Teflon plate, the liquid cell plate, AFM nose cone, optical microscope objective, the two

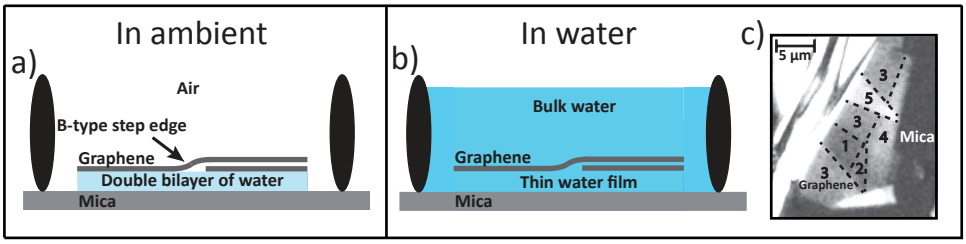

Figure 4.2: (a) Schematic illustration of the sample under ambient conditions. A double bilayer of water is always present between graphene and mica. A schematic illustration of a B-type step edge is also shown. (b) Schematic illustration of the sample in an aqueous environment. (c) An optical microscopy image of a graphene blanket on mica, immersed in water. The numbers refer to the number of graphene layers.

spring-loaded pins and the two cell clamps are omitted from the schematic illustration. The AFM nose cone or optical microscope objective was placed above the sample, also immersed in the water. The graphene in this illustration can be seen as the combination of the graphene flake and the large HOPG flake used for the electrical connection. Note the image is not to scale. Since samples were prepared under ambient conditions, a double bilayer of intercalated water is always present between the graphene and mica.[14,26,27] The layered structure of the graphene blanket is illustrated with a B-type step edge. B-type step edges are steps that are on the bottom surface of the graphene flake. At a B-type step edge, a bottom layer of graphene ends, resulting in the top layer of graphene following the topography of the bottom layer. This B-type step edge is also shown in Figure 4.2(a-b), although one has to take into account that we deal with a graphene blanket during all experiments.

In Figure 4.2(b), the sample immersed in water is schematically represented. The water on top of the graphene is referred to as the bulk water and the water intercalated between graphene and mica is designated as the thin water film. Under all circumstances the bulk water is considered to be in equilibrium with the thin water film. Since graphene is impermeable to gases, water is assumed to diffuse between graphene and mica by direct contact with the bulk water at the edge of the graphene blanket.[13–17] An optical microscopy image of the sample immersed in water is shown in Figure 4.2(c).

In that image, the numbers within the dotted areas refer to the number of graphene layers, as deduced from the optical contrast.

A schematic representation of the AFM electrochemical cell during electrolysis is given in Figure 4.3(a). Electrolysis was established by applying a voltage of -0.26 V to -3.87 V vs. SCE at a scan rate of 10 mV/s to the graphene (current varied from 13 mA to -60 mA), as shown in Figure 4.3(b). During this voltage sweep, at a potential of -3.29 V vs. SCE (current was -43.7 mA), nanobubbles nucleated under the graphene blanket, as shown in Figure 4.3(c(I)); the nanobubbles are indicated by green arrows. After 0.27 seconds, the nanobubbles conglomerated to a larger lengthened nanobubble, which is shown in Figure 4.3(c(II)). The larger lengthened nanobubble is indicated by a green arrow. After 0.96 seconds, the nanobubbles coalesced further into an equilateral triangularly shaped nanobubble, shown in Figure 4.3(c(III)). Figure 4.3(c(IV)) shows that after 1.37 seconds the gaseous domain developed further into a hexagonally shaped nanobubble. Theoretical calculations show that a point load on graphene results in the axis-symmetrical deformation of graphene[28,29]. This leads us to assume that the shape of the nanobubble is predominantly determined by the hexagonally atomic lattice symmetry of the graphene and the triangular atomic lattice symmetry of the mica.[5,10] In Figure 4.3(c(V)), 1.51 seconds after the nanobubble nucleated, the nanobubble collapsed due to delamination of the graphene from the mica towards the edge of the graphene blanket and hydrogen gas was released*. That nanobubbles nucleate shows that ion transport is still active in the thin water film. However, it remains unclear what exactly takes place between graphene and mica following reduction of the confined water. If an ionic liquid was added, instead of pure water, the onset of nanobubble nucleation would probably occur at lower voltages since the electrolyte becomes more conductive. The formation of OH^- probably results in a local pH shift and the OH^- will probably diffuse out. No defect etching was observed.

We used AFM to reconfirm that the nanobubbles grow due to electrolysis and to study the topography of these nanobubbles. Figure 4.4(a) shows an AFM image taken under ambient conditions. The step-like features, which result from the multilayer nature of the graphene blanket, are clearly visible. The dashed white square marks an area where a nanobubble will nucleate. That a nanobubble only nucleates at this location is probably related to the

*A video of this measurement can be found at
https://pubs.acs.org/doi/suppl/10.1021/acs.langmuir.6b00777

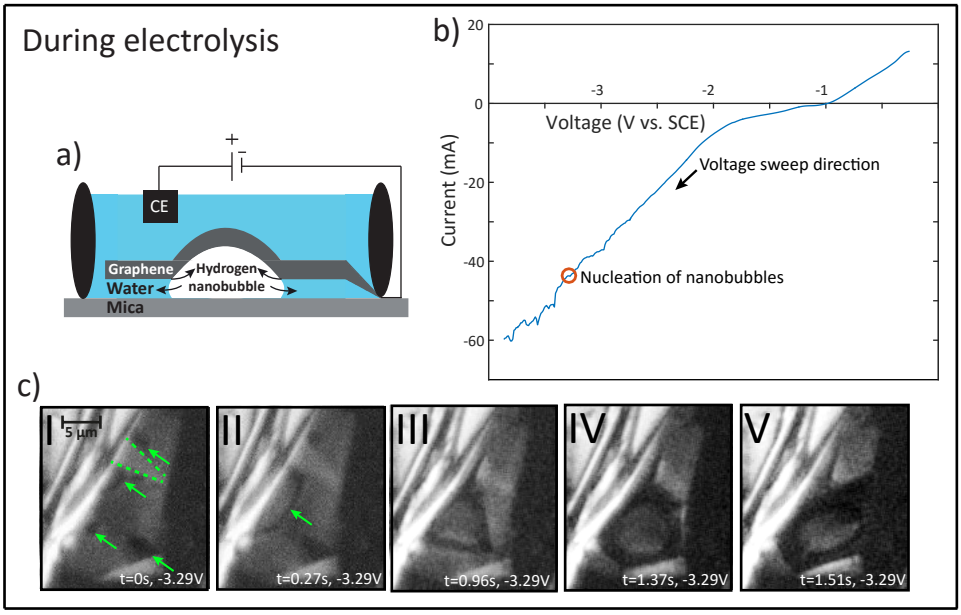

Figure 4.3: (a) Schematic illustration of the sample during electrolysis. (b) I-V curve during electrolysis. The voltage sweep was from -0.25 V to -3.87 V vs. SCE, at a scan rate of 10 mV/s. Hydrogen nanobubbles nucleated at -3.29 V vs. SCE, pointed out by the red circle. (c) Optical microscopy images of the graphene blanket on mica during electrolysis. The nucleated nanobubbles are indicated by green arrows.

presence of a B-type step edge or a defect. A graphene ripple, thus a possible defect, was seen in this area, pointed out by the white arrow. One can also see that at this location there is an elevation of the graphene, possibly by a B-type step edge or wrinkle. The graphene thickness in this area was measured by AFM to be about 15 layers thick.

Figure 4.4(b) shows an AFM image of the same area on the sample in aqueous environment. The topography of the graphene remained unchanged. Since the AFM works in liquid, the change in thickness of the water film between graphene and mica cannot be compared directly to that under ambient conditions. or During electrolysis, a change in topography was observed when a current of -100 nA was applied (voltage was -0.88 V), as shown in Figure 4.4(c(I)). This topography change is due to the nucleation of a hydrogen nanobubble between graphene and mica. The graphene at this location partly delaminates from the mica, leading to the formation of a new nanobubble. The voltage and current at which this nanobubble nucleated in the two-electrode configuration was lower compared to that in the three-electrode configuration (Figure 4.3). In the latter case, the presence of the SCE reference electrode probably led to an increase of ions which could travel through the membrane of the reference electrode into the electrolyte, thereby increasing the current. The higher voltage shown in Figure 4.3 may be related to a larger distance between the working electrode and the reference electrode as well as the counter electrode in the optical microscopy electrochemical cell. This effectively increases the resistance. Please note that the nanobubbles we viewed under AFM are smaller than those we saw under optical microscopy. Due to further evolution of hydrogen gas during prolonged electrolysis, the pressure inside the nanobubble increases, resulting in further delamination and thus growth of the nanobubble, which is shown in Figures 4.4(c(II)) and 4.4(c(III)). The size of the nanobubble slowly increased until it saturated after about 19 minutes. At this point, we assume that a dynamic equilibrium exists between the evolution of hydrogen gas into the nanobubble and the dissolution of hydrogen gas out of the nanobubble into the thin water film. The asymmetry between the top and bottom areas of the nanobubble as shown in Figures 4.4(c(II)) and 4.4(c(III)) is due to the graphene ripple, which is found precisely on top of the nanobubble. The height of the nanobubble in Figure 4.4(c(III)) is 10.9 nm and its average footprint radius is 333 nm. When the magnitude of the current was increased further to -400 nA (voltage was -1.51 V), the size of the nanobubble increased, as shown in Figure 4.4(c(IV)). At

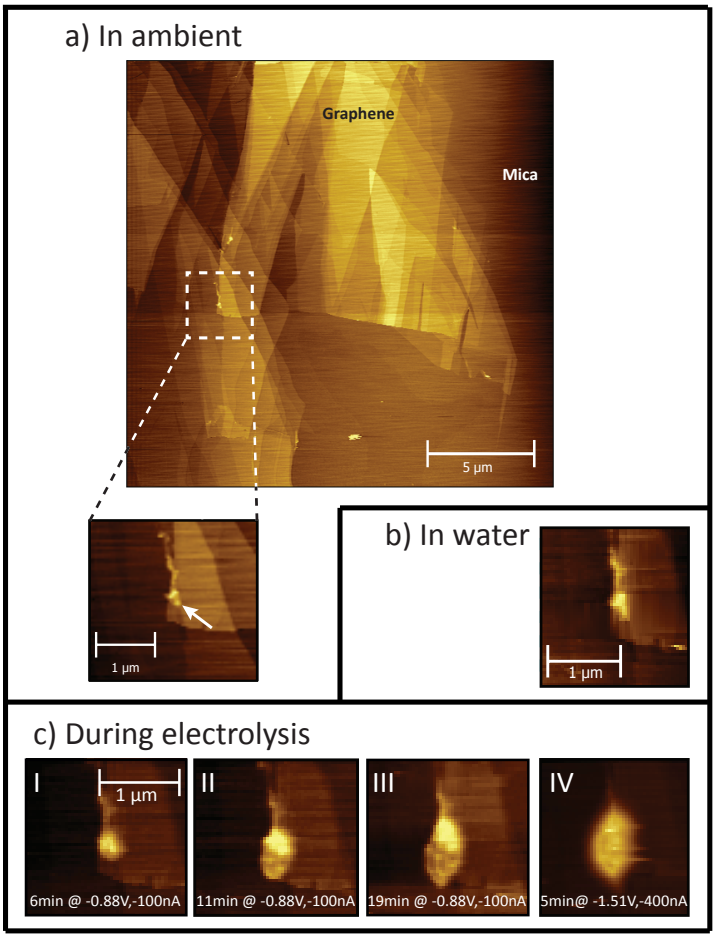

Figure 4.4: (a) AFM image of a graphene blanket on mica under ambient conditions. The dashed white square marks an area where a nanobubble will nucleate. The white arrow points out a graphene ripple. (b) AFM image of the sample immersed in water. (c) AFM images of the sample during electrolysis. A hydrogen nanobubble nucleated under the graphene blanket.

this higher current, a new dynamic equilibrium was established. The height of the nanobubble had increased to 24.5 nm and the average radius had increased to 410 nm. The footprint area of this nanobubble was 0.82 μm^2 and its volume was 9.9 attoliter. To summarize, by comparing the topography of graphene on mica under ambient conditions, in an aqueous environment and during electrolysis, we have presented compelling evidence that nanobubbles nucleate as a result of electrolysis.

Figure 4.5(a) shows an AFM image of nanobubbles of another sample. From the nanobubble shape and topography in the optical images in Figure 4.3(c) and the AFM image in Figure 4.5(a) we have a strong suggestion that we deal with nanobubbles under the graphene blanket. The matching phase image of Figure 4.5(a) is given in Figure 4.5(b). From an AFM phase image, i.e. contrast image, one normally can determine whether observed features are on top or below the graphene. In Figure 4.5(b) one can see there is a phase difference at the location of the nanobubbles. This suggests a change in elastic response of the surface, which may be related to a different material or even a particle underneath the AFM tip. However, we do not relate this phase difference to the presence of particles on the graphene surface, but rather to the AFM imaging technique. Scanning elevations at a low setpoint ratio might influence the AFM phase image.[30] The contrast between the left and right sides of the nanobubbles we interpret due to parachuting of the AFM tip. Here the AFM tip detaches from the surface in an inclined region and it takes some time until the tip lands on the same surface again.[31] Furthermore, scanning charged surfaces in aqueous environment might distort the phase image in elevated regions. Electrolysis will also increase the temperature of the water, which may also lead to a change in setpoint ratio, thus scanning conditions. Due to the curved nature of nanobubbles, convolution also might influence our AFM measurements. Actual nanobubble radii might therefore be slightly smaller.

If we would have seen nanobubbles on top of the graphene, they would have had a more spherical shape, as can be seen in literature where the authors electrolytically formed hydrogen nanobubbles on top of HOPG.[32–34] The absence of those spherical nanobubbles on top of the graphene in our experiments might be due to different scanning parameters, for example a different setpoint ratio.

Several authors have proposed that nanobubble stability on top of surfaces might be related to contact line pinning.[35,36] Nanobubble contact line pinning

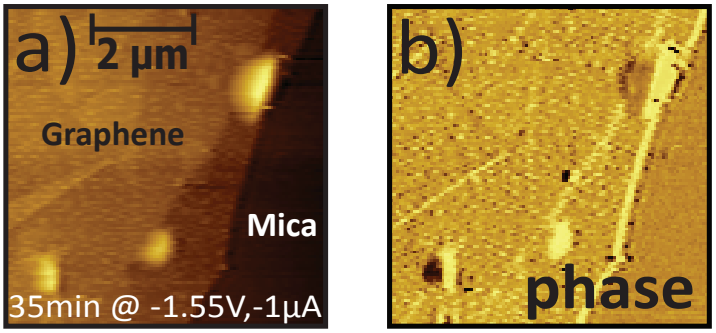

Figure 4.5: (a) AFM topography of nanobubbles under the graphene blanket. The z-limit is 0 - 22.4 nm. (b) Corresponding phase image of the nanobubbles under the graphene blanket. The z-limit is 4.3 - 104.7 degree.

is the phenomena where nanobubbles pin to a surface due to chemical and geometrical surface heterogeneities. Theoretical calculations suggest that line pinning can stabilize nanobubbles by a severe amount of magnitude.
When the nanobubbles are not pinned, they are expected to dissolve within a time τ_{life}:[37–39]

$$\tau_{\text{life}} \approx \frac{R^2 \rho_g}{3 D c_s}, \tag{4.2}$$

where R is the radius of curvature of the nanobubble, ρ_g is the gas density, D is the diffusion constant and c_s is the gas solubility; for hydrogen $\rho_g = 0.082$ kg/m^3, $D = 2.7 \times 10^{-9}$ m^2/s and $c_s = 0.0016$ kg/m^3. The radius of curvature is calculated with $R = (L^2 + 4h^2)/8h$ assuming a spherical cap shape, where L is the footprint diameter and h is the height of the nanobubble, respectively. In case of asymmetric nanobubbles we use a mean radius of curvature $\frac{1}{R_m} = \frac{1}{2}\left(\frac{1}{R'} + \frac{1}{R''}\right)$. When we use the dimensions of the nanobubble in Figure 4.4(c(IV)) and by applying a deconvolution to obtain a more accurate footprint radius, we obtain $R = 3.92$ μm. When we insert this value into equation (4.2), we expect a lifetime of ∼97 ms. This short lifetime may explain the absence of nanobubbles on top of the graphene during our experiments.

Water can more easily intercalate between graphene and mica than between the layers of graphene due to the lower adhesion energies between the two

materials.[40,41] Water intercalation in HOPG has been investigated previously.[42,43] The authors applied a positive potential to HOPG which resulted in the nucleation of oxygen blisters. However, in Figure 4.3(c(V)) we see a strong signal that the nanobubbles grow between graphene and mica. From a sequence of optical images after the image in Figure 4.3(c(V)) we see that the entire graphene blanket moved up and down after delamination. This motion gave strong evidence that the nanobubbles nucleate between graphene and mica and not between the graphene layers.

To calculate the pressure difference Δp of the nanobubble compared to the environment, Hencky's solution is used:[44,45]

$$\Delta p = \frac{K(\nu) E t h^3}{r^4}, \tag{4.3}$$

where K is a coefficient depending on ν, the Poisson's ratio of graphene, E is the Young's modulus of graphene, t is the thickness of the graphene blanket (a monolayer graphene is 0.335 nm high), h is the height of the nanobubble and r is the footprint radius of the nanobubble. Equation (4.3) considers a geometrically nonlinear response of the isotropic elastic membrane subjected to a pressure difference across the membrane. For graphene $\nu = 0.16$, $K(\nu = 0.16) = 3.09$ and $E = 1$ TPa.[2,46–48] For the nanobubbles shown in Figures 4.4(c(III)) and 4.4(c(IV)), we get pressures of 1.58 MPa and 8.18 MPa inside the nanobubble, respectively, by applying equation (4.3).

Electrochemically we can vary the size and thus the pressure of the nanobubbles, as we have shown in Figure 4.4(c). An AFM image of nanobubbles on another sample was obtained after applying a current of -1 μA for 13 minutes (voltage was -1.55 V), as shown in Figure 4.6(a). However, the nucleation of these nanobubbles was not captured. The thickness of the graphene blanket was measured by AFM to be 4 - 6 layers. The heights of the top, middle and bottom nanobubble are 11.5 nm, 11.4 nm and 7.5 nm, respectively. The average footprint radii are 345 nm, 313 nm and 315 nm, respectively. The matching pressures can be calculated by applying equation (4.3), resulting in 0.65 MPa, 0.90 MPa and 0.32 MPa, respectively. Small differences in size and shape are probably related to differences in the local geometry of the graphene blanket. After 35 minutes at a current of -1 μA, the size of the top nanobubble has reached equilibrium, as shown in Figure 4.6(b). Its average radius is 593 nm and its height is 15.6 nm.

The nanobubbles prefer to grow under a thin graphene blanket. We see that nanobubbles nucleate in areas both above and below the thicker

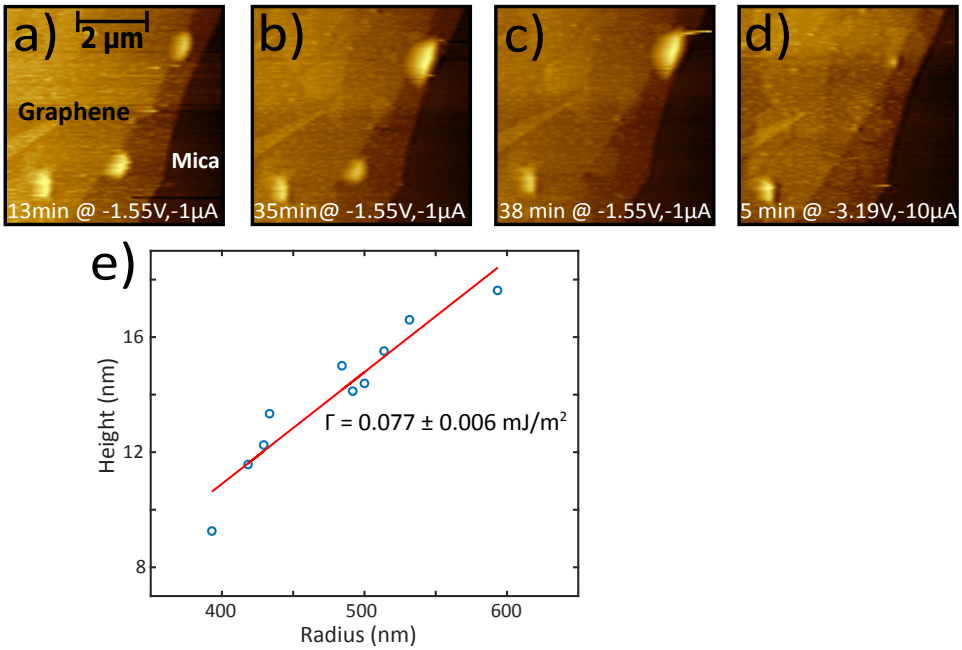

Figure 4.6: (a) Three nanobubbles during electrolysis viewed under AFM. (b) The size of the top nanobubble increased over time. (c) The nanobubble in the middle disappeared. (d) The current was increased, which also resulted in the disappearance of the top nanobubble. (e) Height as function of the radius of the top nanobubble of figure (a-c). The radius and height have a linear relation, as described in the text.

graphene area, marked by the number 5 in Figure 4.2(c). If the graphene blanket is too thick, in for example a flake of HOPG, we do not see nanobubbles since HOPG is hardly bent by the nanobubbles. In Figure 4.4(c(I)), the nanobubble had nucleated at the location of a defect, as showed by the graphene ripple. In Figure 4.6(a), two of the three nanobubbles have nucleated at a B-type step edge. At a B-type step edge, a larger amount of water is available to promote ion transport compared to places without a B-type step edge. We do not have good statistics to draw conclusions about whether nanobubbles prefer to nucleate at a B-type step edge or at the location of a defect. The location where nanobubbles nucleate sheds more light on the delamination process during the bubbling transfer method, typically used in the transfer of large graphene sheets.[49–51] In this method graphene is removed from a substrate (for example copper), by immersing the system in water and applying a potential to the substrate. The formation of hydrogen gas detaches the graphene from the substrate. That bubbles grow at defects and B-type step edges can be considered when further improving the bubbling transfer method. The effect of the number of graphene layers on shape of the nanobubbles was not investigated. The quantity of nanobubbles we observed by AFM was not high enough to extract good statistics and the exact number of graphene layers is hard to exactly determine in few layer graphene areas.

Delamination starts when the pressure inside the nanobubble overcomes the adhesion energy between graphene and mica, intercalated with water. After 38 minutes at a current of -1 μA, the nanobubble in the middle disappeared, as shown in Figure 4.6(c). Due to the high pressure inside the nanobubble, the graphene delaminated towards its edge and the gas directly dissolved into the bulk water. Note that delamination is an irreversible process. Once the graphene delaminates, no new nanobubbles can be created in this area. The nanobubbles are not exclusively in contact with the thin water film between graphene and mica anymore, but also with the bulk water. By increasing the current to -10 μA (voltage was -3.19 V), the size of the top nanobubble increased further and also eventually disappeared due to delamination of the graphene, as shown in Figure 4.6(d). Rupture of the graphene itself is unlikely since it is expected that graphene prefers delamination due to a low graphene-mica adhesion energy, as will be shown in the next paragraph. Furthermore, graphene is flexible and strong.[2,4] The difference in the time till delamination between the nanobubbles might be related to a

difference in local geometry of the graphene blanket. Also the distance away from a B-type step edge might influence the stability of the nanobubble. The long lifetime of the bottom nanobubble might be related to the absence of a B-type step edges in its vicinity. At this location there might have been a defect which fostered the nucleation of this nanobubble. One can also see that the intercalated water layers move between Figure 4.6(c) and Figure 4.6(d). Chapter 5 will elaborate in detail on the movement of these water layers between graphene and mica. So we can change the size and pressure of nanobubbles by applying electrochemistry, but control over the exact size and pressure is still limited.

To better understand why the graphene easily delaminates, we look at the adhesion energy Γ between graphene and mica. This adhesion energy can be calculated by using the following equation:[52,53]

$$\Gamma = \frac{Et}{16}\left(\frac{h}{r}\right)^4. \tag{4.4}$$

This equation points out a linear relation between the height of the nanobubble and its radius when the other parameters remain constant. To experimentally obtain the adhesion energy between graphene and mica, the radius of the top nanobubble in Figure 4.6(a-c) is plotted as a function of the height in Figure 4.6(e). A thickness t of 5 layers graphene is taken. By fitting and using equation (4.4), we get a value for the adhesion energy of 0.077 ± 0.006 mJ/m^2. This value is lower than the theoretically predicted value of 1.79 mJ/m^2 between monolayer graphene and mica.[41] The latter amounts to 29.3 meV per carbon atom, where 3.82×10^{17} m^{-2} is taken as the atom density of graphene.[54] The lower adhesion energy we get is probably the result of the multilayer nature of the graphene we use. Also the intercalated water between graphene and mica, which increases the graphene-mica distance, might reduce the adhesion energy.

To explore the time response, we studied the growth and dissolution times of the nanobubbles using optical microscopy. In Figure 4.7(a), the sample — immersed in water and before electrolysis — is shown. The purple encircled black dots are due to impurities on the CCD camera. The graphene had already delaminated a little since a current of -1 μA (voltage was -2.28 V) and -1.17μA (voltage was -2.5 V) were applied before this image was captured. The application of these currents resulted in the nucleation of small nanobubbles. One of these locations is indicated by the blue arrow. This

observation can be explained by a not fully reversible deformation of the graphene blanket during growth and dissolution of the nanobubbles. Here the graphene layers are believed to slide over one another under the influence of the exerted pressure. These nanobubbles at -1 μA and -1.17μA were observed to nucleate at higher currents than during the experiments by AFM in Figure 4.4. Also here the nanobubbles are expected to nucleate around -100 nA and a voltage of -0.88 V, but the nanobubbles were simply too small to be observed under an optical microscope. Larger nanobubbles, which are indicated by arrows, nucleated under the graphene blanket when at t = 0 a voltage of -2.75 V was applied, as shown in Figure 4.7(b) and 4.7(d). At the left axis in Figure 4.7(d), the increase in area of four individual nanobubbles is plotted versus time. The colored curves match to nanobubbles as pointed out by the arrows of the matching color in Figure 4.7(b). After about 5 seconds, the nanobubbles reached dynamic equilibrium and did not grow any further. This equilibrium is established more rapidly than for the nanobubbles viewed by AFM, which is probably related to the higher electrochemical current. At this voltage, the current started to deviate around -1.3 μA, which is shown at the right axis of Figure 4.7(d), matching the black line. This small change in current is assumed to originate from a change in geometry of the graphene blanket when nanobubbles nucleate. Note that the small change in area during electrolysis correlates to the small change in current when the voltage is switched to a constant value. This confirms that the size of the nanobubbles is directly dependent on the electrochemical current. After about 65 seconds, the voltage was switched off and the evolution of hydrogen gas stopped. Within about 10 seconds, the hydrogen gas in the nanobubbles completely dissolved into the thin water film[†].

By using the diffusion equation

$$\left\langle x^2 \right\rangle = 4Dt, \tag{4.5}$$

where $\langle x^2 \rangle$ is the mean squared displacement, we estimate a 2D hydrogen diffusion constant of the order of 10^{-14} m^2/s. This value is markedly lower than the 3D diffusion coefficient of hydrogen. The lower value is probably related to the confined nature of the intercalated thin water film. The water will be ordered and reduces the lateral mobility of the hydrogen. We estimate that the water thickness is around 1 nm, which is within the range where

[†]A video of this measurement can be found at
https://pubs.acs.org/doi/suppl/10.1021/acs.langmuir.6b00777

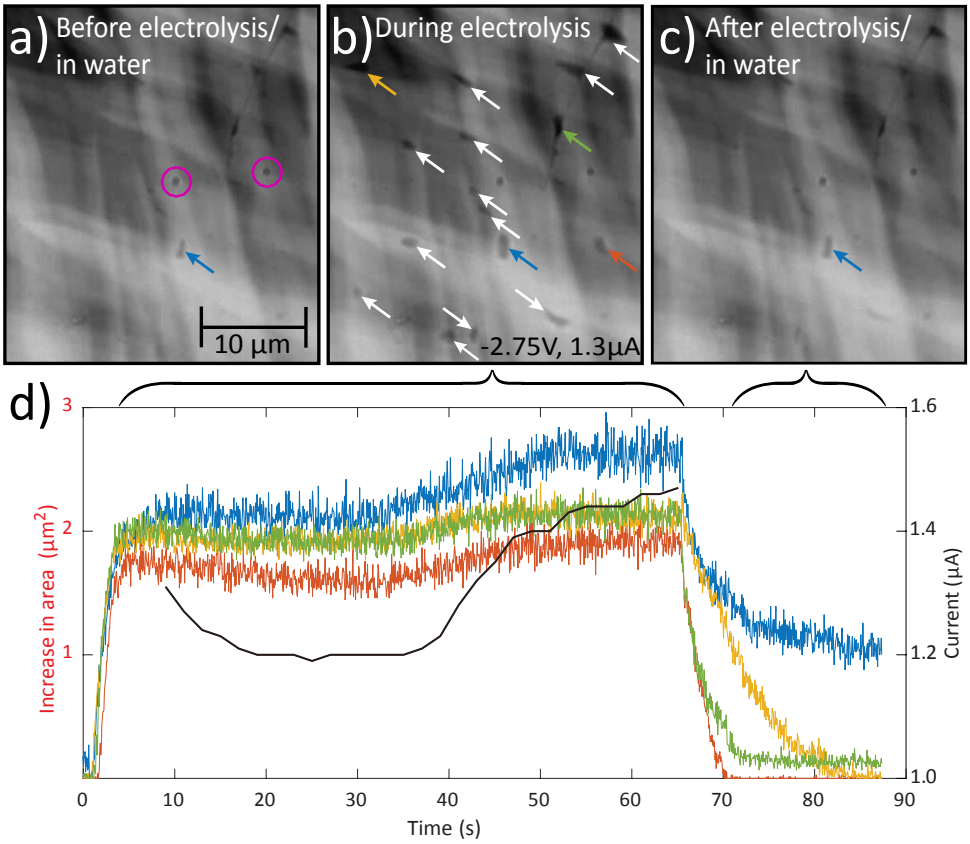

Figure 4.7: (a) Optical microscopy images of the sample before electrolysis. The purple encircled black dots mark impurities on the CCD camera. The blue arrow points out a delaminated part of the graphene blanket. (b) Sample during electrolysis. The nanobubbles are indicated by the arrows. (c) Sample after electrolysis. (d) Plot of the increase in area of the nanobubbles versus time, with the matching electrochemical current (solid black line).

van der Waals forces between graphene and mica are still significant.[16] Due to local geometry differences in the graphene blanket, the dissolution times slightly varied between different nanobubbles. Note that not all nanobubbles returned to their original shape, as shown for example by the nanobubble pointed out by the blue arrow in Figure 4.7(c). The dissolution time of the nanobubbles under the graphene blanket is in the range of 5 to 15 seconds, which is significantly longer than the dissolution time expected for unpinned nanobubbles on top of the graphene blanket. In that case, lifetimes are in the millisecond range, as predicted by equation (4.2).

4.4 Conclusions

We have shown that we can nucleate *dynamic* hydrogen nanobubbles between graphene and mica by use of electrochemistry. Optical microscopy and AFM images strongly suggest that the nanobubbles grow underneath the graphene blanket. From optical microscopy images, it became obvious that the nanobubbles nucleated between graphene and mica, but not between the graphene layers. The pressure inside the nanobubbles is found to be in the MPa range. At higher electrochemical currents the nanobubbles reach dynamic equilibrium within a few seconds and dissolve in tens of seconds. Although we can vary the size and pressure of the nanobubbles by varying the current or voltage, we cannot control their exact size or pressure. Also the exact locations at which nanobubbles nucleate cannot be predicted beforehand. To conclude, we showed the first steps of control over nanobubbles between graphene and mica. A suggestion for further research would be to aim for more control over these nanobubbles.

Bibliography

[1] Geim, A. K. Graphene: Status and Prospects. *Science* **2009**, *324*, 1530–1534.

[2] Lee, C.; Wei, X.; Kysar, J. W.; Hone, J. Measurement of the Elastic Properties and Intrinsic Strength of Monolayer Graphene. *Science* **2008**, *321*, 385–388.

[3] Novoselov, K. S.; Geim, A. K.; Morozov, S. V.; Jiang, D.; Katsnelson, M. I.; Grigorieva, I. V.; Dubonos, S. V.; Firsov, A. A. Two-

Dimensional Gas of Massless Dirac Fermions in Graphene. *Nature* **2005**, *438*, 197–200.

[4] Bunch, J. S.; Verbridge, S. S.; Alden, J. S.; van der Zande, A. M.; Parpia, J. M.; Craighead, H. G.; McEuen, P. L. Impermeable Atomic Membranes from Graphene Sheets. *Nano Lett.* **2008**, *8*, 2458–2462.

[5] Levy, N.; Burke, S. A.; Meaker, K. L.; Panlasigui, M.; Zettl, A.; Guinea, F.; Neto, A. H. C.; Crommie, M. F. Strain-Induced Pseudo–Magnetic Fields Greater Than 300 Tesla in Graphene Nanobubbles. *Science* **2010**, *329*, 544–547.

[6] Lim, C. H. Y. X.; Nesladek, M.; Loh, K. P. Observing High-Pressure Chemistry in Graphene Bubbles. *Angew. Chem., Int. Edit.* **2014**, *53*, 215–219.

[7] Lim, C. H. Y. X.; Sorkin, A.; Bao, Q.; Li, A.; Zhang, K.; Nesladek, M.; Loh, K. P. A Hydrothermal Anvil Made of Graphene Nanobubbles on Diamond. *Nat. Commun.* **2013**, *4*, 1556.

[8] Stolyarova, E. et al. Observation of Graphene Bubbles and Effective Mass Transport under Graphene Films. *Nano Lett.* **2009**, *9*, 332–337.

[9] Zamborlini, G.; Imam, M.; Patera, L. L.; Menteş, T. O.; Stojić, N.; Africh, C.; Sala, A.; Binggeli, N.; Comelli, G.; Locatelli, A. Nanobubbles at GPa Pressure under Graphene. *Nano Lett.* **2015**, *15*, 6162–6169.

[10] Georgiou, T.; Britnell, L.; Blake, P.; Gorbachev, R. V.; Gholinia, A.; Geim, A. K.; Casiraghi, C.; Novoselov, K. S. Graphene Bubbles with Controllable Curvature. *Appl. Phys. Lett.* **2011**, *99*, 093103.

[11] Lee, J. H.; Tan, J. Y.; Toh, C.-T.; Koenig, S. P.; Fedorov, V. E.; Castro Neto, A. H.; Özyilmaz, B. Nanometer Thick Elastic Graphene Engine. *Nano Lett.* **2014**, *14*, 2677–2680.

[12] Smith, A. D.; Niklaus, F.; Paussa, A.; Vaziri, S.; Fischer, A. C.; Sterner, M.; Forsberg, F.; Delin, A.; Esseni, D.; Palestri, P.; Östling, M.; Lemme, M. C. Electromechanical Piezoresistive Sensing in Suspended Graphene Membranes. *Nano Lett.* **2013**, *13*, 3237–3242.

[13] Severin, N.; Lange, P.; Sokolov, I. M.; Rabe, J. P. Reversible Dewetting of a Molecularly Thin Fluid Water Film in a Soft Graphene Mica Slit Pore. *Nano Lett.* **2012**, *12*, 774–779.

[14] Bampoulis, P.; Siekman, M. H.; Kooij, E. S.; Lohse, D.; Zandvliet, H. J. W.; Poelsema, B. Latent Heat Induced Rotation Limited Aggregation in 2D Ice Nanocrystals. *J. Chem. Phys.* **2015**, *143*, 034702.

[15] Kim, J.-S.; Choi, J. S.; Lee, M. J.; Park, B. H.; Bukhvalov, D.; Son, Y.-W.; Yoon, D.; Cheong, H.; Yun, J.-N.; Jung, Y.; Salmeron, M. Between Scylla and Charybdis: Hydrophobic Graphene-guided Water Diffusion on Hydrophilic Substrates. *Sci. Rep.* **2013**, *3*, 2309.

[16] Song, J.; Li, Q.; Wang, X.; Li, J.; Zhang, S.; Kjems, J.; Besenbacher, F.; Dong, M. Evidence of Stranski–Krastanov Growth at the Initial Stage of Atmospheric Water Condensation. *Nat. Commun.* **2014**, *5*, 4837.

[17] Lee, M.; Choi, J.; Kim, J.-S.; Byun, I.-S.; Lee, D.; Ryu, S.; Lee, C.; Park, B. Characteristics and Effects of Diffused Water Between Graphene and a SiO_2 Substrate. *Nano Res.* **2012**, *5*, 710–717.

[18] Lui, C. H.; Liu, L.; Mak, K. F.; Flynn, G. W.; Heinz, T. F. Ultraflat Graphene. *Nature* **2009**, *462*, 339–341.

[19] Novoselov, K. S.; Geim, A. K.; Morozov, S. V.; Jiang, D.; Zhang, Y.; Dubonos, S. V.; Grigorieva, I. V.; Firsov, A. A. Electric Field Effect in Atomically Thin Carbon Films. *Science* **2004**, *306*, 666–669.

[20] Novoselov, K. S.; Jiang, D.; Schedin, F.; Booth, T. J.; Khotkevich, V. V.; Morozov, S. V.; Geim, A. K. Two-Dimensional Atomic Crystals. *P. Nat. Acad. Sci. U. S. A.* **2005**, *102*, 10451–10453.

[21] Rezania, B.; Dorn, M.; Severin, N.; Rabe, J. Influence of Graphene Exfoliation on the Properties of Water-containing Adlayers Visualized by Graphenes and Scanning Force Microscopy. *J. Colloid Interface Sci.* **2013**, *407*, 500–504.

[22] Nair, R. R.; Blake, P.; Grigorenko, A. N.; Novoselov, K. S.; Booth, T. J.; Stauber, T.; Peres, N. M. R.; Geim, A. K. Fine Structure Constant Defines Visual Transparency of Graphene. *Science* **2008**, *320*, 1308.

[23] Dorn, M.; Lange, P.; Chekushin, A.; Severin, N.; Rabe, J. P. High Contrast Optical Detection of Single Graphenes on Optically Transparent Substrates. *J. Appl. Phys.* **2010**, *108*, 106101.

[24] Berkelaar, R. P.; Dietrich, E.; Kip, G. A. M.; Kooij, E. S.; Zandvliet, H. J. W.; Lohse, D. Exposing Nanobubble-like Objects to a Degassed Environment. *Soft Matter* **2014**, *10*, 4947–4955.

[25] Matsumoto, Y.; Tateishi, H.; Koinuma, M.; Kamei, Y.; Ogata, C.; Gezuhara, K.; Hatakeyama, K.; Hayami, S.; Taniguchi, T.; Funatsu, A. Electrolytic Graphene Oxide and its Electrochemical Properties. *J. Electroanal. Chem.* **2013**, *704*, 233–241.

[26] Xu, K.; Cao, P.; Heath, J. R. Graphene Visualizes the First Water Adlayers on Mica at Ambient Conditions. *Science* **2010**, *329*, 1188–1191.

[27] Bampoulis, P.; Lohse, D.; Zandvliet, H. J. W.; Poelsema, B. Coarsening Dynamics of Ice Crystals Intercalated Between Graphene and Supporting Mica. *Appl. Phys. Lett.* **2016**, *108*, 011601.

[28] Duan, W. H.; Wang, C. M. Nonlinear Bending and Stretching of a Circular Graphene Sheet under a Central Point Load. *Nanotechnology* **2009**, *20*, 075702.

[29] Gil, A. J.; Adhikari, S.; Scarpa, F.; Bonet, J. The Formation of Wrinkles in Single-Layer Graphene Sheets under Nanoindentation. *J. Phys.: Condens. Matter* **2010**, *22*, 145302.

[30] Bar, G.; Thomann, Y.; Brandsch, R.; Cantow, H.-J.; Whangbo, M.-H. Factors Affecting the Height and Phase Images in Tapping Mode Atomic Force Microscopy. Study of Phase-Separated Polymer Blends of Poly(ethene-co-styrene) and Poly(2,6-dimethyl-1,4-phenylene oxide). *Langmuir* **1997**, *13*, 3807–3812.

[31] Ando, T.; Uchihashi, T.; Fukuma, T. High-speed Atomic Force Microscopy for Nano-visualization of Dynamic Biomolecular Processes. *Prog. Surf. Sci.* **2008**, *83*, 337–437.

[32] Zhang, L.; Zhang, Y.; Zhang, X.; Li, Z.; Shen, G.; Ye, M.; Fan, C.; Fang, H.; Hu, J. Electrochemically Controlled Formation and Growth of Hydrogen Nanobubbles. *Langmuir* **2006**, *22*, 8109–8113.

[33] Yang, S.; Tsai, P.; Kooij, E. S.; Prosperetti, A.; Zandvliet, H. J. W.; Lohse, D. Electrolytically Generated Nanobubbles on Highly Orientated Pyrolytic Graphite Surfaces. *Langmuir* **2009**, *25*, 1466–1474.

[34] Yang, S.; Tsai, P.; Kooij, E. S.; Prosperetti, A.; Zandvliet, H. J. W.; Lohse, D. Correction to Electrolytically Generated Nanobubbles on Highly Orientated Pyrolytic Graphite Surfaces. *Langmuir* **2013**, *29*, 5937–5937.

[35] Zhang, X.; Chan, D. Y. C.; Wang, D.; Maeda, N. Stability of Interfacial Nanobubbles. *Langmuir* **2013**, *29*, 1017–1023.

[36] Lohse, D.; Zhang, X. Pinning and Gas Oversaturation Imply Stable Single Surface Nanobubbles. *Phys. Rev. E* **2015**, *91*, 031003.

[37] Epstein, P. S.; Plesset, M. S. On the Stability of Gas Bubbles in Liquid-Gas Solutions. *J. Chem. Phys.* **1950**, *18*, 1505–1509.

[38] Ljunggren, S.; Eriksson, J. C. The Lifetime of a Colloid-sized Gas Bubble in Water and the Cause of the Hydrophobic Attraction. *Colloids Surf., A* **1997**, *129–130*, 151–155.

[39] Lohse, D.; Zhang, X. Surface Nanobubbles and Nanodroplets. *Rev. Mod. Phys.* **2015**, *87*, 981–1035.

[40] Loeb, G. I.; Schrader, M. E. *Modern Approaches to Wettability: Theory and Applications*; Springer Science & Business Media, 2013.

[41] Rudenko, A. N.; Keil, F. J.; Katsnelson, M. I.; Lichtenstein, A. I. Graphene Adhesion on Mica: Role of Surface Morphology. *Phys. Rev. B: Condens. Matter Mater. Phys.* **2011**, *83*, 045409.

[42] Goss, C. A.; Brumfield, J. C.; Irene, E. A.; Murray, R. W. Imaging the Incipient Electrochemical Oxidation of Highly Oriented Pyrolytic Graphite. *Anal. Chem.* **1993**, *65*, 1378–1389.

[43] Hathcock, K. W.; Brumfield, J. C.; Goss, C. A.; Irene, E. A.; Murray, R. W. Incipient Electrochemical Oxidation of Highly Oriented Pyrolytic Graphite: Correlation between Surface Blistering and Electrolyte Anion Intercalation. *Anal. Chem.* **1995**, *67*, 2201–2206.

[44] Hencky, H. Uber den Spannungszustand in kreisrunden Platten mit verschwindender Biegungssteifigkeit. *Zeitschrift fur Mathematik und Physik* **1915**, *63*, 311–317.

[45] Williams, J. G. Energy Release Rates for the Peeling of Flexible Membranes and the Analysis of Blister Tests. *Int. J. Fracture* **1997**, *87*, 265–288.

[46] Blakslee, O. L.; Proctor, D. G.; Seldin, E. J.; Spence, G. B.; Weng, T. Elastic Constants of Compression-annealed Pyrolytic Graphite. *J. Appl. Phys.* **1970**, *41*, 3373–3382.

[47] Koenig, S. P.; Boddeti, N. G.; Dunn, M. L.; Bunch, J. S. Ultrastrong Adhesion of Graphene Membranes. *Nat. Nanotechnol.* **2011**, *6*, 543–546.

[48] Al-Jishi, R.; Dresselhaus, G. Lattice-Dynamical Model for Graphite. *Phys. Rev. B: Condens. Matter Mater. Phys.* **1982**, *26*, 4514–4522.

[49] Wang, Y.; Zheng, Y.; Xu, X.; Dubuisson, E.; Bao, Q.; Lu, J.; Loh, K. P. Electrochemical Delamination of CVD-Grown Graphene Film: Toward the Recyclable Use of Copper Catalyst. *ACS Nano* **2011**, *5*, 9927–9933.

[50] Gao, L.; Ren, W.; Xu, H.; Jin, L.; Wang, Z.; Ma, T.; Ma, L.-P.; Zhang, Z.; Fu, Q.; Peng, L.-M. Repeated Growth and Bubbling Transfer of Graphene with Millimetre-size Single-crystal Grains Using Platinum. *Nat. Commun.* **2012**, *3*, 699.

[51] de la Rosa, C. J. L.; Sun, J.; Lindvall, N.; Cole, M. T.; Nam, Y.; Löffler, M.; Olsson, E.; Teo, K. B. K.; Yurgens, A. Frame Assisted H_2O Electrolysis Induced H_2 Bubbling Transfer of Large Area Graphene Grown by Chemical Vapor Deposition on Cu. *Appl. Phys. Lett.* **2013**, *102*, 022101.

[52] Zong, Z.; Chen, C.-L.; Dokmeci, M. R.; Wan, K.-T. Direct Measurement of Graphene Adhesion on Silicon Surface by Intercalation of Nanoparticles. *J. Appl. Phys.* **2010**, *107*, 026104.

[53] Wan, K.-T.; Mai, Y.-W. Fracture Mechanics of a Shaft-loaded Blister of Thin Flexible Membrane on Rigid Substrate. *Int. J. Fract.* **1996**, *74*, 181–197.

[54] Pop, E.; Varshney, V.; Roy, A. K. Thermal Properties of Graphene: Fundamentals and Applications. *MRS Bull.* **2012**, *37*, 1273–1281.

5

Charge induced dynamics of water in a graphene-mica slit pore

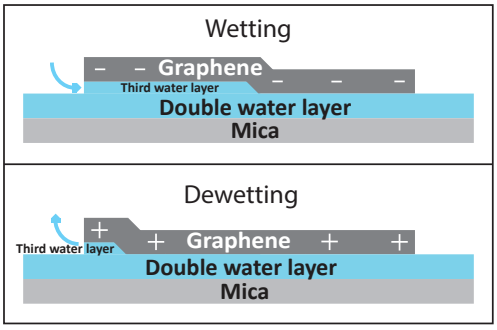

We use atomic force microscopy to *in situ* investigate the dynamic behavior of confined water at the interface between graphene and mica. The graphene is either uncharged, negatively charged or positively charged. At high humidity, a third water layer will intercalate between graphene and mica. When graphene is negatively charged, the interface fills faster with a complete three layer water film, compared to uncharged graphene. As charged positively, the third water layer dewets the interface, either by evaporation into the ambient or by the formation of three-dimensional droplets under the graphene, on top of the bilayer. Our experimental findings reveal novel phenomena of water at the nanoscale, which are interesting from a fundamental point of view and demonstrate the direct control over the wetting properties of the graphene/water interface.

5.1 Introduction

The behavior of *confined* water under the influence of surface charges is of fundamental importance to the emerging field of electrocatalysis under a two-dimensional (2D) cover.[1–3] Due to the confined nature and the large surface area, the orientation of water molecules toward a 2D catalytic surface is essential for efficient electrochemical reactions, e.g. in a nanoreactor. Furthermore, knowledge of confined water at a charged surface is crucial for the control over graphene nanobubbles created by water splitting.[4,5] In our previous work,[4] we showed the formation of hydrogen nanobubbles between graphene and mica created by water splitting. At the location where nanobubbles were formed, an additional water layer was observed as compared to their surroundings. This indicates that the additional water layer promotes graphene nanobubble nucleation. Therefore, improving water intercalation in these systems can enhance the graphene nanobubble formation. Finally, the study of confined water at a charged surface is relevant to the field of electrowetting. So far, electrowetting has mainly been investigated experimentally at the macroscale. In this paper, we experimentally demonstrate new wetting behavior at the nanoscale for the first time. To investigate confined water at a charged surface, we employed water confined in a graphene-mica slit pore.

Graphene is a 2D conductive material which consists of carbon atoms arranged in a honeycomb structure. Graphene's atomic thickness, hydrophobicity, and flexibility[6] makes it an ideal cover to study confined water layers at the molecular level with atomic force microscopy (AFM).[7] A graphene cover prohibits direct contact of the AFM tip with the water molecules, avoiding unwanted interactions. Mica is a mineral, atomically flat,[8] and, in contrast to graphene, hydrophilic and insulating. The flatness of the mica makes it an ideal substrate to study confined water since changes in height can easily be observed with AFM.

In our *experimental* study we investigated *in situ* a graphene-mica slit pore under high (70-96%) relative humidities (RHs) for graphene that is either uncharged, positively charged, or negatively charged. Distinct behavior is observed in all three situations, demonstrating the role of graphene in defining the behavior of the water molecules. Our approach paves the way toward experimental studies of the dynamics of water at the molecular level under confinement and at charged surfaces.

5.2 Experimental section

The mechanical exfoliation method was used to prepare graphene on mica.[9–11] A 2.5x2.5 cm^2 piece of muscovite mica (SPI, V1) was cleaved with a clean scalpel, resulting in a fresh and clean surface. The thickness of the cleaved mica piece was $\sim$40 μm. Graphene was obtained from highly oriented pyrolytic graphite (HOPG, grade ZYB, MikroMasch). The HOPG sample was cleaved with Scotch tape. After cleaving, one of the small loose standing HOPG flakes was peeled off from the HOPG sample with a clean tweezer. Then the flake was pressed with its fresh and clean side onto the mica surface under ambient conditions. Depositing the HOPG flake on the mica was done without using Scotch tape since it easily contaminates the surface.[12] One side of the HOPG flake was not pressed onto the mica surface so that the flake could be peeled off again. After peeling off the flake, some residual HOPG remained attached to the mica. This residual HOPG is referred to as a graphene blanket. The thickness of the blanket varied from monolayer graphene to multilayer graphene. The thickness of the HOPG was initially identified with optical reflection microscopy,[13,14] where the light source and microscope objective were both located above the sample.[15] Our optical microscope (Leica DM2500 MH) was used in combination with HI PLAN EPI 5x/0.12, N PLAN L 20x/0.40, and N PLAN L 50x/0.50 objectives and a PCO PixelFly CCD camera. After identifying an area with a few layers of graphene, AFM was used to find monolayer graphene within this area.

Figure 5.1 shows a photo of the AFM sample plate. To make an electrical connection to the graphene, a few small HOPG flakes were deposited in an overlapping fashion from the edge of the graphene blanket (which is connected to the graphene) toward the edge of the mica piece. The sample is then placed on a 2.5x2.5 cm^2 aluminum plate, which functioned as the counter electrode. The aluminum plate-sample stack is held steady on an AFM sample plate by clamping it with two spring steel clamps. One of these clamps is pressed on top of the overlapping HOPG flakes at the edge of the mica to establish an electrical connection to the graphene.

The sample was then placed in an environmental chamber. The relative humidity (RH) was increased by flowing high humidity gas through the chamber. The high humidity gas consisted of dry nitrogen which was purged through three connected gas washing bottles with Milli-Q water (18.2 MΩ·cm). The dry nitrogen flow was measured with a flow meter (King In-

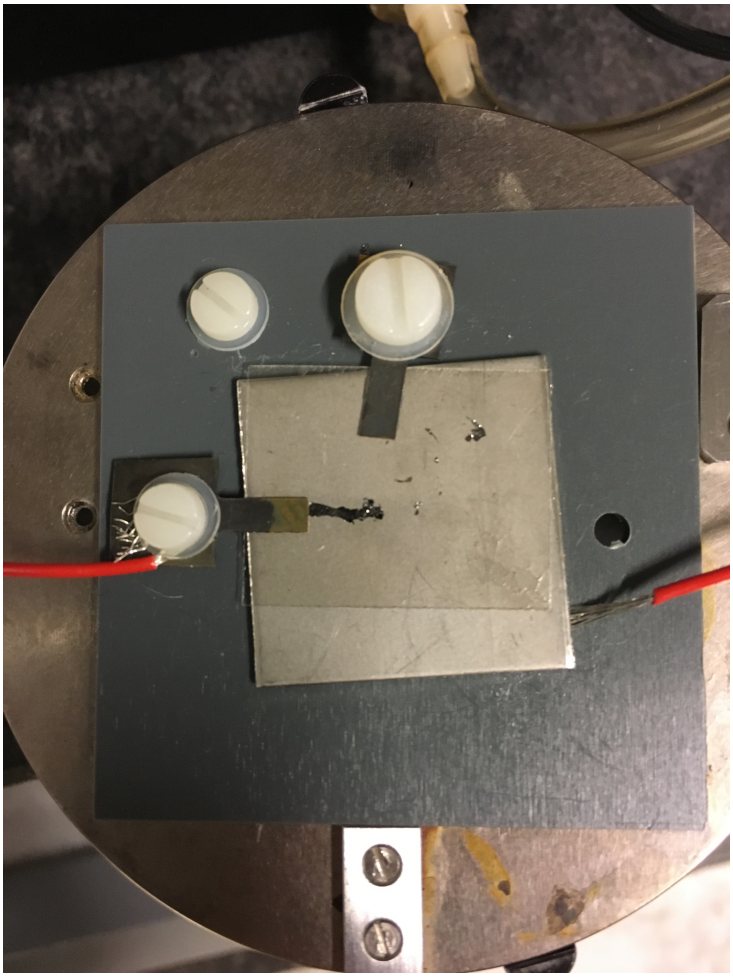

Figure 5.1: Photo of the AFM sample plate.

strument Co., model 7530) and was kept at a constant flow rate throughout the experiments. The flow rate was 0.50±0.05 L/min. A higher flow rate resulted in too many vibrations in the system. The relative humidity was measured with a humidity sensor (Sensirion SHT75) positioned at the bottom of the environmental chamber. The potential, which induces a charge, was applied to the graphene using a power supply (Delta Elektronika Power Supply, E030-1). During the negatively charged graphene experiment, the negative electrode of the power supply was connected to the spring steel clamp and the positive electrode was connected to the aluminum counter electrode. During the positively charged graphene experiment, the electrodes were reversed. A multimeter (ISO-TECH, IDM 106N) was used to accurately determine the applied voltage. It is important that the graphene was grounded during all experiments. Scanning while the graphene was not grounded resulted in damage to the graphene. Furthermore, all experiments were performed at room temperature.

An Agilent 5100 AFM using intermittent contact mode in the constant amplitude mode was used. We have used an AFM scanning setpoint which is at 90% of the free oscillation amplitude. At this setpoint, we tap the surface with very low force. In this way we interact weakly with water layers on top of surfaces, which enables us to image them. As AFM tip we used a MikroMasch HQ:NSC35/CR-AU BS cantilever B (with a nominal spring constant of 16 N/m and a resonance frequency of 300 kHz).

For the calculation of the area of the intercalated water layers, we imported the AFM images to the computer program Fiji. In this program we cropped the image in such a way that only the area of interest, where the third water layer grows, is encapsulated. We then applied a threshold filter to make the image binary. The threshold is chosen so that only the third water layer is converted to black pixels. The analyze particles function is then applied to count the number of black pixels in every frame. This number is then multiplied with the right scale factor to obtain the area.

5.3 Results

5.3.1 Ambient conditions

Under ambient conditions, a water film is always present between graphene and mica.[7,11,16–19] The film has been shown to consist of two water layers.[20,21]

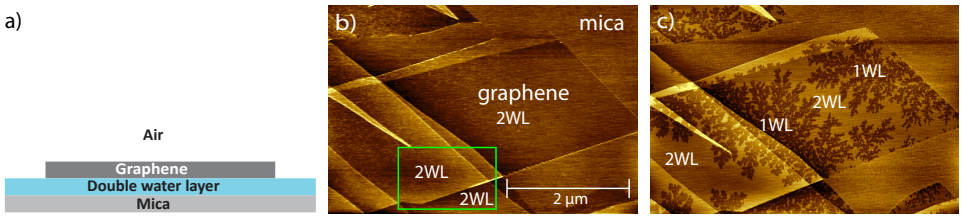

Figure 5.2: (a) Schematic illustration of the sample under ambient conditions. (b) AFM image of a graphene blanket on mica under ambient conditions (RH = 41%). (**c**) AFM image under low humidity conditions (RH = 0.1%).

A schematic illustration of the sample under ambient conditions is depicted in Figure 5.2(a). Note that the schematic illustration is not to scale. Figure 5.2(b) shows an AFM image taken under ambient conditions (RH = 41%). In the center of Figure 5.2(b) a monolayer graphene flake is located. The graphene flake is surrounded by mica. At the left and top, the graphene flake is connected to multilayer graphene. The number of water layers (WL) under the graphene is also indicated. The graphene has a darker contrast compared to the mica. We ascribe this to operating the AFM in a mixed attractive-repulsive mode during this scan.[22] On the mica, the AFM tip is in a repulsive mode and on the graphene the AFM tip is in an attractive mode. This causes an incorrect visualization of the height of the graphene compared to the mica.

When the RH is reduced to ∼1%, 2D ice crystals grow under the graphene cover, induced by the heat extracted from the system by the evaporation of water molecules from the interface;[20] see Figure 5.2(c). The water molecules in the ice crystals form a H-down network with the oxygen side of the water molecules pointing toward the graphene. This results in a net dipole moment.[20] As a result, the graphene becomes positively charged and thus p-type doped.[20]

5.3.2 High humidity, no external stimulus

We now increase the relative humidity of the AFM environmental chamber. The RH reaches the maximum achievable value of 83% (we note that the maximum achievable RH varied from 83 to 96% between experiments since the flow rate and gas washing bottle configuration were slightly different).

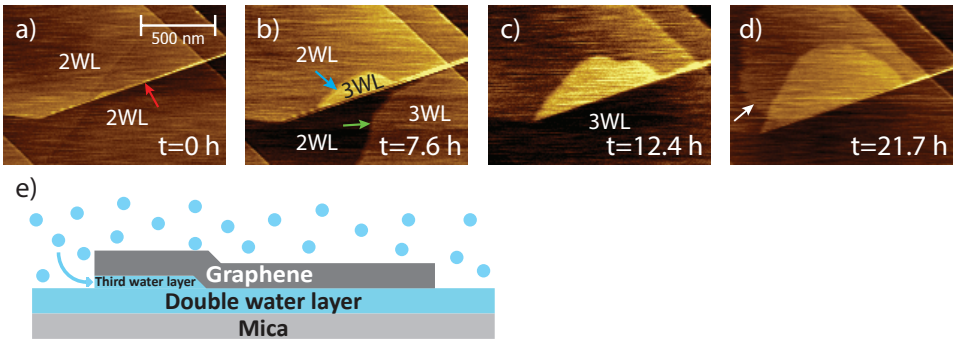

Figure 5.3: (a-d) Sample at high humidity, RH = 83%. After 12.7 h a third water layer formed. (e) Schematic illustration of the sample under high humidity conditions.

At 83% RH, a third water layer starts to form between graphene and mica, indicating intercalation of water molecules into the system due to capillary forces.[23–30] In this experiment, the third water layer started to form after 12.7 h at 83% RH, at the location of the green rectangle in Figure 5.2(b). The formation of the third water layer is depicted in Figures 5.3(a-d). In Figure 5.3(b) the third water layer of interest is indicated by the blue arrow. The time when the third water layer started to form is set at t = 0 h. In Figure 5.3(e) the formation of the third water layer is schematically represented*.

The start of the formation of a third water layer varied from minutes to hours between experiments. The local RH at the sample may be lower than the measured RH at the bottom of the AFM environmental chamber. Only after some time, there may be an equilibrium in RH, resulting in the formation of a third water layer. Differences in graphene geometry between samples may also account for the different starting times.

The measured height of the third water layer is ∼0.37 nm and corresponds well to the interlayer distance of ice-I_h.[31] The water height is calibrated based on the known height of a graphene step edge. We consider the fact that the third water layer has a thickness close to the ice-I_h interlayer distance reflects that the systems keeps its perpendicular order. This stratification effect may

*A movie of the water intercalation due to the high humidity, as shown in Figure 5.3, is provided at https://pubs.acs.org/d oi/suppl/10.1021/acs.langmuir.7b02759

originate from the underlying mica substrate and its interaction with the water molecules.

Since graphene is impermeable to gases,[32] the water molecules can only intercalate from the edges of the graphene. During this experiment, the third water layer initially formed under multilayer graphene. It grew from a bottom graphene step edge, a so-called B-type step edge.[11] At a B-type step edge, a bottom layer of graphene ends, resulting in the graphene layer above it to partly follow the topography of the bottom graphene layer and to partly follow the topography of the mica. The curvature of the graphene at a B-type step edge results in a small channel in which water can flow. One of the B-type step edges in Figure 5.3(a) is indicated by the red arrow. The formation of the third water layer is often bounded by these B-type step edges. In other experiments, we also observed that the third water layer formed first under monolayer graphene. The local geometry of the graphene most likely plays a significant role in the location where the third water layer nucleates.

The third water layer always expands radially. This radial expansion is in strong contrast to the growth of fractal-like 2D ice crystals observed at low humidity and suggests that the water molecules in the third water layer are liquid-like.[25] In Figure 5.3(b) one can also see that, under the graphene cover at the bottom side of the image, a third water layer starts to grow at t = 7.6 h, indicated by the green arrow. The boundaries of the green-arrow-marked third layer of water are the B-type step edges[†]. The growth rate is different compared to the triangle-shaped third water layer indicated by the blue arrow, which is caused by a different geometry of the graphene. In Figure 5.3(d), the three-layer film of interest at the center of the image reached a larger size after 21.7 h. The formation of the third water layer was still going on during this frame. In another experiment, we also observed that the formation of the third water layer can reach a maximum size, partly forming under the graphene cover. In that case, the third water layer reaches a dynamic equilibrium with the three-dimensional (3D) ambient. The intercalation is also bounded by the van der Waals forces between graphene and mica. Most often, the interface completely fills with a water film consisting of three water layers. The formation of a fourth water layer was never observed.[33] The fact that we have never observed a fourth water layer indicates

[†]The water intercalation under high humidity can be seen in a movie at https://pubs.acs.org/doi/suppl/10.1021/acs.langmuir.7b02759

that it is energetically unfavorable. This may be a result of dangling OH bonds on the surface of the third layer, induced by the hydrophobicity of graphene.

Also, a dynamic water layer is discerned in Figure 5.3(d), indicated by the white arrow. The dynamic water layer appears on top of the graphene and shows fuzzy edges. These dynamic water layers are often observed while scanning graphene at high humidity conditions and were predicted by molecular dynamics (MD) simulations[34–36] and observed by previous experimental work.[34,37,38] The area of these dynamic water layers varied significantly between consecutive AFM scans. Upon lowering the humidity, these dynamic water layers disappeared instantly. In the section High Humidity, Negatively Charged Graphene, we will use phase images to show that the dynamic water layer forms on top of the graphene and that the third water layer forms under the graphene. Water layers on graphene are possible since experimental and theoretical studies have shown that freshly cleaved HOPG can be hydrophilic.[36] Its hydrophobicity can be caused by airborne contaminations.[39,40] Graphene also shows a wetting transparency behavior,[41] so the water and mica will also make the graphene less hydrophobic. It has been shown that water can adsorb on HOPG[37] in the form of droplets or layers. In another example, water on graphene/Pt(111) forms a H-bonded network consisting of two flat hexagonal sheets of water molecules in which the hexagons in each sheet are stacked directly on top of each other at low temperatures.[34] This two-layer water structure has closed hydrogen bond. This layer is also experimentally observed.[34,37] The above is also predicted by theory.[35,36] Here, we measured a thickness of the water film on top of the graphene of 1.04 nm. However, since we used tapping mode, the height is not very accurate. We probed a different material (water instead of graphene) which results in different interactions with the AFM tip.

The red graph in Figure 5.4 represents the area of the third water layer indicated by the blue arrow in Figure 5.3 as a function of time. The inset of Figure 5.4 shows a linear growth of the area in the first hours of the scan. The rate of intercalation is 0.005 μm^2/h. This rate is very dependent on the geometry of the graphene flake.[‡]. The number of graphene layers is not observed to have an influence in the water intercalation rate. The middle part of the red line in Figure 5.4 shows an increase in area due to the complete

[‡]The water intercalation movie can be seen at
https://pubs.acs.org/doi/suppl/10.1021/acs.langmuir.7b02759

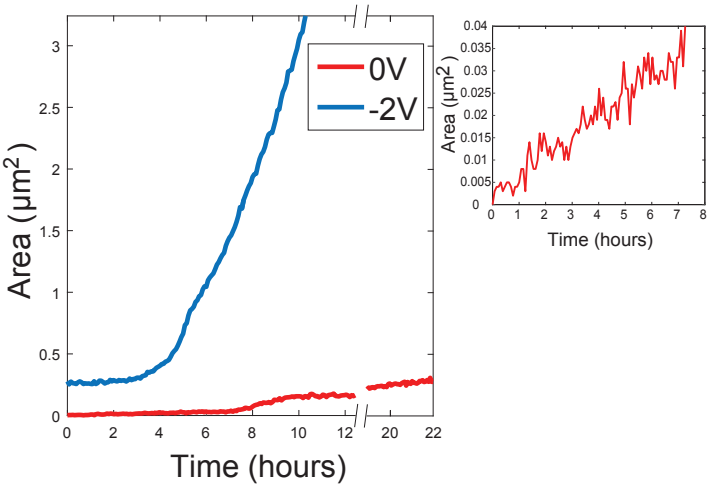

Figure 5.4: Plot of the area of the third water layer versus time. The red line corresponds to the situation without applied voltage to the graphene. The inset shows a linear growth of the area in the first hours of the scan. The blue line corresponds to -2V applied to the graphene.

formation of the third water layer under the graphene cover at the bottom of Figure 5.3(b), which is indicated by the green arrow. Due to vertical drift, we lost AFM tip-sample contact overnight, resulting in some missing data points between 12.4 and 19 h.

5.3.3 High humidity, negatively charged graphene

Figures 5.5(a-d) shows AFM images of the graphene-mica sample in which the graphene is negatively charged. This is achieved by application of a negative voltage bias to the graphene relative to the aluminum counter electrode located under the mica. During the experiment of Figure 5.5, a negative voltage of -2V was applied. The gas flow through the environmental chamber and therewith the RH are kept constant. The AFM scans were performed at the same location as the scans in Figures 5.3(a-d). The formation speed of the third water layer enhanced significantly upon the application of the negative charge to the graphene, as can be seen by the increase in the area of the third water layer over time. In Figure 5.5(b) also the growth of a

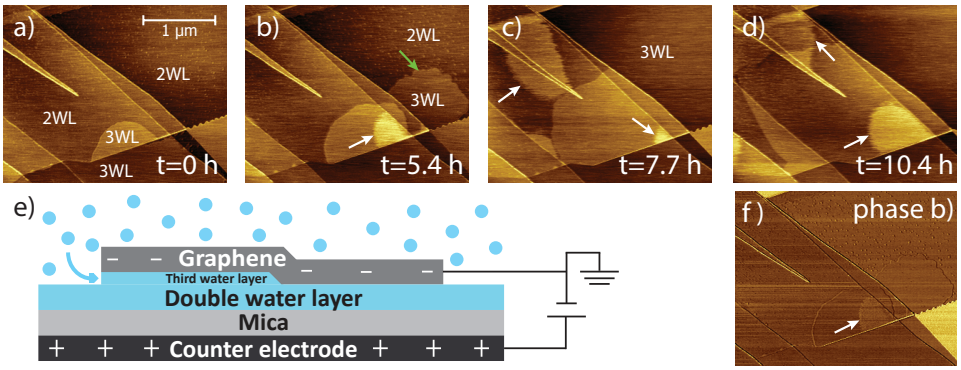

Figure 5.5: Sample at high humidity: (a) RH = 72% and (b-d) RH = 83%. In all images a voltage of -2V is applied to the graphene. (e) Schematic illustration of the sample under high humidity conditions with a negative applied bias to the graphene. (f) Phase image corresponding to topography image (b).

third water layer under the monolayer graphene was observed, indicated by the green arrow. This third water layer intercalation was not observed under high humidity conditions. No onset in the third water layer intercalation was observed under the monolayer graphene, as can be seen in the movie of the experiment[§]. Thus, the negatively charged graphene further promotes the formation of the third water layer under a graphene cover. In Figure 5.5(e) the enhanced water intercalation under negatively charged graphene is schematically represented.

The blue line in Figure 5.4 represents the area increase as a function of time corresponding to the situation where -2V is applied to the graphene. Typically, the initial water intercalation is slow[42] and the area starts to increase exponentially. In this experiment, after 4-5 h, the area of the third water layer starts to increase linearly. The rate of intercalation is 0.5 μm^2/h. It exhibits a significantly higher slope than the red line, revealing the enhanced water intercalation due to the negatively charged graphene. The starting value of the blue line is equal to the final value of the red line since the same region was considered in both experiments. The maximum value

[§]A movie of the enhanced water intercalation due to the negatively charged graphene, as shown in Figure 5.5, is provided at
https://pubs.acs.org/doi/suppl/10.1021/acs.langmuir.7b02759

of this graph is when the third water layer started to grow out of the field of view.

In Figure 5.5(b-d) dynamic water layers on top of the graphene (indicated by white arrows) are again observed. In Figure 5.5(a) the dynamic water layer is absent since we shortly reduced the humidity before we applied -2V to the graphene. In this AFM image, the relative humidity was 72% and had not reached the maximum of 83% RH yet. Figure 5.5(f) shows the phase image corresponding to the topography image in Figure 5.5(b). Using AFM phase imaging, one can probe differences in the elastic response of the surface.[43] We conclude that the dynamic water layers are on top of the graphene since AFM phase images, such as the one in Figure 5.5(f), show a contrast between the area with and without dynamic water layers. No phase difference is observed between the areas with and without a third water layer, indicating that we probe the same type of material, i.e., graphene. Therefore we conclude that the third water layer forms under the graphene cover. A weak contrast is observed between the single-layer of graphene and the few-layer graphene. This is because the single layer graphene is strongly influenced by the underlying substrate and therefore the tip has a different response compared to the few-layer graphene, where the influence fades away.

Formation of the third water layer is a semireversible process. After intercalation of the third water layer, if the RH is reduced to ∼1%, only part of the third water layer evaporates. This evaporation leaves behind two water layers with a fractal-like appearance, indicative of ordering.[20] In Figure 5.6 these fractals are shown. This AFM image was taken when the RH was reduced to 3%, after the experiment at high humidity with negative applied voltage to the graphene. We observed again a mixed attractive-repulsive mode during this AFM scan. The intercalation and evaporation rates are highly dependent on the nitrogen flow rate within the system. During the intercalation experiment, the nitrogen flow rate through the gas washing bottles is restricted to ∼0.5 L/min. Higher flow rates result in too many vibrations in the system due to the bubbling of the water. During the evaporation experiment, the nitrogen flow can be adjusted to higher values before vibrations in the system start to occur. In these higher flow rate experiments, the system reaches equilibrium typically within an hour. This rate is in the same order of magnitude as the rate in which 2D ice fractals form.[11,20] Here we note that the evaporation rate is dependent on the flow rate of the nitrogen, so a direct comparison cannot be made.

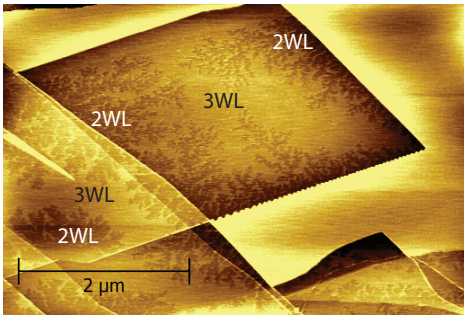

Figure 5.6: Sample at low humidity (RH = 3%), after the experiment at high humidity with negative applied charge to the graphene.

During the experiment with the negatively charged graphene, we first applied -1 V for 3 h. However, no enhancement of the formation of the third water layer was observed. After this, we applied -2 V for 27 h where we saw the enhanced water intercalation. The exact threshold voltage for the start of the growth enhancement of the third water layer has not been determined since the experiment takes a very long time at every voltage. During this experiment, the effect of the magnitude of the voltage is also not determined. At -2V the graphene cover had already a complete formed third water layer underneath it. Since the formation of the third water layer is semi-reversible, we were not able to determine the layer growth at higher voltages under the same graphene cover. To investigate the voltage dependence, one could incrementally increase the voltage during water intercalation.

Figure 5.7(a) shows another graphene on mica sample under ambient conditions. Figure 5.7(b) shows the sample after 22.7 h at 96% RH. The white arrows indicate places where third water layers have significantly formed. In Figure 5.7(c) we apply a negative charge to the graphene. We do this by applying a voltage of -4V to the graphene (which is the first voltage that was applied), keeping the RH constant. We see that the third water layer now also nucleates from multiple locations within the graphene flake. This is a fast process and the first AFM scan we could obtain was 6 minutes after application of the voltage. During another experiment, we also observed the formation of the third water layer from within a graphene cover under high humidity conditions, without applied negative voltage. However, under high humidity

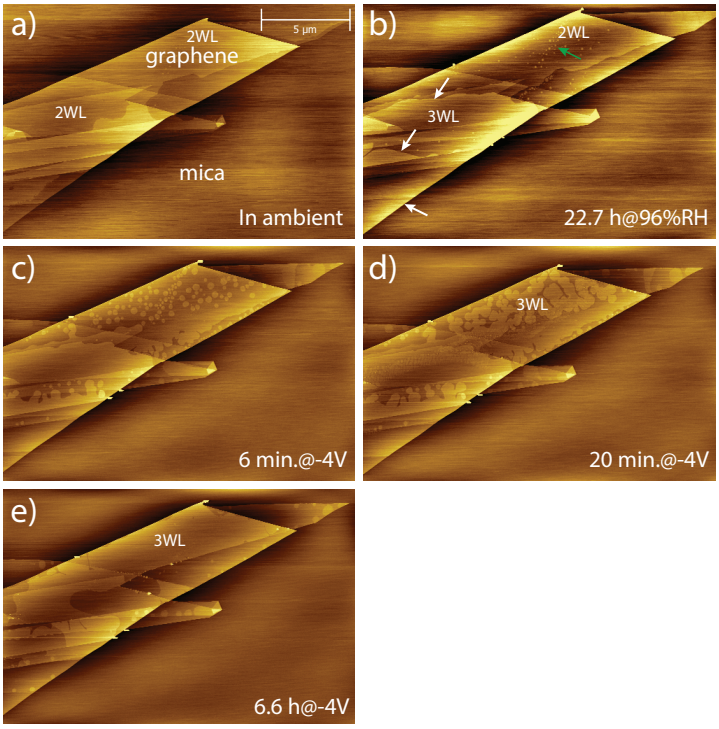

Figure 5.7: AFM images of a graphene on mica sample under (a) ambient conditions, (b) high humidity conditions (RH = 96%), (c-e) high humidity conditions (RH = 96%) with -4V applied to the graphene for 6 minutes, 20 minutes and 6.6 h, respectively.

conditions these formed third water layers were very small (radius of ∼20 nm) and were only observed with a sharp AFM tip (MikroMasch, HI'RES-C14/CR-AU cantilever). Figures 5.7(d-e) show images after 20 minutes and 6.6 h, respectively. After 6.6 h the third water layer has almost completely intercalated under the graphene.

At the locations where the third water layer formed, previously small water droplets were located under the graphene, which acted as nucleation sites, indicated by the green arrow in Figure 5.7(a).[18,25] These water droplets probably nucleated at the location of defects. That nanometer-scale surface defects can serve as nucleation sites for water layers has been observed before

in previous studies[7,18,25,28¶].

5.3.4 High humidity, positively charged graphene

Using a new graphene-mica sample, the influence of a positive applied charge to the graphene is investigated. Figure 5.8(a) shows an AFM image of graphene. In this image, a third water layer has already intercalated due to exposure to a high humidity environment. In this AFM image, only the graphene is visible due to the limited field of view. Figures 5.8(b-f) shows AFM images of the graphene-mica sample when a positive charge is applied to the graphene and keeping the RH constant. The positive charge was achieved by applying +4V to the graphene relative to the aluminum counter electrode. Figure 5.8(b) shows the AFM scan after 29 min at +4V. Surprisingly, we see the formation of a droplet (green arrow) and water evaporating out of the graphene-mica slit pore (white arrow), leaving behind two layers of water. In Figure 5.8(g) this water evaporation under positively charged graphene is schematically represented.

We interpret the formation of droplets to water molecules originating from the third water layer. This leaves behind a depleted region with two water layers. Figures 5.8, parts c-f, show the sample at 107 min, 116 min, 125 min and 6.8 h at +4V, respectively. One can see that the water droplet grows. With time, the droplet also exhibits dynamic behavior and moves up to a new position, leaving a small droplet behind. Also, two new droplets nucleate at the middle of the AFM image. The size of the droplets and depletion of the third water layer reaches a maximum after 3.2 h. The height of the large droplet in Figure 5.8(f) is 9 nm and its lateral dimensions are 820 and 560 nm, respectively. Figure 5.8(h) shows the phase image corresponding to the topography image of Figure 5.8(f). One can see that there is no phase difference at the locations of the water droplets, so we conclude that these droplets are formed under the graphene and not on top. Also, a substantial amount of water has evaporated from the interface, as can be seen by the white arrow in Figure 5.8(b). This water evaporation reached a maximum in Figure 5.8(f). In another experiment, water evaporation without the formation of water droplets is observed. Most likely, the local geometry of the graphene/mica interface determines whether or not droplets form.

¶A movie of the enhanced water intercalation due to the negative applied charge in Figure 5.7 can be found at https://pubs.acs.org/doi/suppl/10.1021/acs.langmuir.7b02759

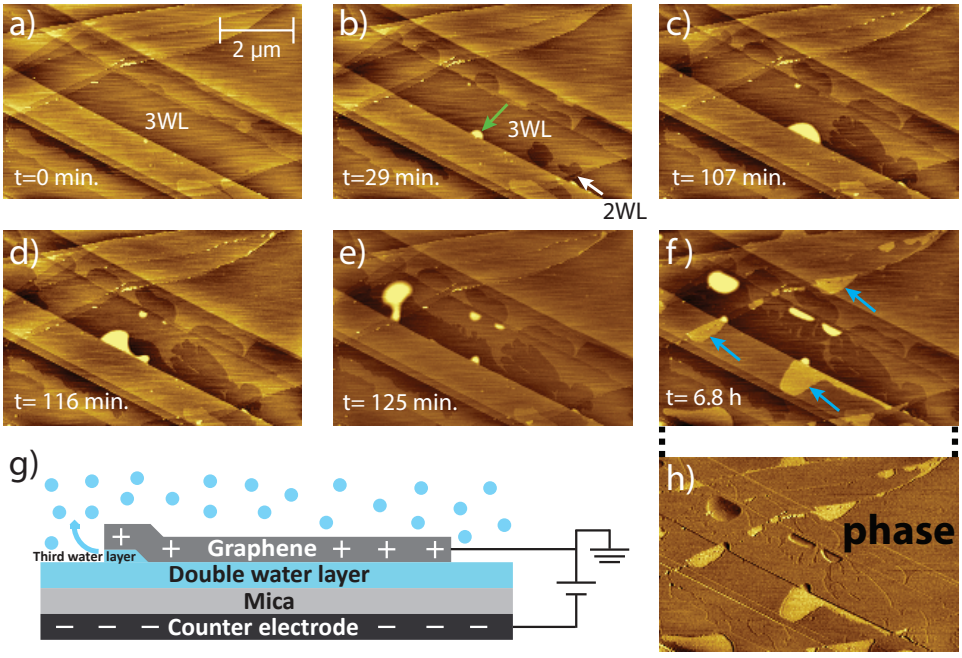

Figure 5.8: Graphene-mica sample at high humidity (RH = 87%). (a) A third water layer has completely formed under the graphene flake. (b-f) A voltage of +4V is applied to the graphene for 29 min, 107 min, 116 min, 125 min and 6.8 h, respectively. (g) Schematic illustration of the sample under high humidity conditions with a positive charge applied to the graphene.(h) Phase image corresponding to topography image (f).

In Figure 5.8(f) we also observed layers on top of the graphene, indicated by the blue arrows. The phase image in Figure 5.8(h) indicates that these layers are on top of the graphene due to a contrast at these locations. These layers are always observed when scanning at high humidity with higher positive voltages applied to the graphene. In contrast to the dynamic water layers observed at high humidity (and with negative applied voltage to the graphene), these layers show no fuzzy edges and have smaller variations in the area between consecutive AFM scans. Initial growth of these layers is observed at the edges of the graphene, next to areas with only mica. We have not been able to verify whether these layers disappear when the humidity is lowered. We do not think that these layers are a result of oxidation of the graphene, since no current is flowing. Furthermore, oxidized graphene has a different appearance. Grain boundaries and defect locations oxidize, as shown by Matsumoto et al.[44]

In Figure 5.9 we reversed the polarity by applying a negative voltage of -4V to the graphene. The AFM images in Figure 5.9 are taken after 10 min, 19 min and 9.4 h, respectively. We see that the droplets shrink and the water, mostly from the droplets, spreads to form a third water layer. After 47 min most of the third water layer has formed again. Only after 9.4 h, a complete three layer water film has been formed. Some water droplets disappeared where others remained slightly visible as an elevated region. We saw the same effect during another experiment where we completely switched off the voltage. Also, note the growth of third water layers at the top right in Figure 5.9(c). These layers, which grow from within the graphene when a negative charge is applied, are discussed in the previous section. The droplet shrinkage and water intercalation when switching off the positive applied voltage and applying a negative voltage to the graphene confirm that the positive applied voltage is responsible for the nucleation of the droplets and the evaporation of the third water layer out of the graphene-mica slit pore[‖].

5.4 Discussion

Our experimental results clearly show an asymmetry in the behavior of water in a graphene-mica slit pore when applying a negative or positive charge to the graphene. In this section, we elaborate on possible mechanisms which

[‖] A movie of the droplet formation and the third water layer evaporation/formation can be found at https://pubs.acs.org/doi/suppl/10.1021/acs.langmuir.7b02759

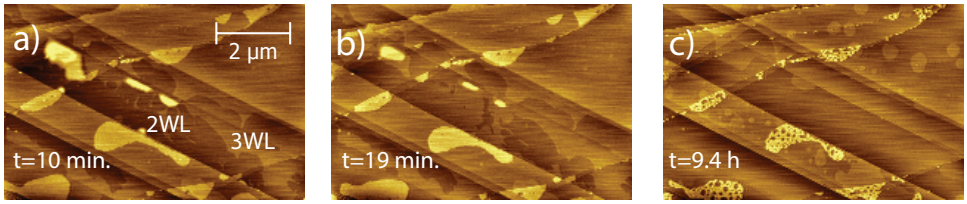

Figure 5.9: High humidity (RH = 87%). The voltage is changed from +4 V to -4 V. Images are taken at 10 min, 19 min and 9.4 h after changing the voltage, respectively.

can explain our experimental observations.

First of all, we want to address that our system is not a typical electrowetting experiment in which wetting phenomena are typically independent of polarization. In our experimental setup, the counter electrode is not in contact with the water. To reconfirm that our system deviates from a typical electrowetting experiment, we placed a small droplet on an HOPG flake on mica without a counter electrode in contact with the water droplet. When we applied a positive or negative charge to the graphene, changes in the macroscopic contact angle were not observed. This leads us to conclude that the wetting and dewetting we observe in the graphene-mica slit pore is a molecular-scale phenomenon.[45] However, theory[46] and experiments have shown that on doped monolayer graphene a lowering of the contact angle can be observed. The doping was obtained by applying high voltages to the graphene[47] (-100V and +100V) or chemically doping the graphene.[48] In our case, the doping effect was probably not observed since we used HOPG flakes (instead of monolayer graphene) and relatively low voltages.

Here, we are dealing with a highly confined system consisting of only three confined water layers. The first two water layers on mica show ordering when covered with graphene.[7,26,49] This agrees with our experimental observations. When we apply a negative or positive charge to a graphene-mica system under ambient conditions with only two intercalated water layers, no changes are observed. This indicates that a double water layer is unaffected by the surface charges on the graphene. Only the liquid-like third water layer, which is situated on top of the double water layer and next to the graphene, seems to be affected by surface charges on the graphene. The ordering of the water is induced by the mica. The further away from the mica, the

lower the ordering of the water molecules will be.[26,33] The first water layer on mica forms a 2D ice layer, which first has been predicted by theory.[50] Here, half of the water molecules in the first water layer are oriented with their hydrogen sides toward the mica. From experiments with scanning tunneling spectroscopy (STS), one can see that areas with one water layer show doping of the graphene.[20] This is attributed to the ordering of the water molecules in a structure with a net dipole moment. Additional evidence comes from conductive AFM measurements, in which a higher conductivity of the graphene areas with only one water layer was observed.[21] We anticipate that the second layer will exhibit less order. Additionally, due to intermolecular interactions, only a small part of the water molecules will face the mica with the OH bonds. Theoretical calculations reveal that the second water layer has an in-plane disorder and is shown to be in a liquid-like state.[26] Some water molecules in the first layer flip and form hydrogen bonds with water molecules of the second water layer. Indeed, STS results show that graphene on top of two water layers is not doped, indicating the absence of any charge transfer.[20,21] The third layer is least ordered.[51] The water molecules in the third layer are less ordered due to their larger distance from the mica. They can rotate easier and diffuse. Therefore, water molecules in the third layer are structurally less stable and exhibit less in-plane order.

The electric field we applied is relatively small. When we take into account the dielectric constants and thickness of the water and the mica, we obtain an electric field E over the three water layers of 3731 V/m during the -2V experiment. Calculating the energy $= E \cdot \mu$, where μ is the dipole moment vector, which has a value of $6.2{\cdot}10^{-30}$ C·m for water, we find an energy of 0.14 μeV. This value is negligible compared to $k_B T$, which has a value of 25.7 meV at room temperature. With such a small electric field and corresponding energy, the polarization of all the water molecules due to this electric field is highly unlikely. The charge is calculated to be $0.22{\cdot}10^{-3}$ μC/cm^2. Assuming a graphene area of 25 μm^2, the charge will be $5.53{\cdot}10^{-5}$ pC. This charge can apparently only change the dipole moment of water layers close to the graphene surface.

Regarding the third layer, in the current model, we argue that the water molecules have higher "flexibility" when the hydrogen side points to the graphene, as compared to the oxygen side. This is attributed to the longer total length of the O-H bond and the H-graphene bond than the O-graphene bond. This higher flexibility allows the water molecules to follow better the

lattice periodicity of graphene. Therefore, the system is able to form a third water layer. On the other hand, and when graphene is positively charged, the oxygen side of the water molecule has to face the graphene surface. The large lattice mismatch of 12% between graphene and ice (oxygen-oxygen distance in ice-I_h = 0.276 nm[52] and a_{gr} = 0.246 nm[53]) hinders the formation of the third layer. This leads to the experimentally observed partial "dewetting" of the third layer.

Taking the above comments into account, we suggest the following mechanism is at play. In the case of negatively charged graphene, the hydrogen side of the water molecules in the third water layer rotates toward the graphene. During this rotation, the hydrogen bonds with the second water layer remain. This new orientation of the water molecules is apparently a more preferred orientation since enhanced water intercalation is observed. At positively charged graphene, the oxygen side of the water molecules in the third water layer rotates toward the graphene, resulting in broken hydrogen bonds with the second water layer. To lower the interfacial energy, the water molecules in the third water layer form 3D droplets and evaporate out of the slit pore.

Our observation is in line with the work of Li et al.[26] They performed ab initio molecular dynamics simulations of a water trilayer between graphene and mica. They observed that the water molecules in the third water layer have a strong tendency to flip and form dangling OH bonds, which is not observed in a bilayer system.

Our experimental results can also be compared to MD simulations done by Taherian et al.[54] They used a slightly different experimental setup where a nanodroplet of water was squeezed between a positively charged and a negatively charged graphene surface. In their study, asymmetric nanoscale electrowetting was observed. The authors found a larger contact angle on negatively charged graphene than on positively charged graphene. Thus, the positively charged graphene has enhanced wetting properties compared to negatively charged graphene. Their result is in contrast to our experimental finding, where we observed that the negatively charged graphene exhibits enhanced wetting properties. This discrepancy may be due to the more confined nature of the water in the graphene-mica slit pore in our experiment. Also, in their work, they use two hydrophobic graphene surfaces, where in our work we use a hydrophilic mica surface and a hydrophobic graphene surface. Since graphene is more hydrophobic than mica, the water has less interaction with the two surfaces. Therefore, the charge has a larger influence

on the orientation of the water molecules. In addition, the charge densities used in their simulations (1 μC/cm^2) are significantly higher than the charge densities we had during our experiments ($0.22{\cdot}10^{-3}$ μC/cm^2). Therefore different physical phenomena may be observed.

Finally, our experimental work is compared to MD simulations performed by Ostrowski et al.[46] and experimental work by Ashraf et al.[48] and Hong et al.[47] They investigated nanodroplets on doped graphene and observed a lowering of the contact angle when p-type or n-type doping was applied to the graphene. This decrease of the contact angle indicates a less hydrophobic graphene surface upon doping. This observation is also in contrast with our experimental observation where we only see a decrease in hydrophobicity at negatively charged graphene surfaces. Also here, the absence of confinement may cause the discrepancy. Taking everything together, why the asymmetry in the breaking of the hydrogen bonds exists between positive and negative charges applied to the graphene is currently unknown and further theoretical studies need to be undertaken to clarify this phenomenon.

5.5 Conclusions

We presented the first experimental study of the electrowetting behavior of confined water at the nanoscale. We started with a double water layer intercalated in a graphene-mica slit pore under ambient conditions. Under high humidity conditions, a third water layer entered the slit pore. Upon application of a negative charge to the graphene, an enhancement of the formation of the third water layer was observed. In this case, we suggested that the hydrogen side of the water molecules in the third water layer rotates toward the graphene, which is apparently a preferred orientation. In contrast, when we applied a positive charge to the graphene, evaporation of the third water layer and droplet formation were observed. These droplets consisted of water molecules which were initially located in the third water layer. In this situation, we suggested that the oxygen side of the water molecules in the third water layer rotates toward the graphene, breaking the hydrogen bonds with the second water layer. The appearance of dangling bonds together with a lattice mismatch between the confined water and the graphene could explain the formation of the 3D water droplets and water evaporation out of the slit pore. The asymmetry between the positively and negatively charged graphene is not yet fully understood. Further theoretical studies are needed

to understand this phenomenon.

Bibliography

[1] Fu, Q.; Bao, X. Surface Chemistry and Catalysis Confined under Two-Dimensional Materials. *Chem. Soc. Rev.* **2017**, *46*, 1842–1874.

[2] Deng, D.; Novoselov, K. S.; Fu, Q.; Zheng, N.; Tian, Z.; Bao, X. Catalysis with Two-Dimensional Materials and Their Heterostructures. *Nat. Nanotechnol.* **2016**, *11*, 218–230.

[3] Li, H.; Xiao, J.; Fu, Q.; Bao, X. Confined Catalysis under Two-Dimensional Materials. *Proc. Natl. Acad. Sci. U. S. A.* **2017**, *114*, 5930–5934.

[4] Dollekamp, E.; Bampoulis, P.; Poelsema, B.; Zandvliet, H. J. W.; Kooij, E. S. Electrochemically Induced Nanobubbles between Graphene and Mica. *Langmuir* **2016**, *32*, 6582–6590.

[5] An, H.; Tan, B. H.; Moo, J. G. S.; Liu, S.; Pumera, M.; Ohl, C.-D. Graphene Nanobubbles Produced by Water Splitting. *Nano Lett.* **2017**, *17*, 2833–2838.

[6] Lee, C.; Wei, X.; Kysar, J. W.; Hone, J. Measurement of the Elastic Properties and Intrinsic Strength of Monolayer Graphene. *Science* **2008**, *321*, 385–388.

[7] Xu, K.; Cao, P.; Heath, J. R. Graphene Visualizes the First Water Adlayers on Mica at Ambient Conditions. *Science* **2010**, *329*, 1188–1191.

[8] Lui, C. H.; Liu, L.; Mak, K. F.; Flynn, G. W.; Heinz, T. F. Ultraflat Graphene. *Nature* **2009**, *462*, 339–341.

[9] Novoselov, K. S.; Geim, A. K.; Morozov, S. V.; Jiang, D.; Zhang, Y.; Dubonos, S. V.; Grigorieva, I. V.; Firsov, A. A. Electric Field Effect in Atomically Thin Carbon Films. *Science* **2004**, *306*, 666–669.

[10] Novoselov, K. S.; Jiang, D.; Schedin, F.; Booth, T. J.; Khotkevich, V. V.; Morozov, S. V.; Geim, A. K. Two-Dimensional Atomic Crystals. *Proc. Natl. Acad. Sci. U. S. A.* **2005**, *102*, 10451–10453.

[11] Severin, N.; Lange, P.; Sokolov, I. M.; Rabe, J. P. Reversible Dewetting of a Molecularly Thin Fluid Water Film in a Soft Graphene Mica Slit Pore. *Nano Lett.* **2012**, *12*, 774–779.

[12] Rezania, B.; Dorn, M.; Severin, N.; Rabe, J. Influence of Graphene Exfoliation on the Properties of Water-Containing Adlayers Visualized by Graphenes and Scanning Force Microscopy. *J. Colloid Interface Sci.* **2013**, *407*, 500–504.

[13] Nair, R. R.; Blake, P.; Grigorenko, A. N.; Novoselov, K. S.; Booth, T. J.; Stauber, T.; Peres, N. M. R.; Geim, A. K. Fine Structure Constant Defines Visual Transparency of Graphene. *Science* **2008**, *320*, 1308.

[14] Gaskell, P. E.; Skulason, H. S.; Rodenchuk, C.; Szkopek, T. Counting Graphene Layers on Glass via Optical Reflection Microscopy. *Appl. Phys. Lett.* **2009**, *94*, 143101.

[15] Dorn, M.; Lange, P.; Chekushin, A.; Severin, N.; Rabe, J. P. High Contrast Optical Detection of Single Graphenes on Optically Transparent Substrates. *J. Appl. Phys.* **2010**, *108*, 106101.

[16] He, K. T.; Wood, J. D.; Doidge, G. P.; Pop, E.; Lyding, J. W. Scanning Tunneling Microscopy Study and Nanomanipulation of Graphene-Coated Water on Mica. *Nano Lett.* **2012**, *12*, 2665–2672.

[17] Bampoulis, P.; Lohse, D.; Zandvliet, H. J. W.; Poelsema, B. Coarsening Dynamics of Ice Crystals Intercalated between Graphene and Supporting Mica. *Appl. Phys. Lett.* **2016**, *108*, 011601.

[18] Ochedowski, O.; Bussmann, B. K.; Schleberger, M. Graphene on Mica - Intercalated Water Trapped for Life. *Sci. Rep.* **2014**, *4*, 6003.

[19] Shim, J.; Lui, C. H.; Ko, T. Y.; Yu, Y.-J.; Kim, P.; Heinz, T. F.; Ryu, S. Water-Gated Charge Doping of Graphene Induced by Mica Substrates. *Nano Lett.* **2012**, *12*, 648–654.

[20] Bampoulis, P.; Siekman, M. H.; Kooij, E. S.; Lohse, D.; Zandvliet, H. J. W.; Poelsema, B. Latent Heat Induced Rotation Limited Aggregation in 2D Ice Nanocrystals. *J. Chem. Phys.* **2015**, *143*, 034702.

[21] Bampoulis, P.; Sotthewes, K.; Siekman, M. H.; Zandvliet, H. J. W.; Poelsema, B. Graphene Visualizes the Ion Distribution on Air-Cleaved Mica. *Sci. Rep.* **2017**, *7*, 43451.

[22] Nemes-Incze, P.; Osváth, Z.; Kamarás, K.; Biró, L. Anomalies in Thickness Measurements of Graphene and Few Layer Graphite Crystals by Tapping Mode Atomic Force Microscopy. *Carbon* **2008**, *46*, 1435–1442.

[23] Kim, J.-S.; Choi, J. S.; Lee, M. J.; Park, B. H.; Bukhvalov, D.; Son, Y.-W.; Yoon, D.; Cheong, H.; Yun, J.-N.; Jung, Y.; Salmeron, M. Between Scylla and Charybdis: Hydrophobic Graphene-Guided Water Diffusion on Hydrophilic Substrates. *Sci. Rep.* **2013**, *3*, 2309.

[24] Song, J.; Li, Q.; Wang, X.; Li, J.; Zhang, S.; Kjems, J.; Besenbacher, F.; Dong, M. Evidence of Stranski–Krastanov Growth at the Initial Stage of Atmospheric Water Condensation. *Nat. Commun.* **2014**, *5*, 4837.

[25] Lee, M.; Choi, J.; Kim, J.-S.; Byun, I.-S.; Lee, D.; Ryu, S.; Lee, C.; Park, B. H. Characteristics and Effects of Diffused Water Between Graphene and a SiO_2 Substrate. *Nano Res.* **2012**, *5*, 710–717.

[26] Li, H.; Zeng, X. C. Two Dimensional Epitaxial Water Adlayer on Mica with Graphene Coating: An ab Initio Molecular Dynamics Study. *J. Chem. Theory Comput.* **2012**, *8*, 3034–3043.

[27] Li, Q.; Song, J.; Besenbacher, F.; Dong, M. Two-Dimensional Material Confined Water. *Acc. Chem. Res.* **2015**, *48*, 119–127.

[28] Cao, P.; Xu, K.; Varghese, J. O.; Heath, J. R. The Microscopic Structure of Adsorbed Water on Hydrophobic Surfaces under Ambient Conditions. *Nano Lett.* **2011**, *11*, 5581–5586.

[29] Komurasaki, H.; Tsukamoto, T.; Yamazaki, K.; Ogino, T. Layered Structures of Interfacial Water and Their Effects on Raman Spectra in Graphene-on-Sapphire Systems. *J. Phys. Chem. C* **2012**, *116*, 10084–10089.

[30] Verdaguer, A.; Segura, J. J.; López-Mir, L.; Sauthier, G.; Fraxedas, J. Communication: Growing Room Temperature Ice with Graphene. *J. Chem. Phys.* **2013**, *138*, 121101.

[31] Fletcher, N. H. The Chemical Physics of Ice. *Cambridge University Press: Cambridge, U.K.* **2009**,

[32] Bunch, J. S.; Verbridge, S. S.; Alden, J. S.; van der Zande, A. M.; Parpia, J. M.; Craighead, H. G.; McEuen, P. L. Impermeable Atomic Membranes from Graphene Sheets. *Nano Let.* **2008**, *8*, 2458–2462.

[33] Bollmann, T. R. J.; Antipina, L. Y.; Temmen, M.; Reichling, M.; Sorokin, P. B. Hole-Doping of Mechanically Exfoliated Graphene by Confined Hydration Layers. *Nano Res.* **2015**, *8*, 3020–3026.

[34] Kimmel, G. A.; Matthiesen, J.; Baer, M.; Mundy, C. J.; Petrik, N. G.; Smith, R. S.; Dohnálek, Z.; Kay, B. D. No Confinement Needed: Observation of a Metastable Hydrophobic Wetting Two-Layer Ice on Graphene. *J. Am. Chem. Soc.* **2009**, *131*, 12838–12844.

[35] Wang, C.; Lu, H.; Wang, Z.; Xiu, P.; Zhou, B.; Zuo, G.; Wan, R.; Hu, J.; Fang, H. Stable Liquid Water Droplet on a Water Monolayer Formed at Room Temperature on Ionic Model Substrates. *Phys. Rev. Lett.* **2009**, *103*, 137801.

[36] Akaishi, A.; Yonemaru, T.; Nakamura, J. Formation of Water Layers on Graphene Surfaces. *ACS Omega* **2017**, *2*, 2184–2190.

[37] Zheng, Y.; Su, C.; Lu, J.; Loh, K. P. Room-Temperature Ice Growth on Graphite Seeded by Nano-Graphene Oxide. *Angew. Chem., Int. Ed.* **2013**, *52*, 8708–8712.

[38] Bampoulis, P.; Teernstra, V. J.; Lohse, D.; Zandvliet, H. J. W.; Poelsema, B. Hydrophobic Ice Confined between Graphene and MoS_2. *J. Phys. Chem. C* **2016**, *120*, 27079–27084.

[39] Ashraf, A.; Wu, Y.; Wang, M. C.; Aluru, N. R.; Dastgheib, S. A.; Nam, S. Spectroscopic Investigation of the Wettability of Multilayer Graphene Using Highly Ordered Pyrolytic Graphite as a Model Material. *Langmuir* **2014**, *30*, 12827–12836.

[40] Li, Z.; Wang, Y.; Kozbial, A.; Shenoy, G.; Zhou, F.; McGinley, R.; Ireland, P.; Morganstein, B.; Kunkel, A.; Surwade, S. P.; Li, L.; Liu, H. Effect of Airborne Contaminants on the Wettability of Supported Graphene and Graphite. *Nat. Mater.* **2013**, *12*, 925.

[41] Rafiee, J.; Mi, X.; Gullapalli, H.; Thomas, A. V.; Yavari, F.; Shi, Y.; Ajayan, P. M.; Koratkar, N. A. Wetting Transparency of Graphene. *Nat. Mater.* **2012**, *11*, 217.

[42] Lee, H.; Ko, J.-H.; Choi, J. S.; Hwang, J. H.; Kim, Y.-H.; Salmeron, M.; Park, J. Y. Enhancement of Friction by Water Intercalated between Graphene and Mica. *J. Phys. Chem. Lett.* **2017**, *8*, 3482–3487.

[43] Schmitz, I.; Schreiner, M.; Friedbacher, G.; Grasserbauer, M. Phase Imaging as an Extension to Tapping Mode AFM for the Identification of Material Properties on Humidity-Sensitive Surfaces. *Appl. Surf. Sci.* **1997**, *115*, 190–198.

[44] Matsumoto, Y.; Tateishi, H.; Koinuma, M.; Kamei, Y.; Ogata, C.; Gezuhara, K.; Hatakeyama, K.; Hayami, S.; Taniguchi, T.; Funatsu, A. Electrolytic Graphene Oxide and its Electrochemical Properties. *J. Electroanal. Chem.* **2013**, *704*, 233–241.

[45] Daub, C. D.; Bratko, D.; Leung, K.; Luzar, A. Electrowetting at the Nanoscale. *J. Phys. Chem. C* **2007**, *111*, 505–509.

[46] Ostrowski, J. H. J.; Eaves, J. D. The Tunable Hydrophobic Effect on Electrically Doped Graphene. *J. Phys. Chem. B* **2014**, *118*, 530–536.

[47] Hong, G.; Han, Y.; Schutzius, T. M.; Wang, Y.; Pan, Y.; Hu, M.; Jie, J.; Sharma, C. S.; Müller, U.; Poulikakos, D. On the Mechanism of Hydrophilicity of Graphene. *Nano Lett.* **2016**, *16*, 4447–4453.

[48] Ashraf, A.; Wu, Y.; Wang, M. C.; Yong, K.; Sun, T.; Jing, Y.; Haasch, R. T.; Aluru, N. R.; Nam, S. Doping-Induced Tunable Wettability and Adhesion of Graphene. *Nano Lett.* **2016**, *16*, 4708–4712.

[49] Ou, X.; Wang, X.; Lin, Z.; Li, J. Heterogeneous Condensation of Water on the Mica (001) Surface: A Molecular Dynamics Simulation Work. *J. Phys. Chem. C* **2017**, *121*, 6813–6819.

[50] Odelius, M.; Bernasconi, M.; Parrinello, M. Two Dimensional Ice Adsorbed on Mica Surface. *Phys. Rev. Lett.* **1997**, *78*, 2855–2858.

[51] Reischl, B.; Watkins, M.; Foster, A. S. Free Energy Approaches for Modeling Atomic Force Microscopy in Liquids. *J. Chem. Theory Comput.* **2013**, *9*, 600–608.

[52] Petrenko, V. F.; Whitworth, R. W. *Physics of Ice*; OUP: Oxford, 1999.

[53] Enachescu, M.; Schleef, D.; Ogletree, D. F.; Salmeron, M. Integration of Point-Contact Microscopy and Atomic-Force Microscopy: Application to Characterization of Graphite/Pt(111). *Phys. Rev. B: Condens. Matter Mater. Phys.* **1999**, *60*, 16913–16919.

[54] Taherian, F.; Leroy, F.; van der Vegt, N. F. A. Interfacial Tension Does Not Drive Asymmetric Nanoscale Electrowetting on Graphene. *Langmuir* **2015**, *31*, 4686–4695.

6

Tuning the friction of graphene on mica by alcohol intercalation

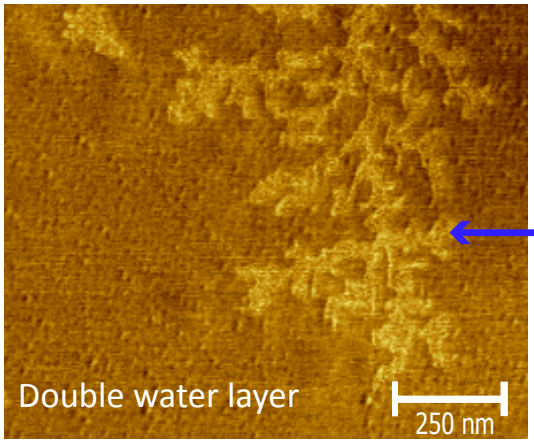

The friction of graphene on mica was studied using lateral force microscopy. We observed that intercalation of alcohol molecules significantly increases the friction of graphene, as compared to water. A 2.4 times increase in friction between an AFM tip and single layer graphene was observed. Moreover, the friction of graphene is found to be higher for single-layer graphene than multilayer graphene. We attribute the increase in friction to the larger size of the alcohol molecules, which changes the vibrational spectrum and thus the energy dissipation. The significant variation of the frictional characteristics of graphene at the nanoscale by altering the intercalant could open up applications for the next-generation nano-lubricants and nano-devices.

6.1 Introduction

Friction is the process when translational kinetic energy is converted to the surface atom vibrations.[1] For example, in atomic force microscopy (AFM), friction results in the transfer of momentum from the tip to surface atoms. The control over friction at the nano-scale is of great importance for nano-mechanical applications in tribology.[2–4] In most cases a lower friction is favorable due to lower energy losses, e.g. in lubricant systems. On the other hand, an increase in friction is sometimes desirable, e.g. in braking systems. Having the possibility to tune the friction between a high and low, could result in novel nano-devices.

An interesting system to investigate the friction of supported 2D materials consists of graphene on mica, between which molecules are intercalated from the vapor phase. For graphene on mica, the excitation and energy transfer process can be studied separately. When an AFM tip slides over a graphene surface, it excites out of plane lattice vibrations of the graphene, the so-called flexural phonons.[5] This lattice vibrational energy is transferred to the out of plane phonon modes of the intercalated molecules and the mica. Lee et al.[6] showed that increasing the number of intercalated water layers between graphene and mica resulted in a higher friction on the graphene. They attributed the higher friction to the increase of the out-of-plane phonon density of states (DOS) for the graphene and the water, and the larger overlap of the phonon DOS between graphene, water and the mica. They also found that when replacing H_2O molecules with D_2O, the friction was reduced due to the larger mass of the D_2O molecules, which resulted in a lower phonon density of states frequency and thus a lower energy dissipation.[7]

In this work, we study whether the friction of graphene can be tuned by changing the size and therewith the vibrational modes of the intercalated molecules. For this, we replaced water with larger alcohol molecules. The alcohol molecules have different vibrational modes, e.g. the stretch of the C-C bond and the C-O bonds. We also investigated whether the friction of graphene can be tuned by varying the size of the intercalated alcohol molecules. For this purpose, we used methanol, ethanol and 2-propanol. Moreover, in this study we also addressed the effect of graphene layer thickness on the friction.

6.2 Experimental section

The mechanical exfoliation method was used to deposit graphene on mica.[8–10] We have used muscovite mica (SPI, V1) as a substrate. Mica is a mineral, which can be cleaved to atomically flat layers.[11] Graphene is a single atom thin 2D material. It is flexible and impermeable to water and gases.[12,13] Water can easily intercalate between the two materials since mica is hydrophilic.[14] During the mechanical exfoliation method, a piece of highly oriented pyrolytic graphite (HOPG, grade ZYB, MikroMasch) was cleaved with Scotch tape. After cleavage, loose vertical standing flakes where transferred with a tweezer from the HOPG substrate to the mica sample. By not using Scotch tape for the HOPG transfer, contamination due to tape was prevented.[15] The HOPG flake was then gently pressed onto the mica and was subsequently removed. In some cases, small HOPG flakes remained attached to the mica surface. The small graphene flakes on mica were located with optical reflection microscopy (Leica DM2500 MH).[16,17] In this setup, the light source and microscope objective were both positioned above the sample.[18] The thickness of the graphene flakes was further characterized by AFM (Agilent 5100). The AFM is equipped with an environmental chamber that allows exposure of the sample to different gases. To obtain lateral force microscopy images, the AFM was operated in contact mode.

The AFM environmental chamber was initially purged with nitrogen to remove water vapor. Subsequently, we started purging with alcohol vapor. The alcohol was placed in a gas washing bottle. The gas washing bottle was already in place during the purging with nitrogen to further reduce the water concentration of the system. We quickly opened the gas washing bottle and filled it approximately halfway with alcohol. The nitrogen flow rate was adjusted to $\sim$0.5 L/min, such that there was only calm bubbling of the alcohol in the gas washing bottle. In our experiments, we used three different alcohols: methanol (Sigma-Aldrich, anhydrous 99.8%), ethanol (EMSURE, analytical quality) and 2-propanol (Sigma-Aldrich, anhydrous, 99.5%). The alcohols must have a water concentration as low as possible. Having water contamination in the alcohols results in the filling of the fractals with water instead of alcohol.[19] We established a low water concentration by using anhydrous alcohols. Furthermore, we used a new bottle of alcohol for every measurement since after opening, water from the ambient enters the bottle which contaminates the alcohol.

In the measurement of Figure 6.1 and Figure 6.2, we used a HI'RES-C14/CR-AU AFM tip (MikroMasch), with a nominal spring constant of 5 N/m and a nominal resonance frequency of 160 kHz. In the measurement of Figure 6.3 we used a AD-E-0.5-SS tip (diamond tip, Adama Innovations) with a nominal spring constant of 0.5 N/m and a nominal resonance frequency of 30 kHz. This AFM tip is very sharp, which allows to visualize individual potassium ions on the mica.[20] Finally, in the measurement of Figure 6.4 and Figure 6.5, we used a PPP-CONTSCR AFM tip (NANOSENSORS^{TM}), with a nominal spring constant of 0.2 N/m and a nominal resonance frequency of 13 kHz. This AFM tip is well-suited for lateral force microscopy since it has a flexible cantilever, resulting in a high lateral sensitivity.

To convert the lateral deflection voltage to a lateral force, the improved wedge calibration method of Varenberg et al.[21] was used. This method is based on the wedge calibration method of Ogletree et al.[22] In the improved wedge calibration method, a TGF11 silicon calibration grating (MikroMasch), with trapezoidal steps under an angle of 54.74°, was scanned. In Section 3.1.3 details of this calibration method are provided.

6.3 Results and discussion

The graphene-mica sample was first scanned under ambient conditions and at room temperature. Under ambient conditions, water is always present between the two materials.[10,14,23–27] This water film is two layers thick.[20,28–30] A schematic illustration of the sample under ambient conditions is given in Figure 6.1(a). Note that the schematic illustration is not to scale. When the relative humidity (RH) is lowered to ∼0.1% by purging with nitrogen, part of the top water layer evaporates,[10] as shown in the schematic illustration in Figure 6.1(b). The molecules leave the graphene-mica slit pore via bottom(B)-type step edges. At a B-type step edge, a bottom layer of graphene ends and the layer on top bends. This results in a small channel through which water molecules can escape. A 2D-ice layer remains at the location of the evaporated water molecules, with a fractal-like appearance,[10,28] as shown in the AFM topography image in Figure 6.1(c). The fractals are darker than their surroundings, indicating a lowering of the graphene height at this location. The red square indicates the area of interest, which will be discussed in the next section. The thickness of the graphene blanket in this image amounts to four layers.

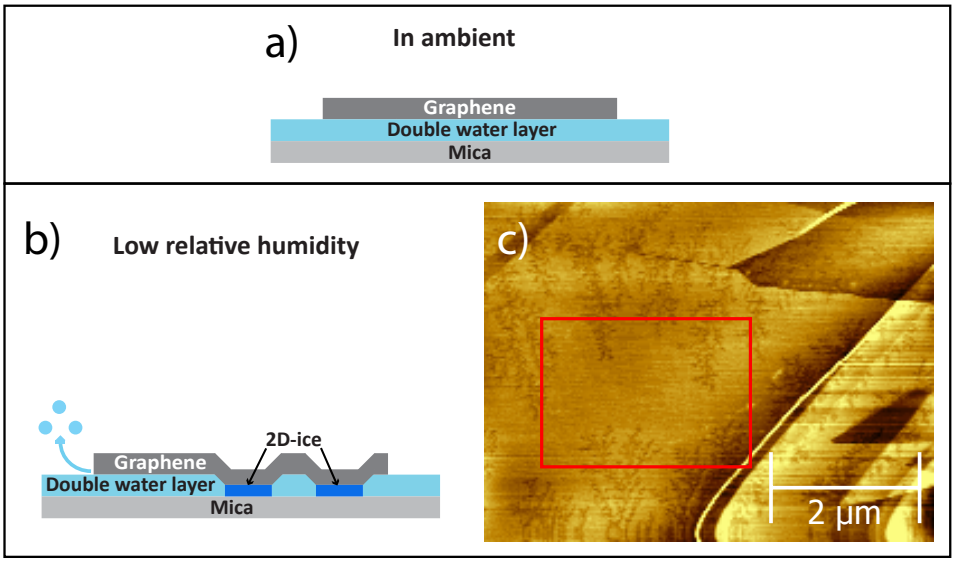

Figure 6.1: A schematic illustration of the sample (a) under ambient conditions and (b) under low relative humidity conditions. (c) An AFM topography image under low relative humidity conditions, RH = ∼0.1%. The red square indicates the area of interest, referred to in the text. A HI'RES-C14/CR-AU AFM tip was used.

When the system is subsequently purged with alcohol, the alcohol molecules fill the region on top of the 2D-ice fractals.[31] This is schematically depicted in Figure 6.2(a). Figure 6.2(b) shows the AFM topography image of the red squared area in Figure 6.1(c). This image was taken 2 h after the nitrogen environment was replaced by a 2-propanol environment. At the top right, a small contrast can be discerned, as compared to the double water layer. This contrast is due to the intercalation of 2-propanol molecules on top of the 2D-ice fractal. The 2-propanol molecules are larger than the water molecules, resulting in an elevation of the graphene sheet. Filling of the 2D-ice fractals typically occurs within tens of minutes.[31] The intercalation of alcohol is observed to be irreversible. The alcohol islands remain when we transfer the sample to ambient. This is in contrast with the observations of Severin et al.,[19] where the alcohol islands shrink when exposed to ambient conditions. Probably, their ambient conditions were under higher humidity, resulting in the intercalation of water molecules back into the slit pore. To test this hypothesis, we exposed the sample to a relative humidity of 80-90% and we indeed observed that part of the alcohol evaporated from the slit pore and is replaced by water molecules. In this experiment, not all fractals are filled with 2-propanol. At the left and bottom side of this image, the remaining 2D-ice fractals are observed. The explanation for this may be that some pores between graphene and mica are clogged, inhibiting the intercalation of the 2-propanol molecules at these locations.

Figure 6.2(c) shows the AFM lateral deflection voltage trace image, which was simultaneously recorded with the AFM topography image. In this friction image, a clear increase in friction is observed at the location of the 2-propanol fractal, as compared to the surrounding double water layer. The larger size and the additional vibrational modes of the C-C and C-O bonds of the 2-propanol molecule is assumed to lead to an increase of the number of vibrational modes and therefore the out-of-plane phonon DOS compared to water, therewith increasing the friction. To further validate this assumption, supporting density functional theory calculations should be done. Unfortunately this lies outside the scope of our work. The increase in mass of alcohol molecules compared to water cannot be the the dominant factor for the increase in friction increase since it has been shown that an increase in mass results in a decrease in friction[7].

In Figure 6.2(c) contrast can also be observed at the location of the 2D-ice fractals. In contrast to the alcohol intercalated areas, this contrast originates

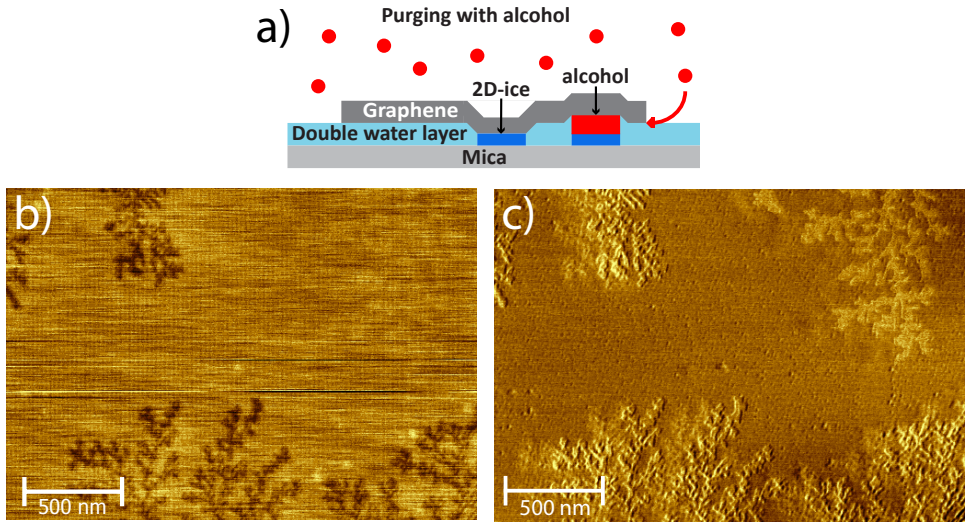

Figure 6.2: (a) A schematic illustration of the sample when purged with alcohol. (b) An AFM topography image. The sample is exposed to a 2-propanol environment. The top right fractal filled with 2-propanol. A HI'RES-C14/CR-AU AFM tip was used. (c) Simultaneously obtained AFM friction image (lateral deflection voltage, trace image).

from edge effects due to the relatively large height variations at these fractal edges. Moreover, the image in Figure 6.2(c) appears to suffer from a double tip artifact.

To enable determination of the friction on the 2D-ice fractals, a zoomed-in image is required. Figure 6.3(a) represents an AFM topography image of a different graphene-mica sample under low RH conditions. This location consists of single-layer graphene. The 2D-ice fractal has a lower height compared to the double water layer, as can be seen by the darker contrast in this image. Figure 6.3(b) shows the simultaneously recorded lateral deflection trace image. No clear contrast in friction is observed, although there is a change in corrugation on the 2D-ice fractals compared to the double water layer. This change in corrugation was already observed by Bampoulis et al.[20] They attributed the features to the potassium ions on the mica surface. Since graphene perfectly follows the topography of its underlying substrate, individual potassium ions affect the measured LFM image and as such can

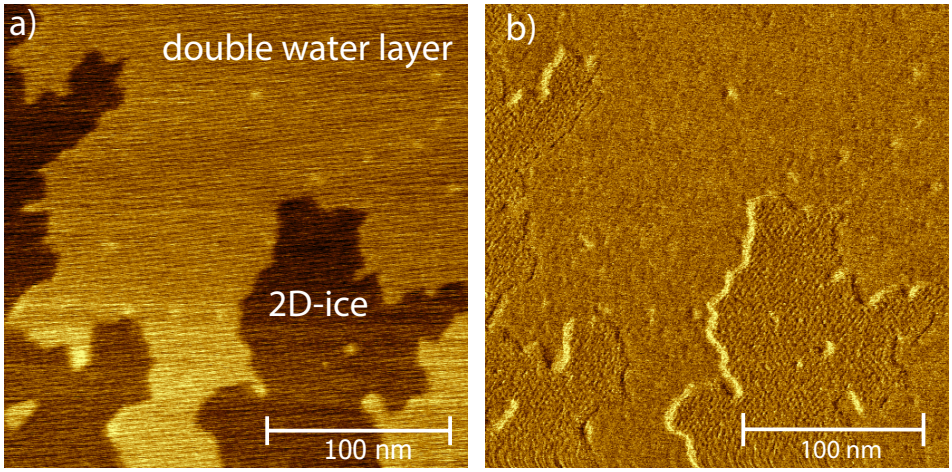

Figure 6.3: (a) An AFM topography image under low RH conditions. (b) The simultaneously obtained AFM friction image (lateral deflection voltage, trace image). The potassium ions can be observed at the location of the 2D-ice. An AD-E-0.5-SS AFM tip was used.

be visualized. Edge effects are still present, but they represent a smaller part of the image and 2D-ice plateaus can be clearly discerned.

To investigate the behavior of a different alcohol, ethanol has been intercalated between graphene and mica in another sample. Figure 6.4(a) shows an AFM topography image graphene-mica sample with intercalated ethanol. The brighter regions represent the intercalated ethanol islands. Like 2-propanol, again a higher friction is observed as compared to the double water layer. The number of graphene layers is also indicated. Figure 6.4(c) shows the line profile of the height, corresponding to the red line in Figure 6.4(a). Clear steps in height are observed from the double water to the ethanol islands on the 2D-ice. A coarsening effect is observed for the ethanol islands under bilayer and trilayer graphene (BLG and TLG, respectively), as compared to SLG. Under SLG small ethanol islands are visible. Under BLG and TLG these islands have merged together and formed larger alcohol plateaus. This coarsening effect was also found by Severin et al.[19,32] Figure 6.4(b) shows the simultaneously recorded lateral deflection trace image of the sample. To observe contrast in the friction between areas with a varying

number of graphene layers, a significant normal force F_N must be applied to the sample. In this measurement, the applied normal force was 66.4 nN. When increasing the normal force, a linear increase in the lateral force F_L was observed, following Amontons' relation $F_L = \mu F_N$,[33] where μ is the friction coefficient.

The magnitude of the friction is significantly larger for SLG as compared to BLG and TLG. We can account for the larger friction for thinner graphene by considering that puckering occurs due to the tip adhesion during sliding of the AFM tip over the surface. The graphene deforms out-of-plane to ripple in front of the AFM tip in the scanning direction, effectively resulting in a larger contact area. With increasing thickness, the graphene becomes more rigid, i.e. stiffer, which leads to less bending and stretching of the layers. As a result, the puckering is less pronounced and the detected friction is lower. That the friction is higher on SLG is in line with the work of Lee et al.[34] They observed that the friction of graphene on SiO_2 increases with decreasing the number of graphene layers. They also found that the same holds for MoS_2, $NbSe_2$ and h-BN on SiO_2.[35] Li et al.[35,36] observed that a change in friction when altering the number of graphene layers does not hold for a mica substrate without intercalated water molecules. This was ascribed due to the fact that the graphene strongly adheres to the atomically flat mica. The effect of layer thickness is more pronounced for graphene on ethanol than for graphene on the double water layer. That the friction of graphene on a double water layer is dependent on the layer thickness was already observed by Lee et al.[6]

To quantify the friction, we converted the half-width of the friction loop W_{exp} ([lateral trace - lateral retrace]/2) to the lateral force F_L. In Section 3.1.3, the conversion method is explained. Figure 6.4(d) shows the line profile of the friction, corresponding to the red line in Figure 6.4(b). A clear stepwise increment in friction is observed as the tip moves from the double water layer to the ethanol islands. For single layer graphene on alcohol on top of the 2D-ice layer the friction is 2.4 times higher than for graphene on top of two layers of water. The bar plot in Figure 6.4(e) summarizes the friction values of Figure 6.4(d). These values were obtained by taking the mean value of a larger area at the same scan heights. The obtained friction forces are of the same order of magnitude as found in the work of Lee et al.[6]

It was not possible to compare the friction between the different alcohols. The AFM tip becomes less sharp after scanning due to forces on the tip and

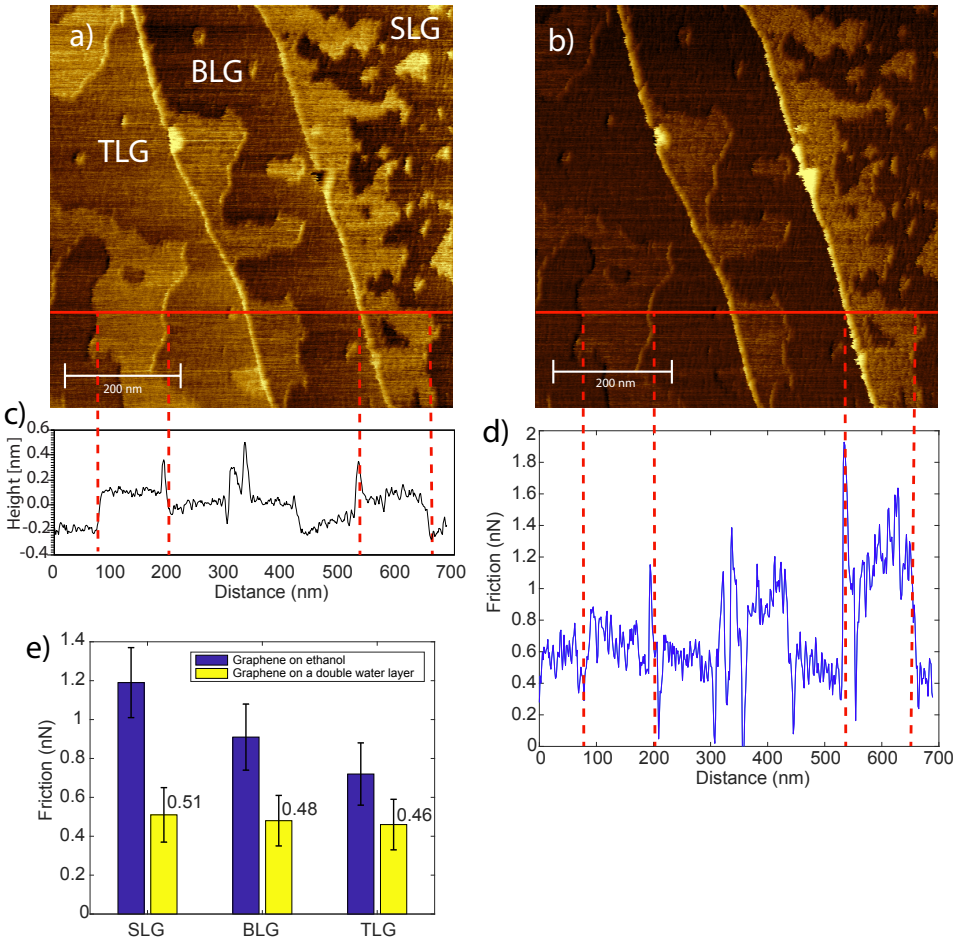

Figure 6.4: (a) An AFM topography image. The brighter regions represent intercalated ethanol islands. A PPP-CONTSCR AFM tip was used. (b) The simultaneously obtained AFM friction image (lateral deflection voltage, trace image). The normal force was 66.4 nN. (c) Line profile of the height, corresponding to the red line in (a). (d) Line profile of the friction, corresponding to the red line in (a). (e) Bar plot of the friction of graphene on ethanol and the double water layer for SLG, BLG and TLG.

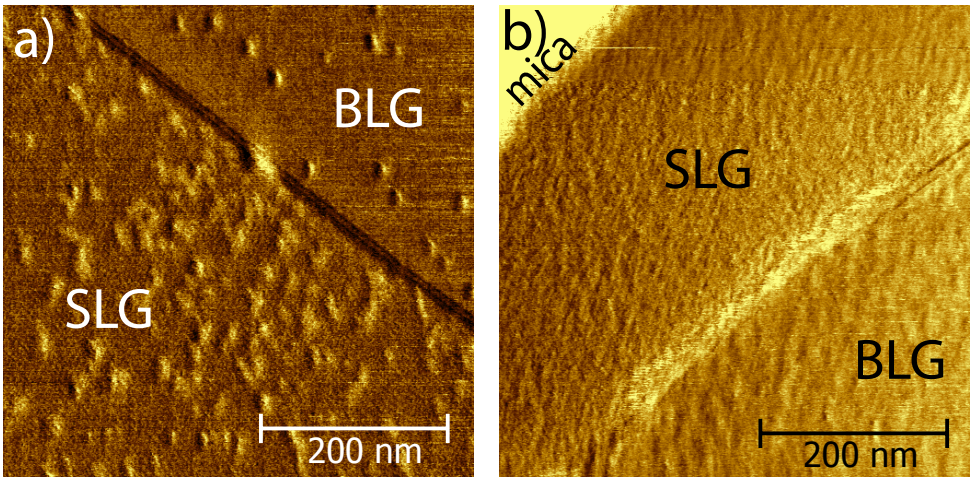

Figure 6.5: AFM friction images (lateral deflection trace images) after intercalation of (a) 2-propanol and (b) methanol; the number of graphene layers is indicated. A PPP-CONTSCR AFM tip was used.

therefore, the frictional forces change. The best method is to compare the friction within one scan line or scan lines close to each other. We tried to compare the friction by normalizing the friction signal of the alcohol to the friction signal of the double water layer, which should be constant. For this comparison the same number of graphene layers is needed. For monolayer methanol and 2-propanol however, small alcohol islands of ∼15 nm in diameter formed. This can be seen in the AFM friction images in Figure 6.5(a) for 2-propanol and Figure 6.5(b) for methanol (lateral deflection voltage, trace images). Edge effect friction gradients dominate the friction signal of the alcohol islands, which results in a highly inaccurate friction value. For an accurate friction value, large alcohol plateaus are needed. Although no accurate values can be obtained, a lighter contrast is observed as compared to the double water layer, indicating a higher friction for 2-propanol and methanol. For the same reason, it was also not possible to investigate the influence of the thickness of the graphene blanket for 2-propanol and methanol. The 2-propanol fractal in Figure 6.2 probably remained since it was situated under four layers of graphene.

6.4 Conclusions

We have studied the influence of alcohol intercalation between graphene and mica on the frictional properties of the graphene. We observed a higher friction for methanol, ethanol and 2-propanol, as compared to an intercalated double water layer. We attribute this increase in friction to the larger size and extra vibrational modes of the alcohol molecules. We also confirmed that single layer graphene has a higher friction than bilayer and trilayer graphene. To summarize, we demonstrate the ability to tune the friction of graphene by changing the environmental conditions and therewith the intercalated molecules between graphene and mica. Alcohol may therefore be a good candidate to be used in applications in nano-devices where control of the frictional properties of graphene is important.

Bibliography

[1] Cannara, R. J.; Brukman, M. J.; Cimatu, K.; Sumant, A. V.; Baldelli, S.; Carpick, R. W. Nanoscale Friction Varied by Isotopic Shifting of Surface Vibrational Frequencies. *Science* **2007**, *318*, 780–783.

[2] Persson, B. N. *Sliding Friction: Physical Principles and Applications*; Springer Science & Business Media, 2013.

[3] Carpick, R. W.; Salmeron, M. Scratching The Surface: Fundamental Investigations of Tribology with Atomic Force Microscopy. *Chem. Rev.* **1997**, *97*, 1163–1194.

[4] Park, J. Y.; Salmeron, M. Fundamental Aspects of Energy Dissipation in Friction. *Chem. Rev.* **2013**, *114*, 677–711.

[5] Mariani, E.; von Oppen, F. Flexural Phonons in Free-Standing Graphene. *Phys. Rev. Lett.* **2008**, *100*, 076801.

[6] Lee, H.; Ko, J.-H.; Choi, J. S.; Hwang, J. H.; Kim, Y.-H.; Salmeron, M.; Park, J. Y. Enhancement of Friction by Water Intercalated between Graphene and Mica. *J. Phys. Chem. Lett.* **2017**, *8*, 3482–3487.

[7] Lee, H.; Ko, J.-H.; Song, H. C.; Salmeron, M.; Kim, Y.-H.; Park, J. Y. Isotope- and Thickness-Dependent Friction of Water Layers Intercalated Between Graphene and Mica. *Tribol. Lett.* **2018**, *66*, 36.

[8] Novoselov, K. S.; Geim, A. K.; Morozov, S. V.; Jiang, D.; Zhang, Y.; Dubonos, S. V.; Grigorieva, I. V.; Firsov, A. A. Electric Field Effect in Atomically Thin Carbon Films. *Science* **2004**, *306*, 666–669.

[9] Novoselov, K. S.; Jiang, D.; Schedin, F.; Booth, T. J.; Khotkevich, V. V.; Morozov, S. V.; Geim, A. K. Two-Dimensional Atomic Crystals. *Proc. Natl. Acad. Sci. U. S. A.* **2005**, *102*, 10451–10453.

[10] Severin, N.; Lange, P.; Sokolov, I. M.; Rabe, J. P. Reversible Dewetting of a Molecularly Thin Fluid Water Film in a Soft Graphene-Mica Slit Pore. *Nano Lett.* **2012**, *12*, 774–779.

[11] Lui, C. H.; Liu, L.; Mak, K. F.; Flynn, G. W.; Heinz, T. F. Ultraflat Graphene. *Nature* **2009**, *462*, 339–341.

[12] Bunch, J. S.; Verbridge, S. S.; Alden, J. S.; van der Zande, A. M.; Parpia, J. M.; Craighead, H. G.; McEuen, P. L. Impermeable Atomic Membranes from Graphene Sheets. *Nano Lett.* **2008**, *8*, 2458–2462.

[13] Lee, C.; Wei, X.; Kysar, J. W.; Hone, J. Measurement of the Elastic Properties and Intrinsic Strength of Monolayer Graphene. *Science* **2008**, *321*, 385–388.

[14] Xu, K.; Cao, P.; Heath, J. R. Graphene Visualizes the First Water Adlayers on Mica at Ambient Conditions. *Science* **2010**, *329*, 1188–1191.

[15] Rezania, B.; Dorn, M.; Severin, N.; Rabe, J. Influence of Graphene Exfoliation on the Properties of Water-Containing Adlayers Visualized by Graphenes and Scanning Force Microscopy. *J. Colloid Interface Sci.* **2013**, *407*, 500–504.

[16] Nair, R. R.; Blake, P.; Grigorenko, A. N.; Novoselov, K. S.; Booth, T. J.; Stauber, T.; Peres, N. M. R.; Geim, A. K. Fine Structure Constant Defines Visual Transparency of Graphene. *Science* **2008**, *320*, 1308.

[17] Gaskell, P. E.; Skulason, H. S.; Rodenchuk, C.; Szkopek, T. Counting Graphene Layers on Glass via Optical Reflection Microscopy. *Appl. Phys. Lett.* **2009**, *94*, 143101.

[18] Dorn, M.; Lange, P.; Chekushin, A.; Severin, N.; Rabe, J. P. High Contrast Optical Detection of Single Graphenes on Optically Transparent Substrates. *J. Appl. Phys.* **2010**, *108*, 106101.

[19] Severin, N.; Sokolov, I. M.; Rabe, J. P. Dynamics of Ethanol and Water Mixtures Observed in a Self-Adjusting Molecularly Thin Slit Pore. *Langmuir* **2014**, *30*, 3455–3459.

[20] Bampoulis, P.; Sotthewes, K.; Siekman, M. H.; Zandvliet, H. J. W.; Poelsema, B. Graphene Visualizes the Ion Distribution on Air-Cleaved Mica. *Sci. Rep.* **2017**, *7*, 43451.

[21] Varenberg, M.; Etsion, I.; Halperin, G. An Improved Wedge Calibration Method for Lateral Force in Atomic Force Microscopy. *Rev. Sci. Instrum.* **2003**, *74*, 3362–3367.

[22] Ogletree, D. F.; Carpick, R. W.; Salmeron, M. Calibration of Frictional Forces in Atomic Force Microscopy. *Rev. Sci. Instrum.* **1996**, *67*, 3298–3306.

[23] Bampoulis, P.; Lohse, D.; Zandvliet, H. J. W.; Poelsema, B. Coarsening Dynamics of Ice Crystals Intercalated between Graphene and Supporting Mica. *Appl. Phys. Lett.* **2016**, *108*, 011601.

[24] Ochedowski, O.; Bussmann, B. K.; Schleberger, M. Graphene on Mica - Intercalated Water Trapped for Life. *Sci. Rep.* **2014**, *4*, 6003.

[25] Shim, J.; Lui, C. H.; Ko, T. Y.; Yu, Y.-J.; Kim, P.; Heinz, T. F.; Ryu, S. Water-Gated Charge Doping of Graphene Induced by Mica Substrates. *Nano Lett.* **2012**, *12*, 648–654.

[26] Bampoulis, P.; Sotthewes, K.; Dollekamp, E.; Poelsema, B. Water Confined in Two-Dimensions: Fundamentals and Applications. *Surf. Sci. Rep.* **2018**, *73*, 233 – 264.

[27] He, K. T.; Wood, J. D.; Doidge, G. P.; Pop, E.; Lyding, J. W. Scanning Tunneling Microscopy Study and Nanomanipulation of Graphene-Coated Water on Mica. *Nano Lett.* **2012**, *12*, 2665–2672.

[28] Bampoulis, P.; Siekman, M. H.; Kooij, E. S.; Lohse, D.; Zandvliet, H. J. W.; Poelsema, B. Latent Heat Induced Rotation Limited Aggregation in 2D Ice Nanocrystals. *J. Chem. Phys.* **2015**, *143*, 034702.

[29] Dollekamp, E.; Bampoulis, P.; Poelsema, B.; Zandvliet, H. J. W.; Kooij, E. S. Electrochemically Induced Nanobubbles between Graphene and Mica. *Langmuir* **2016**, *32*, 6582–6590.

[30] Dollekamp, E.; Bampoulis, P.; Faasen, D. P.; Zandvliet, H. J. W.; Kooij, E. S. Charge Induced Dynamics of Water in a Graphene-Mica Slit Pore. *Langmuir* **2017**, *33*, 11977–11985.

[31] Bampoulis, P.; Witteveen, J. P.; Kooij, E. S.; Lohse, D.; Poelsema, B.; Zandvliet, H. J. W. Structure and Dynamics of Confined Alcohol-Water Mixtures. *ACS Nano* **2016**, *10*, 6762–6768.

[32] Severin, N.; Gienger, J.; Scenev, V.; Lange, P.; Sokolov, I. M.; Rabe, J. P. Nanophase Separation in Monomolecularly Thin Water-Ethanol Films Controlled by Graphene. *Nano Lett.* **2015**, *15*, 1171–1176.

[33] Amontons, G. *Mémoires de l'Académie Royale A* **1699**, 257–282.

[34] Lee, C.; Wei, X.; Li, Q.; Carpick, R.; Kysar, J. W.; Hone, J. Elastic and Frictional Properties of Graphene. *Phys. Status Solidi B* **2009**, *246*, 2562–2567.

[35] Lee, C.; Li, Q.; Kalb, W.; Liu, X.-Z.; Berger, H.; Carpick, R. W.; Hone, J. Frictional Characteristics of Atomically Thin Sheets. *Science* **2010**, *328*, 76–80.

[36] Li, Q.; Lee, C.; Carpick, R. W.; Hone, J. Substrate Effect on Thickness-Dependent Friction on Graphene. *Phys. Status Solidi B* **2010**, *247*, 2909–2914.

7

General conclusions and outlook

7.1 General conclusions

We have studied the dynamics of water between graphene and mica. We have shown that it is possible to nucleate nanobubbles between graphene and mica by reduction of the confined water molecules to hydrogen. This proves that there is still charge transport possible in the confined water film to establish the hydrogen evolution. Furthermore, the absence of surface nanobubbles on top of the graphene may indicate that surface nanobubbles do not occur during electrocatalytic reactions on surfaces. This means that the efficiency of electrocatalytic reactions can not further be optimized by electrochemical control over surface nanobubble formation.

We have also shown that charges on the graphene are responsible for the movement of the confined water layers between graphene and mica. We discovered the influence of the charge by altering the experimental setup to a setup in which no current was flowing through the system. We saw wetting behavior for negatively charged graphene and dewetting behavior for positively charged graphene. We attributed this asymmetry to the preferred molecular orientation of the water molecules in the third water layer. This is actually the first experimental work about electrowetting behavior at the nanoscale. This work could find applications in nanofluidic devices where control over the water flow at the nano-level is crucial.

Finally, we have shown that we can increase the friction of graphene by replacing intercalated water molecules by alcohol molecules. This alcohol intercalation was established by changing the environment from a low/ambient humidity environment to an alcohol vapor environment. This work can find

applications in devices where local control over the friction of graphene is important.

7.2 Outlook

The existence of surface nanobubbles is still under discussion in literature.[1] It was shown that disposable needles can cause PDMS contamination, which can mistakenly be interpreted as surface nanobubbles.[2] Electrochemically induced surface nanobubbles have been observed.[3,4] In these studies the authors used cantilevers with a similar spring constant compared to our work, i.e. 0.58 N/m and 2.8 N/m compared to our 0.6 N/m. In chapter 4 we observed the nucleation of nanobubbles between graphene and mica. However, we did not observe electrochemically induced surface nanobubbles on top of the graphene. The surface nanobubbles on top of the graphene may have nucleated outside the scan area of the AFM, or not exist at all. To answer what happens, one could develop a nano-electrode. These nano-electrodes should have dimensions smaller than the AFM scan range. For our Agilent 5100 AFM, the dimension should be smaller than 20x20 μm^2. The development of glass sealed nano-electrodes has been described in literature.[5,6] However, an AFM study on these nano-electrodes has never been done. My suggested development method for a nano-electrode is with lithography techniques. A schematic illustration of such nano-electrode is shown in Figure 7.1. In this method, the top part of a silicon wafer is oxidized to SiO_2 in an oven with O_2 treatment. A layer of positive photo resist can then be spin coated on the SiO_2. A mask with an opening at the location of the nano-electrode can then be placed on top of the photo resist. Illumination with UV light then weakens the photo resist at the location of the nano-electrode. The mask is then removed and the photo resist needs to be developed, i.e. to remove it at the location of the nano-electrode. Dry etching can then be applied to remove the SiO_2 at the location of the nano-electrode. An attachment layer (chromium) and titanium (hard metal) can then be sputtered onto the sample. Subsequently, removal of the photo resist by immersion in acetone results in the removal of the titanium outside the nano-electrode. The sample then needs to be polished in order to flatten the titanium nanoelectrode. RMS values of 0.3 nm are achievable with polishing,[7] which should be low enough to detect surface nanobubbles on the nano-electrode. When a voltage is applied to the titanium, an electrochemical current should start to occur. When

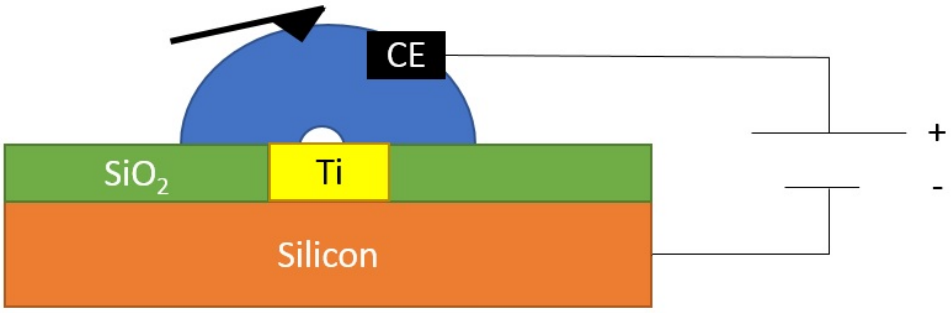

Figure 7.1: Schematic illustration of a nanoelectrode made with lithography techniques.

surface nanobubbles are observed by AFM, on can confirm the existence of surface nanobubbles. However, when one does not observe the formation of surface nanobubbles, the surface nanobubbles directly dissolve in the water, hinting toward the non-existence of surface nanobubbles.

Another future aim is to gain more control over nanobubbles between graphene and mica. The control of the exact size of the nanobubbles is difficult since the electrochemical current divides between the nanobubbles and likely also gas directly dissolves into the water on top of the graphene. We saw that the nanobubbles nucleated at B-type step edges and defects. Perhaps replacing mechanically exfoliated graphene with CVD graphene eliminates the random nucleation due to B-type step edges. However, CVD graphene is more rippled and therefore the confined water might become too large, resulting in the direct dissolution of the confined nanobubbles. Making ion beam etched holes in the mica might result in preferential nucleation sites for the nanobubbles since more water will be present at these locations.

Another future research topic is to study chemical reaction inside the nanobubbles between graphene and mica. A possibility is to study the chemical reactions inside these nanobubbles with X-rays. A challenge will be to point the X-ray beam exactly at the location of the graphene nanobubbles since they nucleate at random locations. The X-ray beam also needs to be small enough to detect local changes in chemistry. Also, the electrochemical cell - AFM/optical microscope combination should be modified such that the X-ray beam can reach the sample.

In chapter 5 we observed the movement of confined water layers due to an

applied charge to the graphene. A negative applied charge to the graphene resulted in enhanced water intercalation, and a positive charge resulted in water being expelled out of the slit pore. The main open question remains the physical mechanism behind this phenomenon. In chapter 5, for the explanation, we pointed in the direction of the preferred water orientation of the water molecules in the third water layer. When the graphene is negatively charged, one of the hydrogen sides of the water molecule is attracted to the graphene. The other side of the water molecule can still form a hydrogen bond with the second water layer below. In the case when the graphene is positively charged, the oxygen side of the water molecule will start to point toward the graphene. In this configuration, the water molecule has a limited rotational freedom and apparently cannot form a stable hydrogen bonds with the second water layer below. This happens probably due to a lattice mismatch between the graphene and the structured second water layer. The water molecules form droplets and evaporate out of the slit pore. Performing molecular dynamics simulations would be the best method to unveil the physics of the observed asymmetry since the water intercalation/deintercalation is a dynamic process.

Another future research topic is to study the influence of the confinement characteristics on the charge induced dynamics. One could for example investigate whether different charge induced dynamics occur for water between other (semi)conducting 2D-materials, e.g. between graphene and hydrophobic MoS_2 or between MoS_2 and mica. Due to the different lattice spacing in MoS_2, compared to graphene, one could study the influence of the lattice spacing on the stability of the water molecules when a positive charge is applied.

In chapter 6 we observed the increase in friction due to alcohol intercalation. We ascribed the increase in friction to the extra vibration modes of the alcohol molecules which enhance the energy transfer to the mica substrate, which increases the friction. First-principle density functional calculations (DFT) calculations could be performed to support our assumption. In DFT, a phonon density of states (DOS) spectrum can be calculated with and without alcohol intercalation. In the case without alcohol intercalation, a phonon DOS can be calculated for the graphene, the double water layer, and the mica. In the case with alcohol intercalation, a phonon DOS can be calculated for the graphene, the 2D-ice + alcohol and the mica. The phonon DOS can be calculated for the in-plane and out-of-plane phonon modes. The

latter has the highest influence on the friction. We expect that the 2D-ice + alcohol results in an increase in the phonon DOS. Also, a shift to higher frequencies is expected. Furthermore, an increased overlap of the graphene/intercalant/mica phonon modes is expected. All these changes result in a higher rate of frictional energy dissipation, thus increasing the energy transfer to the mica substrate.

Finally, one could also study the influence of alcohol intercalation on the friction of other two-dimensional materials. MoS_2 for example, has a 2D Young's modulus which is half of that of graphene,[8] meaning it is easier to deform. This could perhaps result in a higher friction increase at the location of the intercalated alcohol, compared to a double water layer.

Bibliography

[1] Berkelaar, R. Nanobubble-Like Objects at Solid-Liquid Interfaces. Ph.D. thesis, University of Twente, 2014.

[2] Berkelaar, R. P.; Dietrich, E.; Kip, G. A. M.; Kooij, E. S.; Zandvliet, H. J. W.; Lohse, D. Exposing Nanobubble-Like Objects to a Degassed Environment. *Soft Matter* **2014**, *10*, 4947–4955.

[3] Zhang, L.; Zhang, Y.; Zhang, X.; Li, Z.; Shen, G.; Ye, M.; Fan, C.; Fang, H.; Hu, J. Electrochemically Controlled Formation and Growth of Hydrogen Nanobubbles. *Langmuir* **2006**, *22*, 8109–8113.

[4] Yang, S.; Tsai, P.; Kooij, E. S.; Prosperetti, A.; Zandvliet, H. J. W.; Lohse, D. Electrolytically Generated Nanobubbles on Highly Orientated Pyrolytic Graphite Surfaces. *Langmuir* **2009**, *25*, 1466–1474.

[5] Luo, L.; White, H. S. Electrogeneration of Single Nanobubbles at Sub-50-nm-Radius Platinum Nanodisk Electrodes. *Langmuir* **2013**, *29*, 11169–11175.

[6] Zhang, B.; Galusha, J.; Shiozawa, P. G.; Wang, G.; Bergren, A. J.; Jones, R. M.; White, R. J.; Ervin, E. N.; Cauley, C. C.; White, H. S. Bench-Top Method for Fabricating Glass-Sealed Nanodisk Electrodes, Glass Nanopore Electrodes, and Glass Nanopore Membranes of Controlled Size. *Anal. Chem.* **2007**, *79*, 4778–4787.

[7] Gui, C.; Albers, H.; Gardeniers, J. G. E.; Elwenspoek, M.; Lambeck, P. V. Fusion Bonding of Rough Surfaces with Polishing Technique for Silicon Micromachining. *Microsyst. Technol.* **1997**, *3*, 122–128.

[8] Liu, K.; Yan, Q.; Chen, M.; Fan, W.; Sun, Y.; Suh, J.; Fu, D.; Lee, S.; Zhou, J.; Tongay, S.; Ji, J.; Neaton, J. B.; Wu, J. Elastic Properties of Chemical-Vapor-Deposited Monolayer MoS_2, WS_2, and Their Bilayer Heterostructures. *Nano Lett.* **2014**, *14*, 5097–5103.

Summary

The behavior of water under confinement is of utmost importance for the field of electrocatalysis, nanofluidics and lubrication. The dynamics of water under confinement are significantly different as compared to bulk water. Experimental knowledge of confined water was challenging to obtain due to the confined nature of the water, and therefore limited access to the water structures. With the discovery of the two-dimensional material graphene combined with scanning probe microscopy, a new approach to in-situ study confined water layers was born. The mechanical properties of graphene like its flexibility, impermeability and atomic thickness make it a perfect cover to study the water molecules. In this thesis, we studied the dynamic properties of water on mica, covered with a graphene coating. The goal of this PhD work was to increase the experimental knowledge of confined water.

In chapter 1, an introduction was given to the key concepts used in this thesis. We started by elaborating on the properties of graphene and mica. Afterward, we described the structure of water on mica. We ended this chapter by discussing the influence of the graphene cover.

In chapter 2, a literature overview was given of novel applications of confined water. In this chapter applications like graphene nanobubbles, water desalination and the graphene transfer method are discussed.

In chapter 3, we addressed the experimental techniques used in this thesis. We started by discussing the operation principles of atomic force microscopy (AFM). We described the operation principles of contact and tapping mode. In contact mode, lateral force microscopy imaging mode is specifically highlighted since it is significantly used in chapter 6. The chapter ends with the sample preparation method.

In chapter 4, we studied graphene nanobubbles between graphene and mica. The graphene on mica system is immersed in water and studied by AFM. The nanobubbles are created by applying a voltage to the graphene, resulting in splitting of the confined water to hydrogen gas (for negative voltages). The nanobubbles have a typical radius of a few hundred nanome-

ters and a height of a few tens of nanometer. The nanobubbles are dynamic and eventually an equilibrium established between the gas evolution by water splitting and the gas dissolution into the confined water film. When the voltage is switched off, the nanobubbles dissolve within seconds. When the hydrogen evolution is higher than the dissolution rate, the nanobubbles grow and delaminate the graphene. By phase imaging, we concluded that the nanobubbles nucleated between graphene and mica, and not on top. Moreover, we calculate that the pressure inside these nanobubbles is in the MPa range. Due to this high pressure, these graphene nanobubbles could potentially be used as a nanoreactor.

In chapter 5, we studied the charge induced dynamics of water between graphene and mica. We increased the relative humidity so that a third water layer started to intercalate between graphene and mica. After this intercalation, we applied a negative and a positive charge to the graphene. For negatively charged graphene, we observed that the third water layer intercalation speed was enhanced. On the contrary, for positively charged graphene, we observed that the third water layer intercalation was decreased and droplets formed. We attribute this polarization dependent behavior to the different orientation of the water molecules toward the positively/negatively charged graphene. For negatively charged graphene, we obtained a preferential orientation of the water molecules and for positively charged graphene we obtain an instable configuration. As a result, the water molecules evaporate out of the slit pore and form droplets which are energetically more favorable. The influence of charge on confined water is already relevant for the graphene transfer method in which water and therewith ion intercalation are crucial for a successful delamination of graphene.

In chapter 6, we studied the effect of alcohol intercalation between graphene and mica on the frictional properties of graphene. We found that the intercalation of alcohol increases the friction of graphene. We attributed this increase to the larger size of the alcohol molecules and the extra vibrational modes of the alcohol molecules. This results in a better energy dissipation into the sample and thus increase in friction. So by changing the intercalated molecules between graphene and mica, we can vary the friction. This could be implemented in future nano-lubrication devices.

In summary, we studied the physics of confined water in a graphene-mica system by splitting the water, applying a charge to the graphene and changing the intercalated molecules. All these studies expanded our experimentally

obtained knowledge of confined water which potentially will find applications in future devices.

Samenvatting

Het gedrag van opgesloten water is van groot belang voor het gebied van elektrokatalyse, nanofluidica en biologische systemen. De dynamiek van opgesloten water is significant anders in vergelijking met bulk water. Experimentele kennis van opgesloten water was lastig om te verkrijgen vanwege de beperkte toegangelijkheid tot de waterstructuren. Met de ontdekking van het tweedimensionale materiaal grafeen, gecombineerd met scanning probe microscopie, werd een nieuwe methode geboren om waterlagen in situ te bestuderen. De mechanische eigenschappen van grafeen, zoals grafeen's flexibiliteit, ondoordringbaarheid en atomaire dikte, maken het een perfecte beschermlaag om de watermoleculen te bestuderen. In dit proefschrift hebben we de dynamische eigenschappen van water op mica bestudeerd, bedekt met een grafeen coating. Het doel van dit doctoraatswerk was om de experimentele kennis van opgesloten water te vergroten.

In hoofdstuk 1 was een introductie gegeven over de belangrijkste concepten die in dit proefschrift zijn gebruikt. We begonnen met het beschrijven van de eigenschappen van grafeen en mica. Naderhand hebben we de structuur van water op mica toegelicht. We beëindigden dit hoofdstuk met het bespreken van de invloed van de grafeen op de waterlagen.

In hoofdstuk 2 werd een literatuuroverzicht gegeven van huidige toepassingen van opgesloten water. In dit hoofdstuk worden toepassingen zoals grafeen nanobellen, waterontzilting en de grafeen overbreningsmethode besproken.

In hoofdstuk 3 hebben we de experimentele technieken toegelicht die in dit proefschrift worden gebruikt. We begonnen met het bespreken van de werking van de atoomkrachtmicroscoop (AFM). We hebben de werking van de constante kracht mode en de oscillatie met amplitudemodulatie mode toegelicht. In de constante kracht mode wordt de laterale krachtmicroscopie specifiek toegelicht, omdat deze mode aanzienlijk wordt gebruikt in hoofdstuk 6. Het hoofdstuk eindigt met het toelichten van hoe de grafeen-mica samples worden gemaakt.

In hoofdstuk 4 bestudeerden we grafeen nanobellen tussen grafeen en mica. Het grafeen op mica systeem wordt ondergedompeld in water en bestudeerd met een AFM. De nanobellen worden gecreëerd door een spanning op het grafeen aan te leggen, wat resulteert in het splitsen van het opgesloten water tot waterstofgas (voor negatieve spanningen). De nanobellen hebben een typische straal van enkele honderden nanometers en een hoogte van enkele tientallen nanometers. De nanobellen zijn dynamisch en uiteindelijk wordt een evenwicht bereikt tussen de gasontwikkeling door watersplitsing en het oplossen van het waterstofgas in het opgesloten water. Wanneer de spanning is uitgeschakeld, lost het waterstofgas in de nanobellen binnen enkele seconden op. Wanneer de waterstofontwikkeling hoger is dan de oplossnelheid groeien de nanobellen en delamineren ze het grafeen. Door fase beeldvorming concludeerden we dat de nanobellen tussen grafeen en mica ontstaan, en niet bovenop het grafeen. Bovendien berekenen we dat de druk in deze nanobellen in het MPa bereik ligt. Vanwege deze hoge druk kunnen de grafeen nanobellen mogelijk worden gebruikt als een nanoreactor.

In hoofdstuk 5 hebben we de lading geïnduceerde dynamiek van water tussen grafeen en mica bestudeerd. We verhoogden de relatieve vochtigheid zodat een derde waterlaag intercaleerde tussen grafeen en mica. Na deze intercalatie pasten we een negatieve en een positieve lading toe op het grafeen. Voor negatief geladen grafeen zagen we dat de intercalatiesnelheid van de derde waterlaag verhoogde. In tegendeel, voor positief geladen grafeen zagen we dat de intercalatie van de derde waterlaag afnam en er druppeltjes vormden. We schrijven dit polarisatie afhankelijke gedrag toe aan de oriëntatie van de watermoleculen richting van het positief / negatief geladen grafeen. Voor negatief geladen grafeen hebben we een voorkeursoriëntatie van de watermoleculen verkregen en voor positief geladen grafeen krijgen we een instabiele configuratie. Door deze instabiele configuratie verdampen de watermoleculen uit de opsluiting tussen grafeen en mica en vormen ze druppels die energetisch gunstiger zijn. De invloed van lading op water in een opsluiting is al relevant voor de grafeen overbreningsmethode waarbij water en daarmee ionen-intercalatie cruciaal zijn voor een succesvolle delaminatie van grafeen van het substraat.

In hoofdstuk 6 hebben we het effect van alcoholintercalatie tussen grafeen en mica op de wrijvingseigenschappen van grafeen bestudeerd. We vonden dat de intercalatie van alcohol de wrijving van grafeen verhoogt. We hebben deze toename toegeschreven aan de grotere omvang van de alcoholmolecu-

len en de extra vibratie modi van de alcoholmoleculen. De extra vibratie modi resulteren in een betere energiedissipatie naar het sample en dus verhoogde wrijving. Dus door de geïntercaleerde moleculen tussen grafeen en mica te veranderen, kunnen we de wrijving variëren. Dit zou kunnen worden geïmplementeerd in toekomstige technologiën.

Samenvattend bestudeerden we de fysica van opgesloten water in een grafeen-mica systeem door het water te splitsen, een lading op het grafeen aan te brengen en de geïntercaleerde moleculen te veranderen. Al deze onderzoeken hebben onze experimenteel kennis van opgesloten water vergroot, wat mogelijk zijn toepassing in toekomstige technologiën zal vinden.

List of publications

Publications

- **Dollekamp, E.**; Bampoulis, P.; Poelsema, B.; Zandvliet, H.J.W.; Kooij, E.S. Electrochemically Induced Nanobubbles Between Graphene and Mica. *Langmuir*, **2016**, 32, 6582-6590.
- **Dollekamp, E.**; Bampoulis, P.; Faasen, D.P.; Zandvliet, H.J.W.; Kooij, E.S. Charge Induced Dynamics of Water in a Graphene-Mica Slit Pore. *Langmuir*, **2017**, 33, 11977-11985.
- Bampoulis, P.; Sotthewes, K.; **Dollekamp, E.**; Poelsema, B. Water Confined in Two Dimensions: Fundamental and Applications. *Surf. Sci. Rep.*, **2018**, 73, 233-264.

Submitted

- **Dollekamp, E.**; Bampoulis, P.; Siekman, M.H.; Kooij, E.S.; Zandvliet, H.J.W. Tuning the Friction of Graphene on Mica by Alcohol Intercalation
- Sotthewes, K.; van Bremen, R.; **Dollekamp, E.**; Boulogne, T.L.A.; Nowakowski, K.K.; Kas, D.G.; Zandvliet, H.J.W.; Bampoulis, P. Universal Fermi Level Pinning in Transition Metal Dichalcogenides

In preparation

- **Dollekamp, E.**; Verdelli, F.; Bampoulis, P.; Siekman, M.H.; Kooij, E.S.; Zandvliet, H.J.W Tuning the Electronic Properties of Graphene on Mica by Alcohol Intercalation
- Loessberg-Zahl, J.T.; de Bruijn, D.S.; van den Beld, W.E.T.; **Dollekamp, E.**; van den Berg, A.; Eijkel, J.C.T. Electrowetting-Controlled Diode-Like Behavior of Suspended Graphene Membranes

Acknowledgements

This thesis would not have been possible without the help of many others. I had four superb years in the Physics of Interfaces and Nanomaterials (PIN) group. Time flew by and I will definitely miss the nice atmosphere in the group.

Harold, Stefan, Arie and Martin, thank you for believing in me and giving me the opportunity to conduct my PhD in the PIN group. I have never regretted the choice of doing my PhD in this group.

Harold, my sincere thanks for being my supervisor. Due to your enthusiastic presence, there is always a nice atmosphere in the group. You always dropped by the offices for a coffee break and have a very informal relation with all the members of the group. I could also always enter your office for questions. Your guidance throughout my PhD is well appreciated.

Stefan, thank you for being my co-supervisor. I could always enter your office too when I had questions. Also thank you for giving me a lot of freedom during my PhD. Your extensive feedback on my papers and thesis was always very constructive and well appreciated. It really brought my work to a higher scientific level. Also, thanks for organizing the many nice group outings together with Simone and Kai. I have very good memories of the group outings to Dresden and Grenoble.

Arie, I enjoyed working together with you. You always had some good suggestions for further research during my Monday morning discussions. I also enjoyed assisting you with the course 'Physical Chemistry of Interfaces' and learned a lot from it.

Martin, thank you for your practical assistance during my PhD. When I had an experimental question, you could always guide me in the right direction. Your expertise in electronics also saved me a lot of time. For example, you quickly fixed laser of the AFM and assisted with the KPFM measurements. Also thanks for ordering the many AFM tips and chemicals. I also enjoyed our conversations a฿out cryptocurrencies. HODL!

Pantelis, I was blessed to work closely together with such a talented re-

searcher as you. You were always interested in my work, showed me how to work systematically and always had suggestions for further research when I got stuck. It is an honor to have you in my graduation committee now. Also thanks for introducing me to the world of go-karting. I enjoyed the many trips to the go-kart track in Oldenzaal. Your tips improved my karting skills significantly. I hope to beat you one day in the future. I wish you a successful career in Cologne.

I would also like to thank the members of my graduation committee, Prof. dr. S. De Gendt, Prof. dr. T. Banerjee, Prof. dr. J.C.T. Eijkel and Prof. dr. ir. R.G.H. Lammertink for their time and effort to read my thesis and be part of my PhD defense.

Bene, thank you for your scientific contributions to my work. During the Monday morning discussions you always had good suggestions for further research. I also appreciate that you are the chairman of my PhD defense ceremony.

Simone, thank you for handling all my administrative tasks. From booking my flights, handling my declarations and administering my holidays. Also thanks for organizing all the great events as being part of the outing committee.

Hans, thank you for your practical insights and helping me out in the workshop. Thanks to you I had some very nice electrochemical cells to work with.

Adil, it was nice to have to as a colleague. I enjoyed our trip to the RPGR conference in Australia and our road trip afterwards. Many good memories remain, from the cloudy Blue Mountains to the nice pizza in Merimbula. It was also an honor to be one of your paranimfs.

Rik, I had a good time with you during the many lunch breaks. It was also nice that we shared the same hobby: mountain biking. I enjoyed the many mountain bike trips with you through Twente and our mountain bike holiday to Winterberg.

Qirong, I was a honer to be your colleague. I enjoyed our many lunch breaks where you always had nice stories. You were also always very interested in my research. I will miss making funny pictures of you when you are sleeping on backseats of cars haha.

Kai, I enjoyed our conversations in the social corner and drinking beers (for me often Fanta's) with you. Also thanks for organizing the many group outings. I wish you all the best with your family and your permanent posi-

tion at the UT.

Lijie, I enjoyed our time together in the group, from the lunch breaks to the social activities. I wish you all the best with your associate professorship in China.

Francesco and Daniel, I enjoyed supervising you as a master and bachelor students, respectively. Thanks for contributing to my projects. I hope you learned something from me.

Tim, thank you for introducing me to wakeboarding. I still did wakeboarding in the last year of my PhD and hope to learn to jump in the future.

Chris, thank you for making the PIN Promotion Pack. It saved me a lot of time by having a LaTeX template for my thesis.

I would also thank my office mates Carolien, Martina, Jordi, Reinier, Jaap, Jasper, Lisette, Hairong, Liselotte, Xing, Valent and Erik for the nice time in our office CR 2.225.

I also would like to thank Özlem, Tabassom, Nikolai, Ruben, Mikhail, Herman, Herbert, Krystian, Zhen, Zhiquo, Jorn, Wojciech, Gerjan, Paul and all other members of the PIN group for who I now forget, for the good time. I really foster the nice memories.

Douwe, thanks for involving me in your master project. It was nice to work with you and cool that your challenging project succeeded. I wish you all the best with your PhD in the BIOS group.

Tobias, Marine and Yves-Matthieu, thank you for believing in me and giving me the opportunity to conduct a postdoc at the European Synchrotron Radiation Facility (ESRF) in Grenoble. I look forward to this new adventure in France.

There is of course also a life outside work, for which I have to thank several people.

I would like to thank all members of the PIN-ICE futsal team (Interfacionale) for the nice matches we played together in the lunch breaks. It was always a nice break of the day and fun to beat other research groups.

Vincent, Claudia and Leonie, I enjoyed being with you in the board of breakdance/hip-hop association Break-Even. We really made the association grow and future proof.

I would also like to thank all the members of the breakdance group of Break-Even. Next to breakdance group, it really feld like a friend group. I have many good memories of our training sessions, trips to breakdance events and movie evenings.

I would also like to thank all the members of triathlon association Aloha. I enjoyed our training sessions, from race-biking trough Twente to running on the UTrack. I also have good memories of our 'Aloha in de Bergen' trips to Aken and Sauerland.

I also would like to thank the trainers of Aloha. Thanks to you I was able to finish the full distance triathlon Mallorca in 2015 and can now call myself an IRONMAN.

I would also like to thank the mountain bike group of Klein Verzet. Although I joined you in the last year of my PhD, it was really nice to be a member. I discovered many new tracks in Twente and improved my mountain biking skills significantly.

I would also like to thank all the persons involved in the gravitation programme MCEC, especially the MCEC Twente members. It was always fun to get together and share ideas between our projects.

I would also like to thank my housemates of Campuslaan 67 for the nice time in the flat. I always enjoyed living there.

I also would like to thank my sisters Mirjam and Lisette for being my paranimfs and their support throughout the years

Finally, I would like to thank my parents for their interest and support throughout the years and giving me the freedom and trust in everything I do.